ASSEMBLY OF COLLOIDAL CRYSTALS WITH WELL-CHARACTERIZED PAIR INTERACTION POTENTIALS

by

Reginald Evon Rogers, Jr.

A dissertation submitted in partial fulfillment
of the requirements for the degree of
Doctor of Philosophy
(Chemical Engineering)
in The University of Michigan
2010

Doctoral Committee:

Professor Michael J. Solomon, Chair
Professor Sharon C. Glotzer
Professor Robert M. Ziff
Associate Professor Alan J. Hunt

2010

To my parents who have sacrificed much to help me reach this point in my life.

Thank you with all of my love.

ACKNOWLEDGMENTS

I would like to thank first and foremost my thesis advisor Michael Solomon. He has been an extraordinary mentor and has truly impacted my life and the career path I have chosen to pursue. I would also like to thank Sharon Glotzer, Alan Hunt, and Robert Ziff for their service as my dissertation committee. Thank you to Christopher Iacovella for his collaboration with the pair interaction potential work. Thank you also to Stephanie Teich-McGoldrick and Ramsey Zeitoun for their help with images and renderings for the ionic colloidal crystal work. Thank you to all members of the Solomon group, both graduate and undergraduate students. It has been a pleasure to work with them during my time here at Michigan. Thank you to the staff of the Chemical Engineering department, especially Shelley Fellers, Ruby Sowards, Harald Eberhardt, Susan Hamlin, and Mike Africa. All of these people have gone above and beyond the call of duty to assist me during my tenure within the department. Finally, and most importantly, I would like to thank all of my friends and family. Their overwhelming support during this journey will never be forsaken. I am, and will always be, forever grateful to everyone who I have crossed paths during my Ph.D. career.

TABLE OF CONTENTS

LIST OF FIGURES

LIST OF TABLES

LIST OF APPENDICES

ABSTRACT

The study of colloidal particles is of particular interested because of their applicability in photonic band-gap and sensing materials, food, and cosmetic products. The behavior of colloidal particles is difficult to predict and depends highly on the system. Slight changes in external variables (e.g. temperature or pressure) can lead from a crystalline solid to an amorphous liquid. This dissertation experimentally explores the behavior of colloidal particles to understand their tunability for self-assembly applications. Using confocal laser scanning microscopy (CLSM), a direct visualization technique, we were able to understand how these colloidal particles interact with one another and self assemble crystal structures composed of oppositely-charged particles.

We developed a methodology to directly measure the pair interaction potential of colloidal particles. Working with dilute ($\phi < 0.02$) colloidal suspensions, we measured the radial distribution functions using CLSM and image processing code. In conjuction with computer simulations, criteria for determining the dilute regime based on linear extrapolation of the potential of mean force to the limit of infinite dilution was developed. From this analysis, we were able to construct the pair interaction potential. Computer simulations were also used to examine issues associated with refinement of the error in the radial distribution function and pair potential. Simulations were also used to understand the effect, if any, polydispersity in the experimental system would have on the

proposed methodology. We found that our methodology held for polydispersities of less than 10% in the particle size.

We examined the role of sedimentation in the assembly of colloidal particles of opposite charge. Ionic colloidal crystals were successfully reproduced following the methods of Leunissen et al. [1]. The range of crystallization achievable under sedimentation was examined by varying the initial volume fraction and the density difference between the particles and solvent. We found that crystallization was achievable for medium to high initial volume fractions ($\phi_i \geq 0.12$) and across all density differences studied. To quantify our qualitative results, we computed the dimensionless Peclet number for each of our systems. We compare the Peclet number as a function of the initial volume fraction to similar results for hard-sphere crystallization as reported by Davis et al. [2]. We found the trend in ionic crystallization to be opposite to that of the Davis results. We hypothesize the mechanism for ionic colloidal crystallization to not simply depend on the rate at which the particles sediment but also on the charge interactions within the system.

1. Leunissen, M.E., C.G. Christova, A.P. Hynninen, C.P. Royall, A.I. Campbell, A. Imhof, M. Dijkstra, R. van Roij, and A. van Blaaderen, *Ionic colloidal crystals of oppositely charged particles.* Nature, 2005. **437**(7056): p. 235-240.
2. Davis, K.E., W.B. Russel, and W.J. Glantschnig, *Settling Suspensions of Colloidal Silica - Observations and X-Ray Measurements.* Journal of the Chemical Society-Faraday Transactions, 1991. **87**(3): p. 411-424.

CHAPTER 1

INTRODUCTION

1.1. Colloids and Forces

Colloidal science is the branch of science concerned with the understanding and application of particles with nanometer to micrometer length scales that have been suspended in solution. Colloids affect the lives of millions of people. People interact with colloidal systems on a day-to-day basis, many not knowing it. Colloids can be found in a variety of everyday items. These items range from food (e.g. yogurt), cosmetics (e.g. nail polish), and household goods (e.g. paints) [1-3]. Colloidal particles are also found in more hi-tech materials, including photonic band-gap and chemical/biological sensing applications [4-6]. Since the human interaction with these products is very high, a full understanding of colloidal behavior is critical for applications of these particles.

The small size of the colloidal particles provides a significant surface area-to-volume ratio. Therefore, their interaction with each other becomes crucial in defining the final physical response of these suspensions. Such suspensions can contain hydrodynamic, diffusive, gravitational and electrostatic forces [7]. These forces are functions of temperature, concentration, charge, size and shape of the particles. The nature of interactions defines the physical state of the suspension, which can vary from fully

dispersed to an ordered assembly [7]. The concentration of particles also plays a significant role in defining the structure. At low concentrations and low interactions a dispersed phase is a possibility [7]; however, a balance of attractive and repulsive forces at sufficiently high concentrations, along with the entropy of the system, can lead to ordered phases [8, 9]. Finally, intermediate and high concentrations with large inter-particle interactions may lead to aggregated and jammed structures [10, 11].

A key feature of colloids is their interaction through the excluded volume (hard sphere) potential [7, 12]. The excluded volume potential for hard bodies is a short-range repulsive interaction, which prohibits interpenetration of particles. The value of this potential is infinity when the particles are in contact and zero otherwise [13]. Such hard body interactions lead to disorder-order transitions at sufficiently high concentrations. Electrostatic and induced dipole moments give rise to repulsive (e.g. electrostatic) or attractive (e.g. van der Waals) forces that act on longer length scales than the excluded volume potential [7, 12]. Attractive forces favor aggregation of the particles. Large clusters of the particles are seen in suspensions where net forces are of an attractive nature. The addition of non-adsorbing polymer to a colloidal suspension can induce such attractive interactions. Addition of non-adsorbing polymer promotes the overlapping of excluded volume of the colloidal particles and thereby creates an imbalance in osmotic pressure. This imbalance in the osmotic pressure gives rise to an attractive force known as the depletion effect. If of sufficient strength, the depletion potential can often lead to phase separation [14, 15].

1.2. Colloidal Interactions

Equilibrium phase behavior of colloidal particles opens the door to new possibilities for characterizing interactions between particles. One class of colloidal systems that are a primary focus for assembly are those in which the particle is refractive index matched to the solvent. Refractive index matching minimizes strong van der Waals interactions that can disrupt the system leading to aggregation and/or gelation. Methods for characterizing these interactions vary and include 2-D and 3-D techniques. Traditional methods for capturing the interaction of colloidal systems include colloidal probe atomic force microscopy [16, 17], total internal reflection microscopy [18, 19], surface force apparatus [20, 21], and optical tweezers [22, 23]. These techniques perform 2-D analysis of particle interactions. Colloid probe atomic force microscopy, surface force apparatus, and total internal reflection microscopy examine the interaction of a particle with a surface. This is important because colloidal interactions with various surfaces can alter the phase behavior of the system depending on the conditions present at the time. Optical tweezers is a technique to control the position of particles by capturing them in optical traps. With these traps, an examination of particle-particle interactions is made possible.

While all four of these techniques are powerful in their own right, they do have their limitations. When interest is focused on particle-particle interactions, colloidal probe atomic force microscopy, surface force apparatus, and total internal reflection are not able to provide this information. These techniques are designed to capture the interactions between particles and surfaces. Both total internal reflection microscopy and optical tweezers rely on systems that are refractive index mismatched for optimal performance.

This is a disadvantage in the case when colloidal systems for assembly rely on solvents that are of similar refractive indices.

The progression of technology has led to the development of new techniques for understanding particle-particle interactions. Advances in the development of microscopy and image processing techniques have revolutionized how we are able to study colloidal particles. Microscopy developments have allowed the possibility for visualizing colloidal particles and their interactions in three-dimensional space. For example, confocal laser scanning microscopy is a technique that allows for imaging deep within a sample. Unlike light or optical microscopy, confocal microscopy is unique in that out-of-focus light is removed, by way of the confocal pinhole, therefore eliminating scattering in the object plane [24, 25]. As such, one is able to focus a beam of light well into a sample generating three-dimensional image volumes.

The development of image processing techniques by Crocker and Grier [26] is another step forward in gaining quantitative information from qualitative data. It used to be very challenging to determine 3-D information (e.g. particle position) with a single 2-D image slice. With application of Crocker and Grier's image processing methods, one is now able to obtain information such as particle positions, radial distribution functions, or mean square displacement of collective structures (i.e. image volumes). This additional information provides data that expands our knowledge and the scope of our understanding for applications of colloidal particles.

Simulations, used in conjunction with experiments, have also proven to be beneficial in characterizing colloidal particle interactions. Royall et al. [27] showed how the pair potential could be constructed using simulations to take an experimentally determined radial distribution function and generating the effective pair interaction potential. Lu et al. [28] parameterized short-range attractive potentials of micron-sized colloids by comparing measurements of the second virial coefficient and the cluster mass distributions to the results of Monte Carlo (MC) simulations. These results, among many others, demonstrate how simulations and experiments complement one another. Simulations allow experimentalists to expand their capabilities at understanding the complexities of various colloidal interaction phenomena.

There is still great interest in the development of a direct pathway to the true pair interaction potential without simulations. That is, one of the key limitations with simulations is the need for knowing the pair potential in order to match it to an experimental data set. A direct pathway that does not involve simulations would allow for quick access to the pair potential allowing for faster processing of experimental data. The challenge lies in developing a pathway consistent with statistical mechanics that could be verified through, but not rely on, simulations. Overcoming this challenge would greatly expand the possibilities for creating new methodologies for experimentally capturing the true pair interaction potential.

1.3. Assembly of Colloidal Particles

Understanding colloidal particle interactions is an important milestone for controlling their assembly. Self-assembly of colloidal particles is of great interest because of its validity in various applications, include photonic band-gap and sensing materials [29-32]. With self-assembly, the behavior of colloidal particles is naturally controlled. In other words, the particle behavior is dictated by the surrounding environment. Studies of this type are interesting because we are able to gain a greater appreciation for what these particles will do without human intervention. This, in turn, allows for applications to be built around the particles instead of the particles needing to work for the application.

Self-assembly also allows direct connections between particle interactions and what structures are formed. One self-assembly technique of interest is sedimentation [33]. Sedimentation operates under the influence of gravity. A dilute suspension is typically created and the particles are permitted to settle at a particular sedimentation rate. This rate is usually defined by a density difference between the particles and the solvent. The magnitude of the difference dictates the how fast (or slow) the particles will settle. Sedimentation has been used to study a wide array of crystallization of colloidal particles [34-45]. It has been shown that high quality crystals can be achieved using this technique. The limitation to this technique is the time it takes to form such crystals. Sedimentation times are typically on the order of days to weeks to achieve long-range ordered crystalline structures. This makes the practicality of sedimentation unfavorable for large-scale operations where mass production would be required.

There are many examples of sedimentation being used to form colloidal crystals. Davis and co-workers demonstrated that hard-sphere crystallization of silica particles was possible under conditions where the initial volume fraction was dilute such that the crystallization rate was not impeded by the sedimentation rate [34, 35]. They showed that the crystallization was controlled by the dimensionless Peclet number in addition to the initial volume fraction ($Pe^*\phi_i < 10^{-3}$ for crystallization). Hoogenboom et al. provided a critical analysis of stacking faults in colloidal crystals [46]. Also citing the Peclet number, they showed that these stacking faults and defects could be used to determine if a sediment was primarily hexagonal close packed, face center cubic, or mixture of two structures. Finally, Leunissen et al. examined sedimentation as it related to binary colloidal crystallization [40]. Taking advantage of opposite charges on their particles, they demonstrated crystallization was possible by controlling the charge on the particle and the size ratio between the two particles. They showed one was able to form not only the atomic analog cubic structures (i.e. CsCl and NaCl) but also more complex structures (e.g. LS_6 and LS_8) with long-range ordering.

The study of ionic colloidal crystals is of interest because of the limited work that has been done in this area. There is much promise with the application of this particular system, especially in photonics and photonic band-gap materials. Many of the studies presented have examined thermodynamics. In other words, much of the focus has been on describing what conditions these ionic colloidal crystals will be stable and what structures will form. There has been very limited work on understanding the kinetics behind ionic colloidal crystallization. An important question left to be answered is the

applicability of the findings of Davis et al. to ionic crystallization. Is the mechanism of ionic colloidal crystallization the same as hard-sphere crystallization? In other words, will ionic colloidal crystallization occur only in very dilute suspensions and under slow sedimentation rates? One of the objectives of this dissertation is to answer these questions.

1.4. Overview of Dissertation

In this dissertation, an examination of the interactions between colloids for assembly of colloidal crystals is presented. In Chapter 2, a study is presented aiming to develop a methodology for characterizing the pair interaction potential using experimental techniques and basic statistical mechanics. Working with dilute systems, linear extrapolation of the potential of mean force is utilized to determine the pair interaction potential of collective structures. Simulation tools are utilized in conjunction with the experimental work. These simulations will serve as a check of experimental results and provide verification that the developed methodology is working properly. Chapter 3 presents a study focused on understanding how sedimentation affects the formation of ionic colloidal crystals. Our hypothesis is that ionic colloidal crystals behave in the same manner as hard sphere crystals. Based on previous work with hard-sphere crystallization, it has been shown that crystallization takes place in very dilute systems when the sedimentation rate does not hinder the rate of crystallization. Our aim is to (1) reproduce ionic colloid crystals based on the methods of Leunissen et al. [40], (2) understand how density differences between the particles and solvent affect the rates of sedimentation and crystallization, and (3) quantify the sedimentation rate using the dimensionless Peclet

number. Finally, Chapter 4 presents the overall conclusions and recommended future work.

References

1. R. Cush; D. Dorman; P. S. Russo, *Macromolecules* **2004,** 37, (25), 9577-9584.
2. L. Hong; S. M. Anthony; S. Granick, *Langmuir* **2006,** 22, (17), 7128-7131.
3. A. D. Dinsmore; M. F. Hsu; M. G. Nikolaides; M. Marquez; A. R. Bausch; D. A. Weitz, *Science* **2002,** 298, (5595), 1006-1009.
4. G. M. Whitesides; M. Boncheva, *Proceedings of the National Academy of Sciences of the United States of America* **2002,** 99, (8), 4769-4774.
5. M. A. Horsch; Z. Zhang; S. C. Glotzer, *Nano Letters* **2006,** 6, 2406-2413.
6. C. M. van Kats; P. M. Johnson; J. van den Meerakker; A. van Blaaderen, *Langmuir* **2004,** 20, (25), 11201-11207.
7. S. D. A. Russel W.B., Schowalter W.R., *Cambridge Univ. Press, Cambridge* **1989**.
8. A. P. Hynninen; M. E. Leunissen; A. van Blaaderen; M. Dijkstra, *Physical Review Letters* **2006,** 96, (1), 4.
9. L. Onsager, *Annals of the New York Academy of Sciences* **1949,** 51, (4), 627-659.
10. E. Sanz; M. E. Leunissen; A. Fortini; A. van Blaaderen; M. Dijkstra, *Journal of Physical Chemistry B* **2008,** 112, (35), 10861-10872.
11. J. M. Valverde; M. A. S. Quintanilla; A. Castellanos, *Physical Review Letters* **2004,** 92, (25).
12. R.G. Larson, The Structure and Rheology of Complex Fluids, *Oxford University Press, Oxford* **1999**.
13. K. V. Tretiakov; K. W. Wojciechowski, *Physica Status Solidi B-Basic Solid State Physics* **2005,** 242, (3), 730-741.
14. S. Asakura; F. Oosawa, *Journal of Chemical Physics* **1954,** 22, (7), 1255-1256.
15. S. Asakura; F. Oosawa, *Journal of Polymer Science* **1958,** 33, (126), 183-192.
16. McKee, C.T., S.C. Clark, J.Y. Walz, and W.A. Ducker, *Relationship between scattered intensity and separation for particles in an evanescent field.* Langmuir, 2005. **21**(13): p. 5783-5789.
17. Butt, H.J., B. Cappella, and M. Kappl, *Force measurements with the atomic force microscope: Technique, interpretation and applications.* Surface Science Reports, 2005. **59**(1-6): p. 1-152.
18. Israelachvili, J.N., *Intermolecular and surface forces*. 2nd ed. 1992, London: Academic. xxi, 450 p.
19. Schorr, P.A., T.C.B. Kwan, S.M. Kilbey, E.S.G. Shaqfeh, and M. Tirrell, *Shear forces between tethered polymer chains as a function of compression, sliding velocity, and solvent quality.* Macromolecules, 2003. **36**(2): p. 389-398.
20. Bevan, M.A. and D.C. Prieve, *Direct measurement of retarded van der Waals attraction.* Langmuir, 1999. **15**(23): p. 7925-7936.
21. Claesson, P.M., T. Ederth, V. Bergeron, and M.W. Rutland, *Techniques for measuring surface forces.* Advances in Colloid and Interface Science, 1996. **67**: p. 119-183.
22. Furst, E.M., *Interactions, structure, and microscopic response: Complex fluid rheology using laser tweezers.* Soft Materials, 2003. **1**(2): p. 167-185.

23. Sainis, S.K., V. Germain, C.O. Mejean, and E.R. Dufresne, *Electrostatic interactions of colloidal particles in nonpolar solvents: Role of surface chemistry and charge control agents.* Langmuir, 2008. **24**(4): p. 1160-1164.
24. Pawley, J.B., *Handbook of biological confocal microscopy*. 2nd ed. 1995, New York: Plenum Press. xxiii, 632 p.
25. Solomon, M.J., Kogan, M., *Confocal Optical Microscopy.* Encyclopedia of Condensed Matter Physics, 2005: p. 229-235.
26. Crocker, J.C. and D.G. Grier, *Methods of digital video microscopy for colloidal studies.* Journal of Colloid and Interface Science, 1996. **179**(1): p. 298-310.
27. Royall, C.P., A.A. Louis, and H. Tanaka, *Measuring colloidal interactions with confocal microscopy.* Journal of Chemical Physics, 2007. **127**(4): p. 044507.
28. Lu, P.J., E. Zaccarelli, F. Ciulla, A.B. Schofield, F. Sciortino, and D.A. Weitz, *Gelation of particles with short-range attraction.* Nature, 2008. **453**(7194): p. 499-U4.
29. Ngo, T.T., C.M. Liddell, M. Ghebrebrhan, and J.D. Joannopoulos, *Tetrastack: Colloidal diamond-inspired structure with omnidirectional photonic band gap for low refractive index contrast.* Applied Physics Letters, 2006. **88**(24): p. 241920.
30. Hosein, I.D. and C.M. Liddell, *Convectively assembled asymmetric dimer-based colloidal crystals.* Langmuir, 2007. **23**(21): p. 10479-10485.
31. Hosein, I.D. and C.M. Liddell, *Convectively assembled nonspherical mushroom cap-based colloidal crystals.* Langmuir, 2007. **23**(17): p. 8810-8814.
32. Hosein, I.D. and C.M. Liddell, *Homogeneous, core-shell, and hollow-shell ZnS colloid-based photonic crystals.* Langmuir, 2007. **23**(5): p. 2892-2897.
33. Russel, W.B., Saville, D. A., Schowalter, W. R., *Colloidal Dispersions*. 1 ed. Cambridge Monographs on Mechanics and Applied Mathematics, ed. G.K. Batchelor. 1989, Cambridge: Cambridge University Press. 525.
34. Davis, K.E., W.B. Russel, and W.J. Glantschnig, *Settling Suspensions of Colloidal Silica - Observations and X-Ray Measurements.* Journal of the Chemical Society-Faraday Transactions, 1991. **87**(3): p. 411-424.
35. Davis, K.E., W.B. Russel, and W.J. Glantschnig, *Disorder-to-Order Transition in Settling Suspensions of Colloidal Silica - X-Ray Measurements.* Science, 1989. **245**(4917): p. 507-510.
36. Leunissen, M.E., M.T. Sullivan, P.M. Chaikin, and A. van Blaaderen, *Concentrating colloids with electric field gradients. I. Particle transport and growth mechanism of hard-sphere-like crystals in an electric bottle.* Journal of Chemical Physics, 2008. **128**(16): p. -.
37. Ackerson, B.J., S.E. Paulin, B. Johnson, W. van Megen, and S. Underwood, *Crystallization by settling in suspensions of hard spheres.* Physical Review E, 1999. **59**(6): p. 6903-6913.
38. Shereda, L.T., R.G. Larson, and M.J. Solomon, *Local stress control of spatiotemporal ordering of colloidal crystals in complex flows.* Physical Review Letters, 2008. **101**(3): p. -.
39. Royall, C.P., R. van Roij, and A. van Blaaderen, *Extended sedimentation profiles in charged colloids: the gravitational length, entropy, and electrostatics.* Journal of Physics-Condensed Matter, 2005. **17**(15): p. 2315-2326.

40. Leunissen, M.E., C.G. Christova, A.P. Hynninen, C.P. Royall, A.I. Campbell, A. Imhof, M. Dijkstra, R. van Roij, and A. van Blaaderen, *Ionic colloidal crystals of oppositely charged particles.* Nature, 2005. **437**(7056): p. 235-240.
41. Vermolen, E.C.M., A. Kuijk, L.C. Filion, M. Hermes, J.H.J. Thijssen, M. Dijkstra, and A. van Blaaderen, *Fabrication of large binary colloidal crystals with a NaCl structure.* Proceedings of the National Academy of Sciences of the United States of America, 2009. **106**(38): p. 16063-16067.
42. Hilhorst, J., V.V. Abramova, A. Sinitskii, N.A. Sapoletova, K.S. Napolskii, A.A. Eliseev, D.V. Byelov, N.A. Grigoryeva, A.V. Vasilieva, W.G. Bouwman, K. Kvashnina, A. Snigirev, S.V. Grigoriev, and A.V. Petukhov, *Double Stacking Faults in Convectively Assembled Crystals of Colloidal Spheres.* Langmuir, 2009. **25**(17): p. 10408-10412.
43. Solomon, T. and M.J. Solomon, *Stacking fault structure in shear-induced colloidal crystallization.* Journal of Chemical Physics, 2006. **124**(13): p. -.
44. Beckham, R.E. and M.A. Bevan, *Interfacial colloidal sedimentation equilibrium. I. Intensity based confocal microscopy.* Journal of Chemical Physics, 2007. **127**(16): p. -.
45. Lu, M., M.A. Bevan, and D.M. Ford, *Interfacial colloidal sedimentation equilibrium. II. Closure-based density functional theory.* Journal of Chemical Physics, 2007. **127**(16): p. -.
46. Hoogenboom, J.P., D. Derks, P. Vergeer, and A. van Blaaderen, *Stacking faults in colloidal crystals grown by sedimentation.* Journal of Chemical Physics, 2002. **117**(24): p. 11320-11328.

CHAPTER 2

PAIR INTERACTION POTENTIALS BY EXTRAPOLATION OF CONFOCAL MICROSCOPY MEASUREMENTS OF COLLECTIVE STRUCTURES

Chapter Summary

An experimental method for measuring the pair interaction potential between colloidal particles is presented. The method is particularly well suited to systems in which the colloid is fluorescent and the colloid and solvent are refractive index matched. The method involves characterization of the potential of mean force between colloidal particles in suspension by measurement of the radial distribution function at multiple particle concentrations. Extrapolation of the potential of mean force computed from the radial distribution function to infinite dilution yields an estimate of the pair interaction potential, $U(r)$. Poly-12-hydroxystearic acid-stabilized poly(methyl methacrylate) (PHSA-PMMA) particles dispersed in the solvent dioctyl phthalate (DOP) were used to test the method and assess its accuracy and precision. Using confocal laser scanning microscopy (CLSM), 3D image volumes of colloidal particles at dilute, equilibrium conditions were collected and analyzed with image processing to determine the radial distribution function. We found a linear relationship between the measured potential of mean force and the volume fraction of the suspension for sufficiently dilute conditions. Signal-to-noise, particle stability, and polydispersity effects can complicate interpretation of the data and these effects were studied in the PHSA-PMMA system. We evaluated the

performance of three different systems interacting through repulsive forces, the range of which had been manipulated by addition of electrolyte.

2.1. Introduction

The pair interaction potential, *U(r)*, characterizes the potential energy change that results as two isolated particles are brought from an infinite to a finite separation. In colloidal suspensions, the pair interaction potential, mediated through a liquid solvent, and the volume fraction, determine the phase behavior [1]. Thus, characterization of *U(r)* of colloidal particles is helpful to predict conditions necessary for the assembly of different colloidal phases. For example, tuning of the pair interaction potential of colloids of opposite charge yields colloidal crystals with ionic structures such as NaCl and CsCl [2]. Arrays of colloids produced by self-assembly have potential applications in photonic band gap materials [3], periodic dielectrics [4, 5], and chemical and biological sensing [6].

Colloidal systems may undergo crystallization because of the effects of packing and excluded volume [7], charge [8], or weak attractions [9]. Often, colloidal systems that are useful for self-assembly are approximately refractive index matched. This matching minimizes strong attractive interactions due to van der Waals forces, which tend to trigger gelation and irreversible aggregation. Moreover, for colloids that are refractive-index matched, fluorescent and approximately 1μm in size, fluorescence or confocal microscopy methods can be used to characterize structure and order in such colloidal suspensions [10].

Common techniques for measuring *U(r)* between pairs of colloids include colloid probe atomic force microscopy (AFM) [11, 12], the surface force apparatus [13, 14], total internal reflection microscopy (TIRM) [15, 16], and optical tweezers [17, 18]. Each of these techniques allows for the direct measurement of the pair interaction potential between isolated particles and surfaces. While these techniques provide valuable information about colloidal interactions, their application to the problems of colloidal assembly as discussed above are limited because they do not characterize interactions between colloids or because they cannot characterize interactions for the particular case of refractive index matched systems. For example, colloid probe AFM, TIRM, and surface force apparatus measure interactions between a colloid and a surface. The interaction between pairs of colloidal particles is more relevant to the understanding of how colloids will assemble. Moreover, the methods of TIRM as well as optical tweezers are not generally applicable to refractive index matched colloidal systems since these techniques require refractive index contrast for optimal performance.

Techniques to infer pair potentials from the collective structure of colloidal fluids address some of the aforementioned limitations, particularly the need for a method that directly probes the interactions between colloids. These methods are complementary to the previously discussed ones because they can often be performed on the exact system that will be used in self-assembly. For example, Royall et al. [19] used confocal microscopy to acquire 3D image volumes of concentrated suspensions ($0.045 < \phi < 0.055$) of colloidal particles. By assuming a form for *U(r)*, the effective pair potential was determined using Monte Carlo (MC) simulations. Hsu et al. [20] approached the problem

by using bright-field microscopy. Using a quasi-2D methodology, they captured many statistically independent images of particles interacting with one another, and then computed the 2D radial distribution function, *g(r)*, to extract the pair potential. To corroborate their results, they employed a MC simulation to calculate *g(r)* and compare with their experimental results. Wu and Bevan [21] took advantage of TIRM and video microscopy to capture the interaction forces between the particles. In this case colloidal pair interactions were assessed by first separating out the additional contribution of the surface that is present in TIRM studies. Finally, Lu et al. [22], to support studies of gelation, parameterized short-range attractive potentials of micron-sized colloids by comparing measurements of the second virial coefficient and the cluster mass distributions to the results of MC simulations.

Here we evaluate the degree to which a method based on the extrapolation of the potential of mean force, *W(r)*, in dilute colloidal suspensions is an accurate and precise characterization of *U(r)*. Specifically, we make use of the fundamental relationship between the radial distribution function, *g(r)*, and the potential of mean force, $W(r)$ [23]:

$$W(r)/k_bT = -\ln[g(r)] \qquad (2\text{-}1)$$

where k_b is the Boltzmann constant, and T is the temperature. $W(r)$ is density dependent. To determine the pair potential, *U(r)*, we extrapolate equation 2-1 to the limit of infinite dilution:

$$\frac{U(r)}{k_B T} = \lim_{\phi \to 0} [-\ln g(r)] \qquad (2\text{-}2)$$

Equation 2-1 is the basis of several recent reports of pair potential characterization by video [23] and confocal laser scanning microscopy [19, 24, 25]. In these papers, $g(r)$ was determined from the microscopy data at a particular volume fraction and equation 2-1 was applied to arrive at an effective pair potential [19, 23, 24] by evaluation at finite volume fraction. That is, the method of these papers assumes that at dilute concentrations the potential of mean force approximates the pair potential.

The difference between these papers and the method discussed in this work is that here equation 2-2 is used to extrapolate measurements at multiple dilute volume fractions to infinite dilution. To our knowledge, our work is the first to pursue an experimental extrapolation of measurements of *g(r)* and *W(r)*. A particular advantage of applying equation 2-2 is that the method requires no apriori assumption of the functional form of the pair potential that the system exhibits. That is, it provides a purely empirical, experimentally based assessment of *U(r)*.

Another key attribute of our work is that it takes advantage of the 3D direct visualization capability of confocal microscopy. Confocal laser scanning microscopy (CLSM) is a technique that images a three-dimensional volume of a sample by acquisition of a stack of 2D images [26]. Previous studies have taken advantage of CLSM to study the interaction potential [19, 27-29]. While 2D methods are capable of measuring interactions of particles, these methods typically require model interpretation and may

suffer from poor signal to noise at dilute conditions because fewer particle pairs are available for analysis. Methods, such as the one reported here, that are 3D in nature help to fill in this important gap.

Thus, the extrapolation to infinite dilution of confocal microscopy measurements analyzed according to equation 2-2 represents a route to characterization of pair interactions that is particularly relevant to colloids dispersed in refractive indexed matched solvents. To evaluate the usefulness of this approach, we apply the method to a refractive index matched charge-stabilized colloidal system and evaluate potential limitations to the method, including effects of signal to noise, phase instability, and polydispersity. For example, potentially large signal to noise in measurements of $g(r)$ at very low volume fractions could introduce error into the extrapolation to infinite dilution required to apply equation 2-2. Phase instability and/or gelation could lead to errors because equation 2-2 assumes a single equilibrium phase in the system. Polydispersity in the particle size could affect the experimental potential due to the effect of small variations in radial separation between the particles. Systematic errors in quantitative image processing used to determine coordinates used to extract the potential of mean force could furthermore affect results [30-32]. Finally, the pair potential could be a function of ϕ itself [33]. This effect would impact the applicability of any dilute characterization method, since assembly typically proceeds at high volume fractions.

In this work, we describe a general procedure for the determination of the pair interaction potential, $U(r)$ that addresses the potential weaknesses raised above. To address the

limiting nature of equation 2-1, we use linear regression to extrapolate the potentials of mean force, $W(r)$, themselves obtained from *g(r)* measurements, at finite concentrations to infinite dilution. To address signal to noise issues, we collected a number of image volumes at each volume fraction to establish a relationship between the relative error of the measured *g(r)* and parameters of the experimental design such as number of particles imaged, colloid volume fraction, and spatial resolution of *g(r)*. To address the complication of phase stability, tests were performed to establish that suspensions studied were all a single, equilibrium phase. Finally, to address potential effects of polydispersity, simulations were performed (by Iacovella and Glotzer) to determine the degree to which this parameter affects the performance of equation 2-1 at infinite dilution.

2.2. Materials and Methods

2.2.1. Synthesis and Characterization of PHSA-stabilized PMMA Particles

Fluorescently labeled poly(methyl methacrylate) particles stabilized by poly-12-hydroxysteric acid (PHSA) were synthesized using an adaptation of the methods of Antl et al. [34], Campbell and Bartlett [35], and Pathmamanoharan et al. [36], and as discussed by Solomon and Solomon [29]. Particles were labeled using Nile red dye. The size of the colloids was analyzed scanning electron microscopy (SEM). The distribution of particle diameters, determined from analysis of 100 particles, is plotted in Figure 2.1. From the best fit of the normal distribution, we determined the mean diameter to be 951nm ± 38nm.

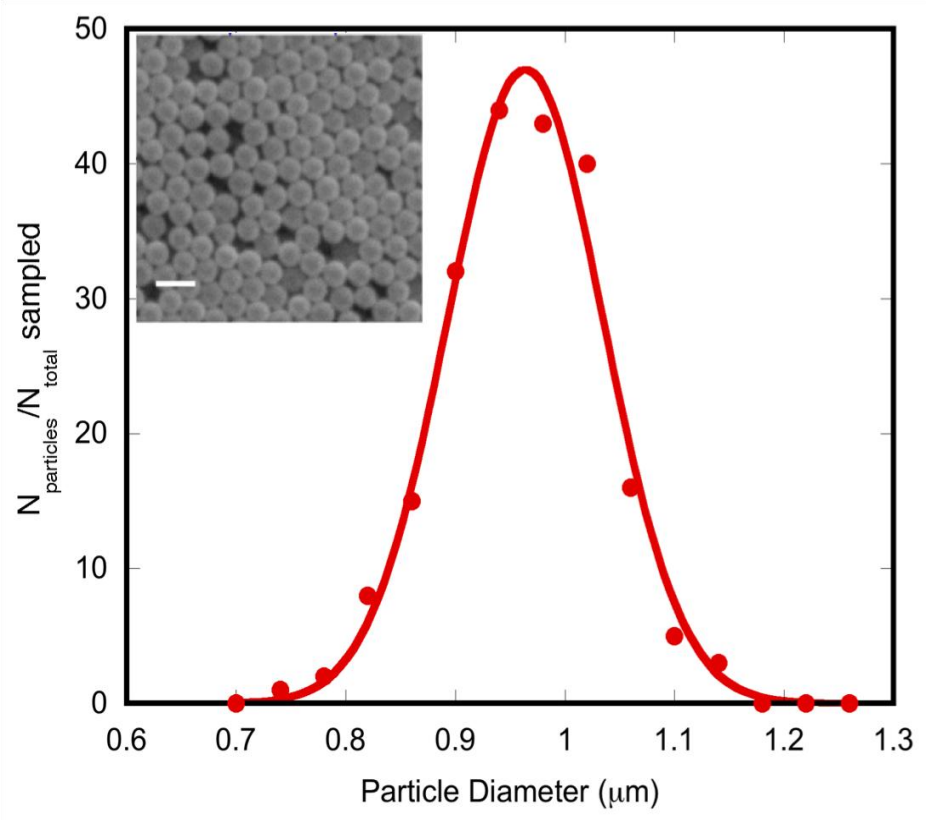

Figure 2.1: Distribution of diameters of PHSA-PMMA particles used in this study. Inset is SEM image of PHSA-stabilized PMMA particles used to generate the distribution. Particles have a diameter of 951nm. Scale bar represents 2μm.

Previous work has shown that PHSA-PMMA colloids in cyclohexyl bromide (CHB) and decalin are charged [37]. Solomon and Solomon also reported particle charging for these particles in dioctyl phthalate [27]. Such colloidal systems have been modeled by a pair potential of the form:

$$\frac{U(r)}{k_B T} = \frac{Z^2 \lambda_B}{(1+\kappa\sigma/2)^2} \frac{e^{-\kappa(r-\sigma)}}{r} \qquad (2\text{-}3)$$

where Z is the charge number, λ_B = Bjerrum length (11 nm for the system studied here), κ is the inverse Debye length, σ is the particle diameter, and r is the center-to-center separation [2].

Parameters in equation 2-3, estimated by experiment, are reported in Table 2-1. The Debye length, κ^{-1}, was estimated from conductivity measurements. Briefly, solutions of DOP containing 2mM of tetrabutylammonium chloride (TBAC) salt were prepared and their conductivity measured (Model EW-01481-61, Cole-Parmer, USA). Using Walden's rule [38], the ion concentration was determined and the inverse Debye screening length was calculated using the equation

$$\kappa = \sqrt{8\pi\lambda_B \rho_i} \qquad (2\text{-}4)$$

where ρ_i is the density of the cation or anion [10]. For the salt-free DOP solvent, the Debye length was estimated to be 444nm based on previous work where the conductivity of pure DOP was measured [39]. For DOP containing 10μM TBAC, the conductivity was estimated by computing the equilibrium constant, K_{eq}, of the dissociated ions in solution at 2mM TBAC. At 2mM TBAC, the conductivity was measured to be 0.004μS/cm. From this conductivity, K_{eq} was calculated to be 2.75×10^{-9} M. Based on this value for K_{eq}, the conductivity of DOP containing 10μM TBAC was estimated to be 2.85×10^{-4}μS/cm. This conductivity translated into an estimated Debye length of 189nm.

Table 2-1 – Characteristic parameters for PHSA-stabilized PMMA particles

	σ_{SEM} (nm)	σ_{CLSM} (nm)	κ^{-1} (nm)	ζ (mV)	Z_{CLSM} $Z = \frac{4\pi\varepsilon_r\varepsilon_0(\sigma/2)\zeta(1+\kappa\sigma/2)}{e}$	ε_{CLSM} $\varepsilon = \frac{Z^2\lambda_B}{\sigma_p(1+\kappa\sigma_p/2)^2}$
No TBAC	951 ± 38	1001 ± 30	444	-28	-105	27
10μM TBAC	951 ± 38	1001 ± 30	189	-30	-194	31
2mM TBAC	951 ± 38	1001 ± 30	49	-32	-635	35

The charge number of the PHSA-stabilized PMMA particles was determined from measurements of their electrophoretic mobility (Zetasizer Nano Series, Malvern, United Kingdom). Particles were prepared as 1 vol% solutions in DOP solutions TBAC concentration equal to 0 (pure solvent), 10μM, and 2mM. Solutions were placed in a dip cell designed for non-aqueous solvents. A voltage of 50mV was applied to each sample. A total of three measurements with 150 sub-runs were taken for each sample to determine variability in the mobility. Using the Debye length and measured mobility, the ζ-potential was determined by the method of O'Brien & White [40]. The charge number on the particles was determined from:

$$Z = \frac{q}{e} = \frac{4\pi\varepsilon\varepsilon_0(\sigma/2)\zeta(1+\kappa\sigma/2)}{e} \qquad (2\text{-}5)$$

where Z is the charge number, q is the particle charge, e is the charge on an electron, ε_0 is the permittivity in a vacuum, ζ is the zeta potential, κ is the inverse Debye screening length, and a is the particle radius, the charge was calculated [41].

Because PMMA colloids may swell in organic solvents [27], we compared the SEM diameter to direct measurements of the colloid size in solution. To perform the comparison, we prepared a sample at a high TBAC salt concentration of 50mM to induce aggregation of the particles in the solvent. A CLSM image volume was acquired and the separation between particle pairs was computed by image processing per the method described subsequently. We found the particles swelled approximately 5% from a SEM particle size of 951 ± 38 nm to a CLSM particle size of 1001 ± 30 nm.

2.2.2. Sample preparation and image volume collection

The PMMA-PHSA particles (RI = 1.489) were dispersed in DOP (RI = 1.485) containing no salt, 10μM TBAC salt or 2mM TBAC salt. Samples for the no salt case were prepared at nominal volume fractions of 0.005, 0.01, 0.015, 0.02, 0.03, 0.04, and 0.05; however, precise estimation of the volume fraction was made from the results of quantitative image processing discussed in Section 2.2.3. Samples were mixed for about 45 s using a vortex mixer and a sonication bath. After the initial mixing, the samples were allowed to equilibrate for 24 hours. Samples were then gently remixed and subsequently transferred to glass specimen vials (O.D. = 12mm) that were adhered to a microscope cover slip using ultraviolet bonding glue (Dymax Corporation, United

States). The cover slip was attached to a 35mm O.D. glass ring made from Pyrex standard wall tubing. To assess the stability of this colloidal system, samples prepared at a volume fraction of 0.005 in the DOP solvent were monitored for 24 hours for signs of phase instability. No aggregation or phase instability was observed.

Sample imaging was performed on a Leica TCS SP2 confocal microscope (Leica Microsystems, Wetzlar, Germany). A 100x oil immersion objective with numerical aperture 1.4 was used. The particles were dyed with Nile red (Sigma-Aldrich, United States) and were excited with a green neon (GreNe) laser beam (λ_0 = 543nm). Emission from 550nm to 650nm was collected. To avoid possible effects of sample boundaries on particle configurations, all points in the image volumes were located at least 20μm from any boundary of the specimen vial. Stacks of 247 images with a resolution of 512 x 512 pixels were obtained and processed to extract particle centroids as described in the next section. Images were acquired with a spatial resolution of 69.2 x 69.2 nm/pixel in the objective plane and an axial separation of 81.4nm. Thus, the size of the image volume was 35 x 35 x 20 μm^3. Figure 2.2 shows images for each of the volume fractions used for the case of pure DOP with no added salt.

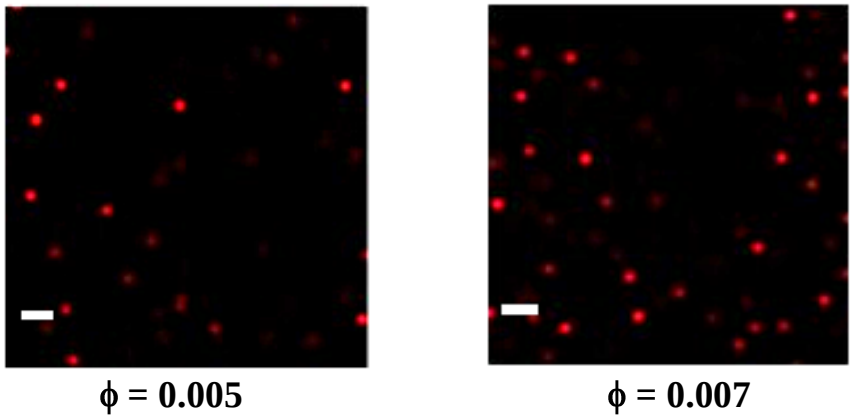

ϕ = 0.005

ϕ = 0.007

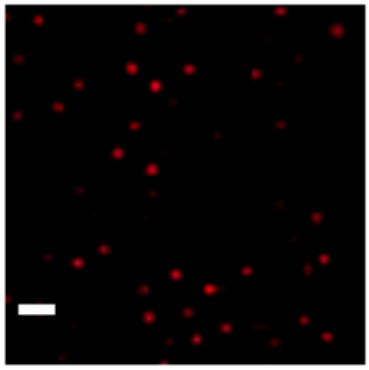

ϕ = 0.008

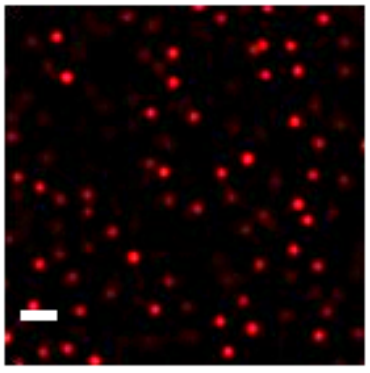

ϕ = 0.012

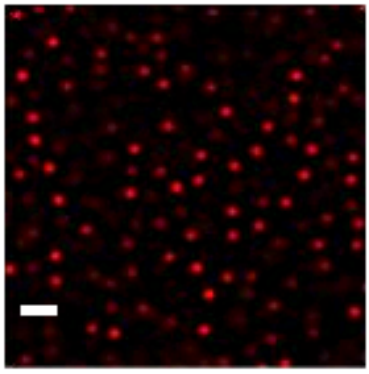

ϕ = 0.018

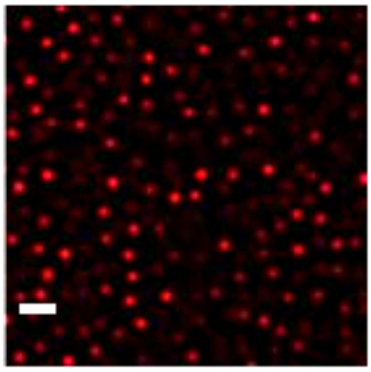

ϕ = 0.022

Figure 2.2 – CLSM images of PMMA-PHSA particles in pure DOP with diameter of 1μm. Images were taken using a green neon (GreNe) laser (λ_0 = 543nm). Scale bar on all images is 3μm

2.2.3. Image Processing and Calculation of g(r)

To identify particle locations, we used image processing algorithms based on the work of Crocker and Grier [42] as discussed in Dibble et al. [43]. The procedure is divided into three steps. First, a Gaussian filter is applied to the 3D image volume. Second, particle centers are identified using a local brightness maximum criterion. That is, a voxel is identified as a candidate centroid if it is within a local cubic region of half-width *w*. For our systems and imaging conditions, $w = 7$. Finally, using the moments of the local intensity distribution, particle positions are refined to subpixel accuracy [42]. For our system, the accuracy is ±35 nm in the *x*-*y* plane and ±45 nm in the *z* direction [43]. After centroids were identified, the radial distribution function, *g(r)*, was determined by computing the separation between all particle pairs. We assessed the performance of the image processing algorithm by examining composite images for which centroid locations were overlaid on the fluorescence images. From these images, we determined the algorithm had identified nearly all of the particle centroids.

2.3. Results

2.3.1. Radial Distribution Function

Figure 2.3 shows the average *g(r)* of PMMA/PHSA particles in pure DOP for each volume fraction used in this study. The data plotted in Figure 2.3 are averages of independent measurements at multiple volumes in the specimen. For the three lowest volume fractions ($\phi = 0.005$, 0.007, and 0.008), multiple samples were used to collect additional data and increase the sample size for statistical purposes. Table 2-2 lists the number of particles and image volumes included in the average of each *g(r)* curve. The

bin shell size of the radial distribution function was selected to be 0.1μm (about 10% of the particle diameter) to balance the competing constraints of signal to noise and spatial resolution of the potential. At these charge and solvent conditions, we observed no particles in the inner most shells of *g(r)*. This result is consistent with repulsive pair interactions, as previously reported [19, 37] for similar systems. For the four lowest volume fractions, pair separations were found with r < 2μm. As the volume fraction increased above 0.012, some particle pair separations were found for r < 2μm. This indicated an increase in the local density of the particles. Error bars represent the standard error of the mean *g(r)*.

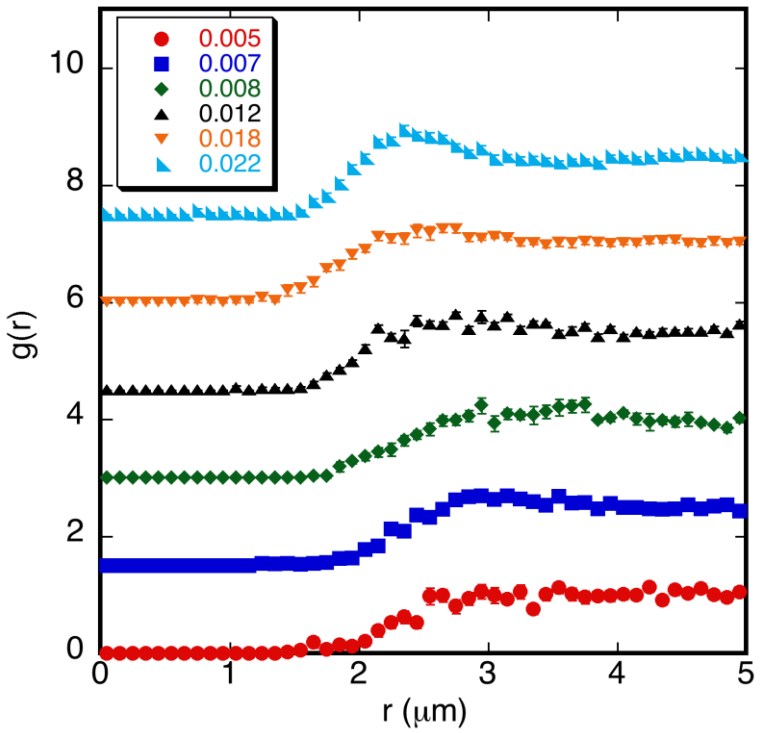

Figure 2.3 – Radial distribution functions for PMMA/PHSA particle system in pure DOP

Table 2-2 - Total number of particles and image volumes used for potential characterization in pure DOP.

Volume Fraction	N_{Total}	Total number of image volumes used for *g(r)* curve
0.005	7,216	36
0.007	10,911	26
0.008	5,772	12
0.012	4,686	6
0.018	6,842	6
0.022	8,279	6
0.042	15,997	6

2.3.2. Determining the Dilute Limit

The potential of mean force, *w(r)*, computed by application of equation 2-1 to the data of Figure 2.3, is plotted in Figure 2.4 for the pure DOP system with $0.005 < \phi < 0.042$. To determine the pair potential according to the approach of equation 2-2, we must extrapolate -ln [*g(r)*] to infinite dilution at each radial position. The curvature in Fig. 2.4a indicates that for this system, with its strongly repulsive interactions, there is a transition from dilute to non-dilute behavior for $\phi \sim 0.018$. The transition point is not abrupt, and appears to be slightly dependent on radial position. Equation 2-2 should only be applied in a dilute limit – that is, in a concentration range where the potential of mean force is a linear function of volume fraction. In Fig. 2.4a, we empirically determine that the dilute limit corresponds to $\phi < \sim 0.018$ and accordingly analyze data below that limit to determine *U(r)*. The dilute transition volume fraction of $\phi \sim 0.018$ is consistent with

simulations of this system: Iacovella and Glotzer [44] determined a transition volume fraction of $\phi \sim 0.02$.

(a)

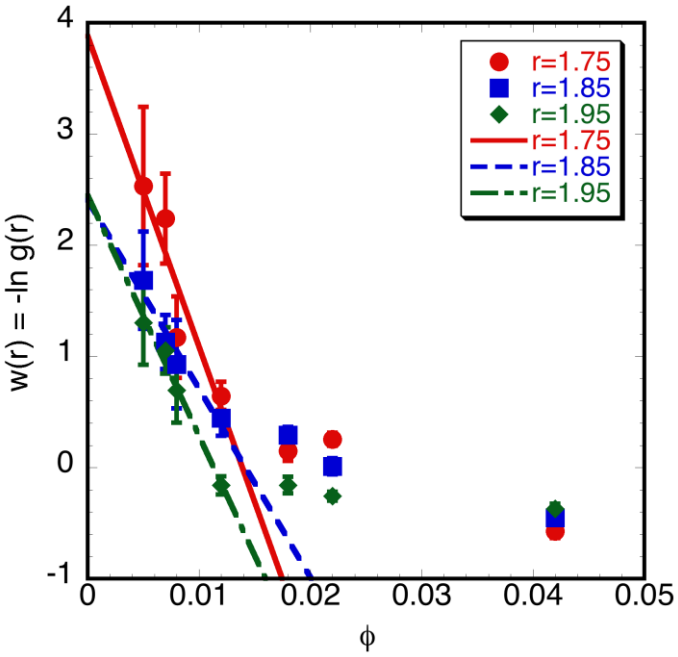

(b)

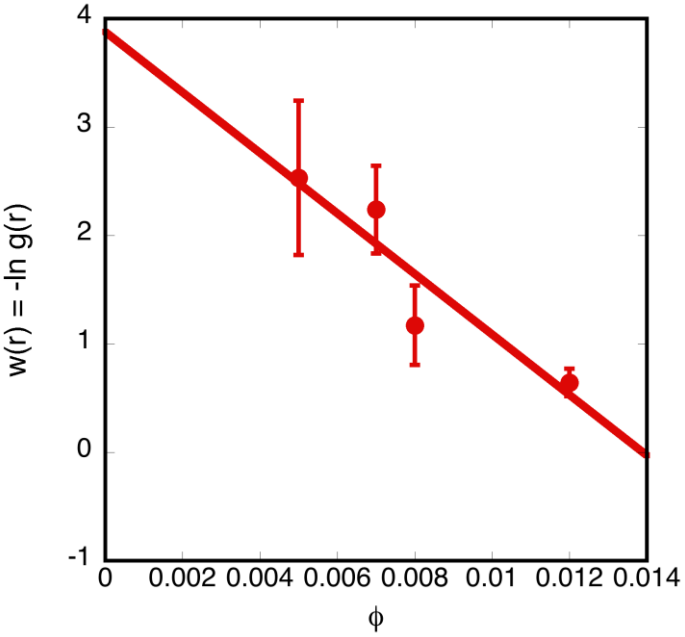

(c)

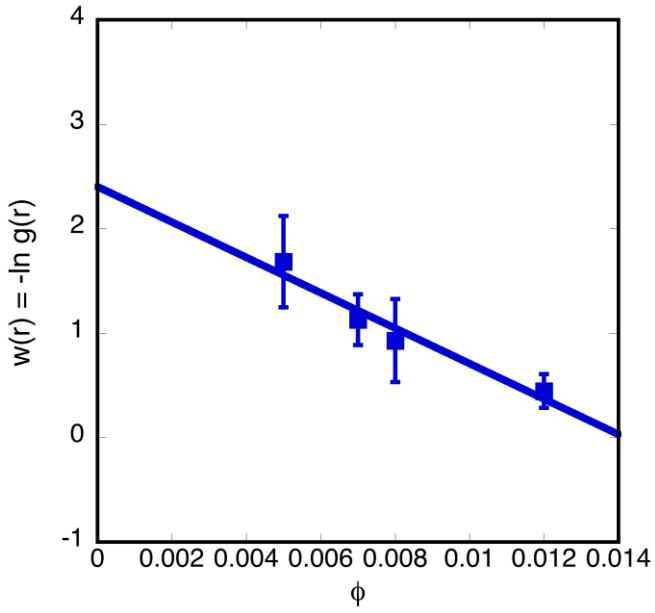

(d)

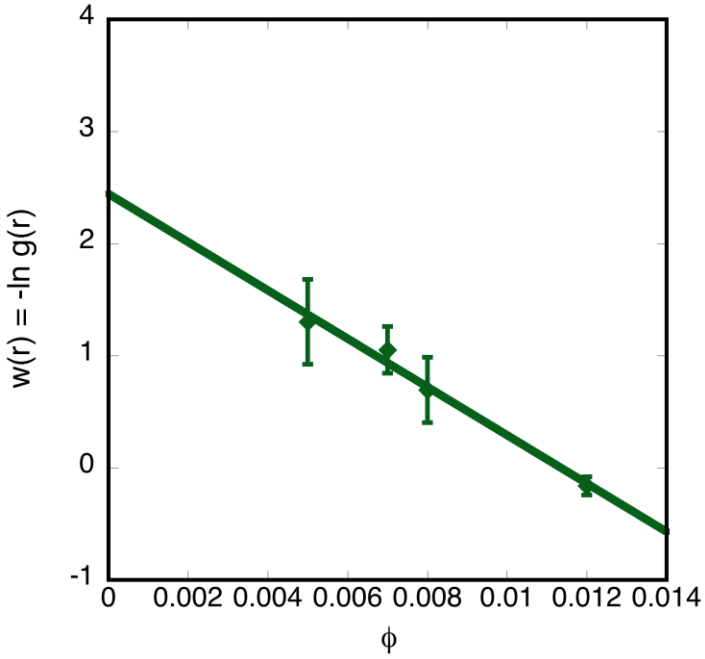

Figure 2.4 – Potential of mean force as a function of volume fraction. In (a), extrapolation has been performed on volume fractions up to $\phi = 0.012$. Above $\phi = 0.018$, *w(r)* moves out of the linear region. Extrapolation to infinite dilution shown for radial positions of (b) r = 1.75μm, (c) r = 1.85μm, and (d) r = 1.95μm.

To determine *U(r)*, extrapolation of the potential of mean force is performed at each radial position, as shown for the particular cases of r = 1.75μm, 1.85μm and 1.95μm in Figures 2.4b-d. The y-intercept of these plots is the infinite dilute result, equivalent to *U(r)* as per equation 2-2. These figures show that the linearity of the data in this volume fraction region is excellent. The error bars represent the propagation of error associated with the extrapolation of –ln *g(r)* to infinite dilution.

The importance of extrapolating the measured *w(r)* to the infinite dilution case can be seen in Figure 2.4. At a given ϕ and radial position, the measured *w(r)* in all cases would be less than the value at the intercept. For example, at r = 1.75μm and ϕ = 0.005, the measured *w(r)* ~ 2.5; however, the value of *w(r)* at the intercept is ~ 4. The difference between the actual value at the intercept and the single point measurement is approximately 37%. This significant systematic error demonstrates the extrapolation method of equation 2-2 is preferred over single point measurements such as would result for application of equation 2-1 at a single volume fraction.

2.3.3. Experimental Pair Interaction Potential

Figure 2.5 shows the experimental pair interaction potential measured for PHSA-PMMA in the solvent pure DOP per the extrapolation method discussed in the previous section. *U(r)* is qualitatively consistent with long range repulsive interactions, consistent with reports of others for similar systems [37]. Error bars plotted are standard error of the mean. They show that the precision of the data set is very good.

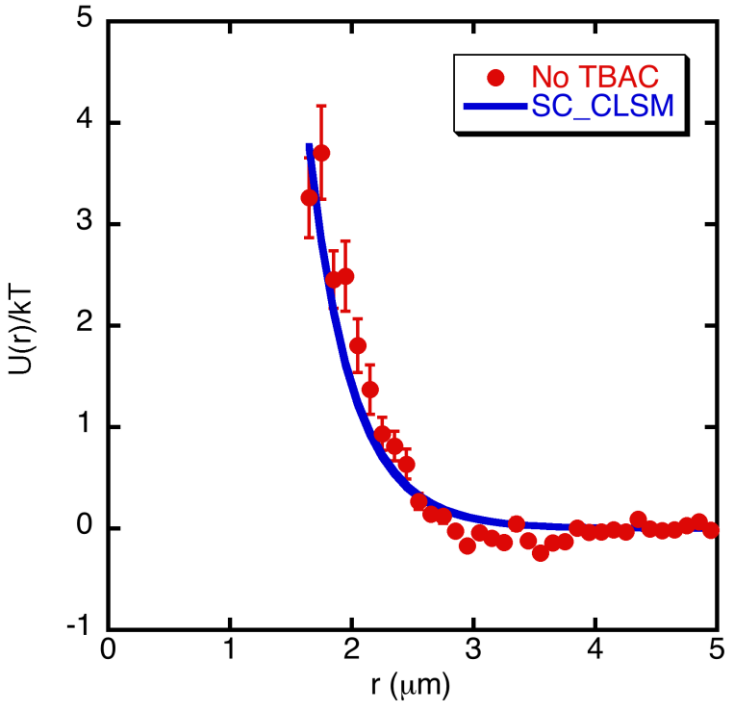

Figure 2.5 – Experimental pair interaction potential for PMMA/PHSA particle system in pure DOP. Screened Coulomb potential for CLSM particle diameter has been overlayed on experimental potential.

To assess the degree to which the measurements are consistent with the Table 1 characterization parameters and repulsive interactions, we compare the data to predictions for the screened Coulombic potential, equation 2-3. Figure 2.5 shows that the agreement between the theoretical prediction (derived solely from independent measurements of colloid electrokinetics) and the experimental data (derived solely from the confocal microscopy measurements) is very good. One ambiguity in the comparison is uncertainty in characterization of the particle diameter, which enters into equation. 2-3, but which could be taken as either the value from SEM or from CLSM. However, this ambiguity has only a small effect on the result of equation 2-3. A full discussion on the differences between the SEM and CLSM particle diameters is presented in section 2.4.2.

From the inspection of the error bars, the Figure 2.5 data are precise, an indication that sufficient statistics were acquired in the confocal microscopy experiments. (The number of image volumes and particles for each volume fraction is given in Table 2-2.) General application of the method requires that sufficient particle pairs be acquired for construction of the radial distribution functions used in the extrapolation. Figure 2.6 summarizes the relationship between the precision of the measured *g(r)* and properties of the experiments, including the number of particles found, the volume fraction of the specimen, and the bin size of each point in *g(r)*. We see that the error in *g(r)* is a weak function of the combination $N^*\phi^*\Delta r$, scaling as power law with exponent ~ -0.79.

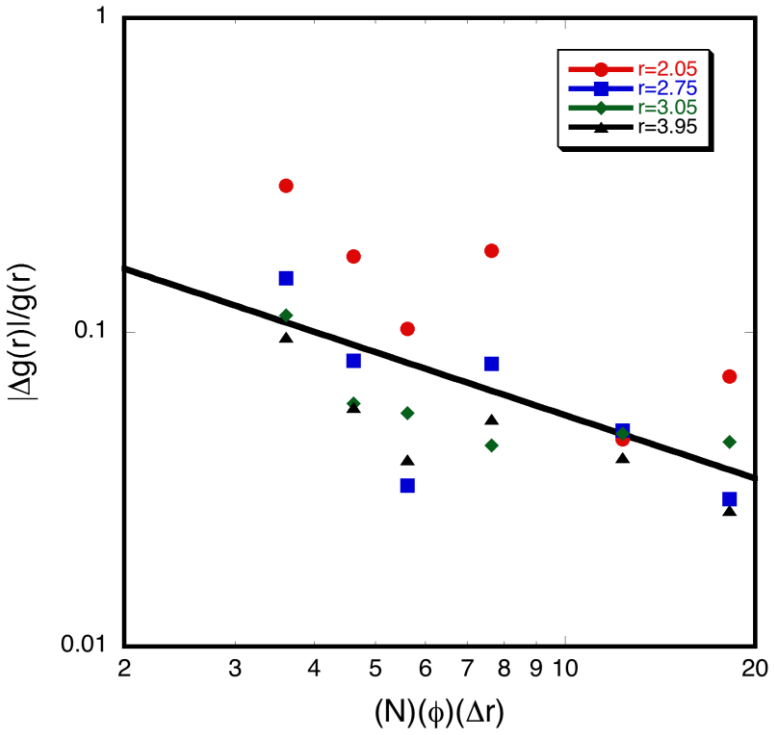

Figure 2.6: Error analysis of *U(r)/kT* as a function of number of particles, volume fraction, and bin size for pure DOP case. Data taken from four different radial (*r*) positions, units of microns. Line drawn is power law fit to the data with a slope of -0.79. Bin shell size (Δr) held constant at 0.10 μm/bin.

The particular combination of variables plotted on the abscissa, N*ϕ*Δr, was suggested by the simulations of Iacovella and Glotzer. That each variable in the combination should affect precision is clear: First, N should appear because as the total number of particles increases the statistics included in *g(r)* increases and signal to noise is also improved. Second, the statistics of *g(r)* improves as the number of pairs counted increases. The number of pairs counted is proportional to the product N*ϕ. Third, Δr appears because the total number of pairs counted is distributed among the number of

bins which are inversely related to their width. Iacovella also found a power law dependence, but with slope -0.56. Figure 2.6 can be applied to determine experimental conditions for pair potential characterization. For example, for a relative error of ~ 10% in the radial distribution, Figure 2.6 requires $N^*\phi^*\Delta r \sim 4$. For a volume fraction ~ 0.01 of 1 μm particles in which *g(r)* is resolved at ~ 10% of the colloidal size, this relative error would require measurements on the order of 4,000 particles.

2.3.4. Measurement of Pair Interaction Potential of Screened Systems

To assess the extent to which the method can resolve differences in pair potential interactions that are relevant for self-assembly, we performed experiments in which the repulsive interactions observed in Figure 5 were reduced by addition of electrolyte. Figures 2.7 and 2.8 show measured *g(r)* for cases where the repulsion between the particles had been screened by addition of TBAC at concentrations of 10μM and 2mM, respectively. Recall from Table 1, the Debye length for these three conditions is 49nm for the 2mM case, 189nm for 10μM case, and 444nm for the pure DOP. We prepared samples using macroscopic volume fraction ranging from 0.02 to 0.08. Again, the actual volume fractions were determined from image processing. Tables 3 and 4 list the number of particles and image volumes included in the average of each *g(r)* curve. To ensure the samples did not become unstable after dispersing the PMMA particles in DOP with TBAC, CLSM images were taken 24 hours after preparation. Just as for the experiments with no added TBAC, we observed no signs of particle aggregation.

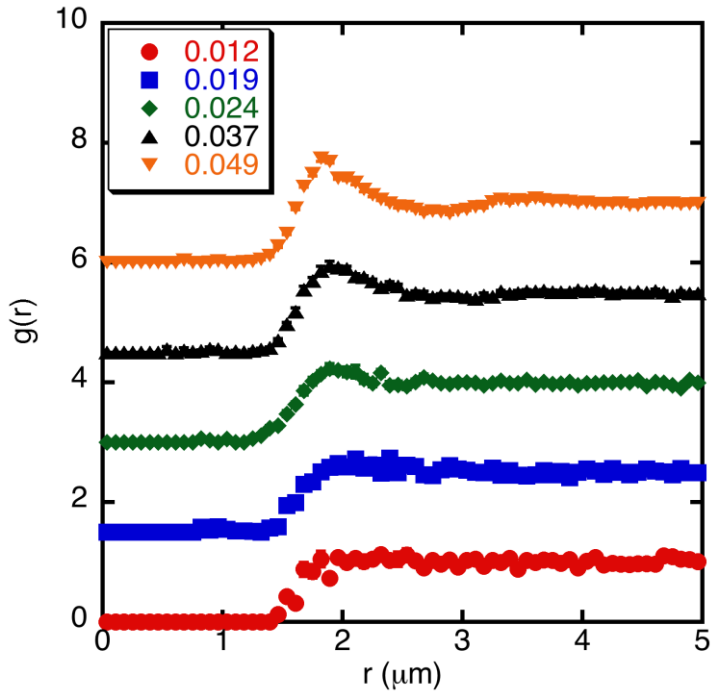

Figure 2.7 – Radial distribution functions for PMMA/PHSA particle system in DOP with 10μM TBAC (curves offset for clarity). Each curve represents g(r) at a volume fraction ranging from 0.012 to 0.049 as determined by image processing.

Table 2-3 – Total number of particles and image volumes used for potential characterization in DOP with 10μM TBAC added.

Volume Fraction	N_{Total}	Total number of image volumes used
0.012	6,646	10
0.019	8,331	8
0.024	10,434	8
0.037	12,183	6
0.049	16,116	6

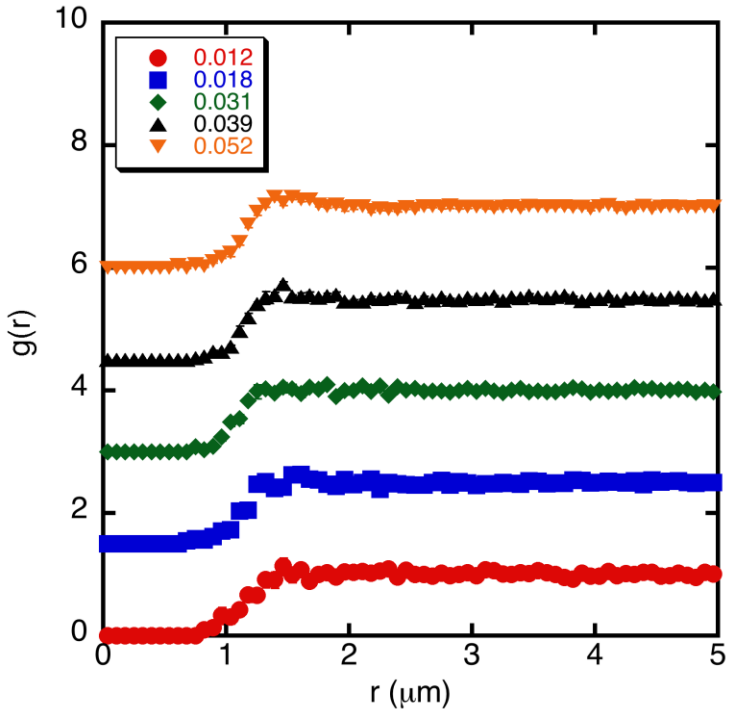

Figure 2.8 – Radial distribution functions for PMMA/PHSA particle system in DOP with 2mM TBAC (curves offset for clarity). Each curve represents g(r) at a volume fraction ranging from 0.012 to 0.052 as determined by image processing.

Table 2-4 – Total number of particles and image volumes used for potential characterization in DOP with 2mM TBAC added

Volume Fraction	N_{Total}	Total number of image volumes used
0.012	10,568	14
0.018	13,508	12
0.031	10,196	6
0.039	12,453	6
0.052	15,129	6

For both TBAC concentrations, we observed that the onset of finite *g(r)* shifted to smaller radial distances. This shift qualitatively indicates that TBAC addition was moderating repulsive interactions in the system. The shift also affects the limit of linearity (discussed in Figure 4 for the case of no added TBAC). For example, for [TBAC] = 10 μM, linearity is found for $\phi < 0.05$. For [TBAC] = 2 mM, linearity was found for $\phi < 0.06$ in the experiments. Comparing to the case of pure DOP, where linearity is found for $\phi < 0.018$, these results for the two TBAC cases are consistent with an expected shift due to an increase in the screening of the repulsive interactions. Iacovella has assessed, from simulation, limits of linearity for the potential of mean force, *w(r)*. The highest limit occurs in the case of simple excluded volume (Weeks Chandler Anderson) interactions. In this case, linear extrapolation of the potential of mean force is possible for $\phi < 0.2$. Therefore, our findings are well within the limits as determined from simulations.

Figure 2.9a compares the experimental pair potential for the three systems. CLSM images provide a comparison of particle separations for the three cases studied in this work. The pair potentials were again extracted by application of eqn. (2) below the extrapolation limits discussed above. Interesting, the results for the high salt concentration (2mM TBAC) are nearly consistent with a simple excluded volume interactions – the transition to the repulsive portion of the potential is abrupt and very close to the measured diameter of the colloid. This abrupt transition is consistent with the electrokinetic characterization – the Debye length of this condition is 49 nm. Thus, screened electrostatic interactions extend no further than about 5% of the particle diameter, not too difference from the spread in the particle size distribution due to

polydispersity. That the 10μM pair potential falls between the two cases of pure DOP and 2mM TBAC is consistent with expectations based on the screened electrostatics. Figures 2.9b-d are CLSM images that show the difference in particle separations in the three different TBAC cases for a volume fraction of 0.012. For the pure DOP, a wider separation between particles was observed at all volume fractions. The introduction of TBAC reduced the particle separations as can be seen in (c) and (d).

(*a*)

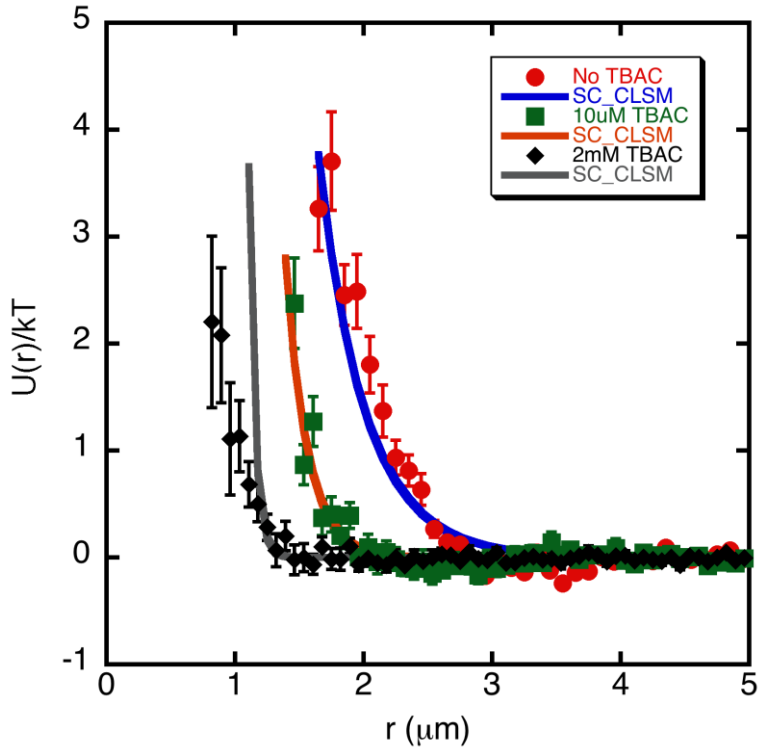

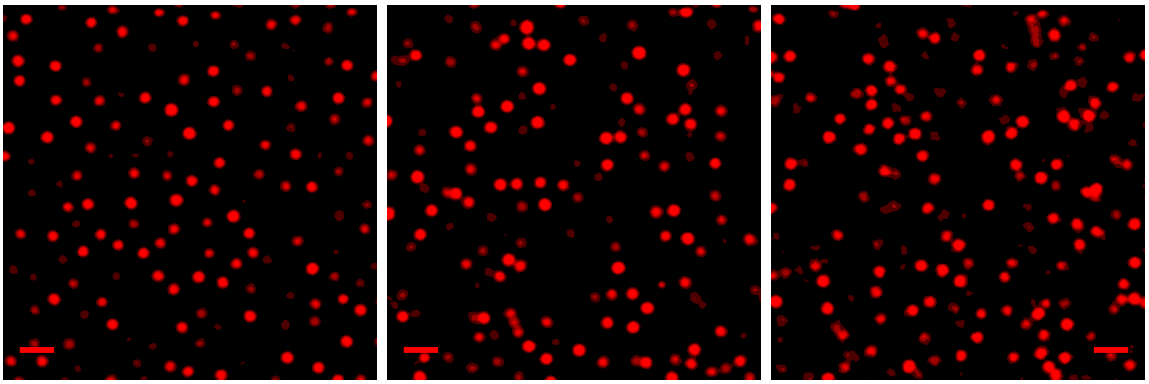

(*b*) (*c*) (*d*)

Figure 2.9 – a) Experimental pair interaction potential for PMMA/PHSA particle system containing no TBAC, 10μM TBAC, and 2mM TBAC. Screened Coulombic potential has been overlayed on experimental potentials. Characterization data for PMMA-PHSA particles in pure DOP and DOP containing 10μM and 2mM TBAC were used to compute screened Coulombic potentials. CLSM images show particle separations at $\phi = 0.012$ in b) pure DOP; c) DOP with 10μM TBAC; and d) DOP with 2mM TBAC. Scale bar in images is 3μm.

2.4. Discussion

2.4.1. Conductivity Measurements for DOP

The Debye lengths presented in Table 2-1 were calculated based on the conductivity of DOP containing no TBAC, 10μM TBAC, and 2mM TBAC salt. In our analysis of the conductivity, we found that DOP had a very low conductivity ($\leq \sim 10^{-3}$ μS/cm). It was very difficult to get a precise reading of the conductivities for the pure DOP and DOP with 10μM TBAC cases using our conductivity meter. We were able to get a conductivity reading for the highest salt concentration. To make full use of the screened Coulomb equation, we chose to calculate the conductivity of the no TBAC and 10μM TBAC cases based on literature values (no TBAC case) and the equilibrium constant (10μM TBAC). While we recognize these two approaches did not give us an exact value of the respective conductivities, these approaches did allow us to make valid estimations based on known values. The estimation of the conductivity for the no TBAC case led us to make a one-parameter fit since we were only able to measure the zeta potential of the system. We were still able to do a two-parameter fit for the 10μM TBAC case because the conductivity was computed based on the measured conductivity of the 2mM TBAC case.

We also undertook an alternate approach to measuring the conductivity of DOP. Using a setup typically found in biological studies, we thought it could be possible to access the very low conductivity of our solvent. The Patch-1U Model cell has the capability of measuring very high resistances of materials. A small amount of DOP was place in a petri dish and two electrodes were inserted into the solvent. A voltage (+100mV and -

100mV) was passed across the solvent and the current (in units of picoAmperes) was measured. Using the relation V=I*R, the resistance was determined. Because resistance is the inverse of conductivity, we had direct access to this value. From this test, we determined that the conductivity of the solvent was 5.35×10^{-4} μS/cm, validating the order of magnitude of the conductivity we determined through the fit. The difference in magnitude can be attributed to variation in experimental conditions (e.g. temperature/humidity conditions within the laboratory at time conductivity measurements are recorded).

2.4.2. Comparing SEM to CLSM Particle Size

Previous work with PMMA particles has shown that the particles swell when dispersed in solution [27]. We were interested in determining if such swelling would have an effect on the use of equation 2-3 in comparing theory to the experimental results. Characterization parameters were computed using both the SEM and CLSM particle diameters. These parameters were then used to determine the screened Coulomb potential for both sizes and overlayed on the experimental potential. Figure 2.10 shows U(r)/kT for the no TBAC case with the SEM and CLSM curves overlayed. There is no significant difference in using the SEM particle diameter versus the CLSM particle diameter. We determined the 5% difference in the size did not yield a major variation in subsequent calculations. As such, we chose to use the CLSM particle diameter since all experiments were performed in the DOP solvent.

2.4.3. Comparing Experimental Data to Simulation Results

We utilized simulations as part of this work in order to validate the experimental results and to confirm the validity of the proposed methodology. In this section, we compare key results from both experiments and simulations to demonstrate the consistency between the two methods. Additional simulation results can be found in Appendix B.

Figure 2.10 shows how the simulation results compare with the experimental results for determining the dilute limit for performing linear extrapolation back to infinite dilution. The potential of mean was computed from the relation, $w(r) = -\ln g(r)$, where $w(r)$ is the potential of mean force. A plot of $w(r)$ versus volume fraction was generated. In Figure 2.10a, the simulation results show how $w(r)$ deviates from linearity at higher volume fractions. As previously mentioned, our methodology holds only when $w(r)$ varies linearly with the volume fraction. We should expect to find a similar trend in the experimental results. Figure 2.10b presents the experimental data at a center-to-center separation of 1.95μm. We found a linear relationship between $w(r)$ and ϕ up to $\phi = 0.012$. At $\phi = 0.018$, there was a sharp deviation from linearity indicating the upper limit to the dilute regime had been exceeded. As expected, the experimental data agreed with the simulations results.

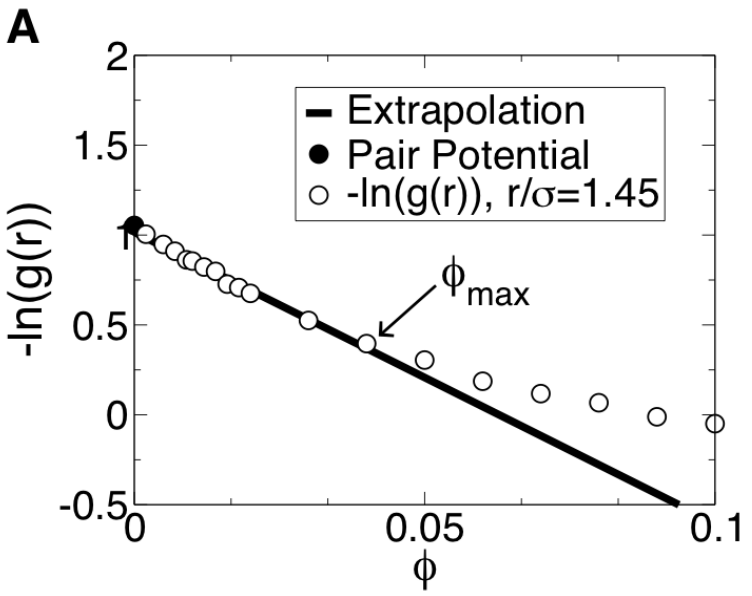

(a)

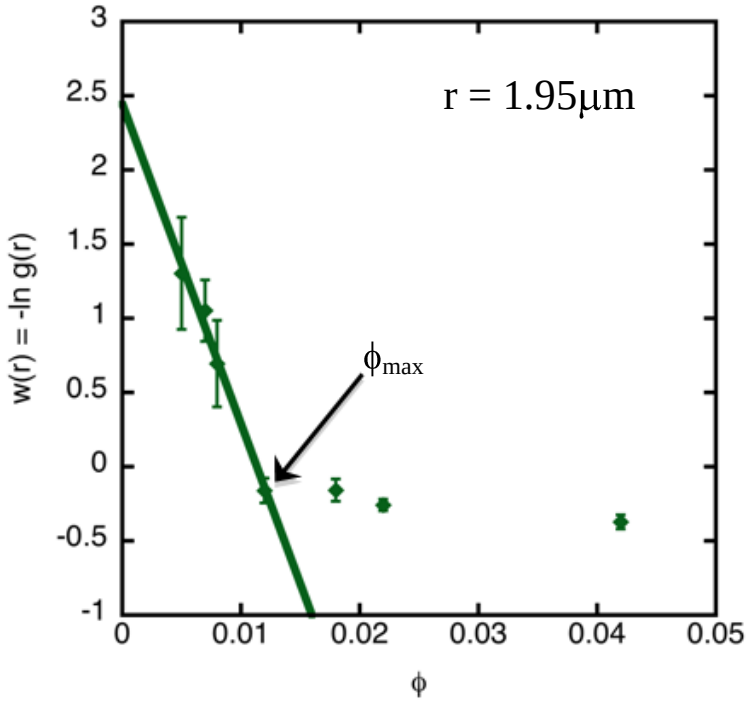

(b)

Figure 2.10 – Potential of mean force, *w(r)*, as a function of volume fraction, ϕ, for (a) simulation and (b) experimental results. For experimental plot, potential of mean force curve is shown for radial position of 1.95μm from center of particle. Figure (a) by Chris Iacovella.

Figure 2.11 shows the results from an examination of the error in the radial distribution function, g(r). We were interested in understanding how the error scaled in relation to the number of particles (N), the volume fraction (ϕ), and the bin shell size (Δr). Essential to accurately determining the pair potential is generating *g(r)* with sufficient accuracy. Due to its construction, *g(r)* is a spherically averaged measure; therefore, we average over more particle pairs as we consider larger particle separations. In other words, our statistics improve as *r* increases. This may be problematic since the pair potential we wish to determine acts the strongest at smaller separations where statistics are poorest. Additionally, since we must compute *g(r)* at low values of ϕ, it is unlikely at such conditions to have many particles interacting at small values of *r* if particles are well distributed in the system (i.e. particles do not aggregate). As such, to determine *w(r)* accurately (and thus *U(r)*), we must establish when we have appropriately gathered sufficient statistics to be confident in *g(r)*. Simulations indicated a power law relationship could be made between the error and the product of N, ϕ, and Δr. Figure 2.11a presents the simulation results. The error, and therefore the accuracy, in *g(r)* was shown to decrease as either N, ϕ, and Δr increased. We plotted the experimental data in the same manner and present the results in Figure 2.11b. We found the same power law trend as was seen in the simulation results. As such, the experimental data was able to validate the findings from simulation.

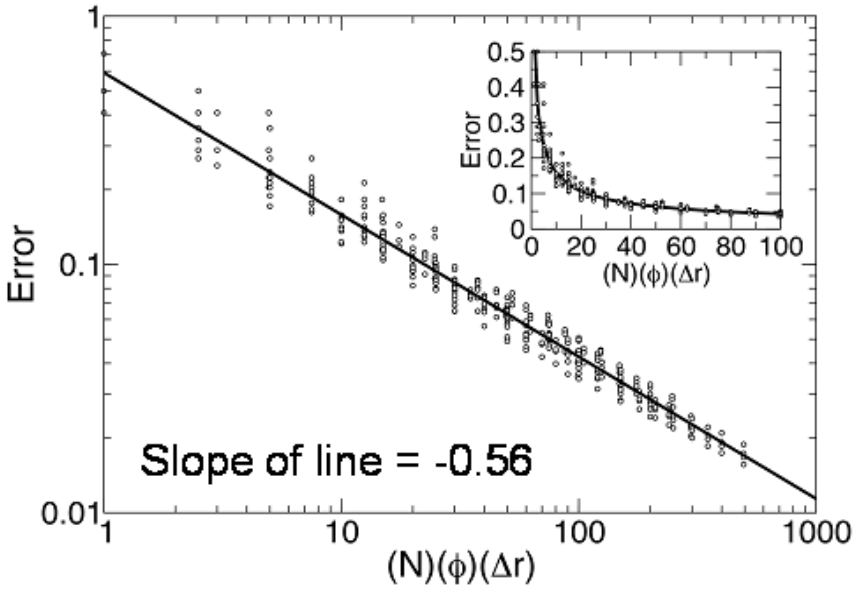

(a)

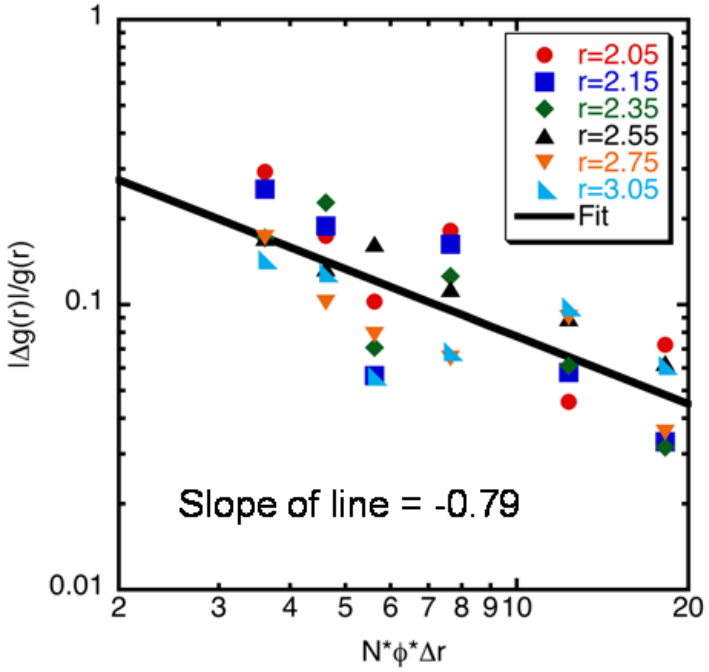

(b)

Figure 2.11 – Error scaling of g(r) for (a) simulations and (b) experiments. Plots show how the error scales as a function of number of particles, volume fraction, and bin size. Figure (a) by Chris Iacovella.

2.5. Conclusion

We have presented a methodology to determine the pair interaction potential of colloidal particles. By using the relationship between the potential of mean force and the radial distribution function, we can systematically calculate the pair potential of our colloidal systems. The key to our methodology relies on the ability to rigorously determine a dilute region where one can extrapolate back to an infinite dilution point and subsequently calculate the pair potential. Using the screened Coulombic potential, we were able to successfully match the experimental potentials to those theoretically predicted. We have shown that signal to noise issues typically found in data at very low volume fractions can be reduced significantly by achieving a set criteria that is a combination of the number of particles and the number of image volumes collected.

References

1. Anderson, V.J. and H.N.W. Lekkerkerker, *Insights into phase transition kinetics from colloid science.* Nature, 2002. **416**(6883): p. 811-815.
2. Leunissen, M.E., C.G. Christova, A.P. Hynninen, C.P. Royall, A.I. Campbell, A. Imhof, M. Dijkstra, R. van Roij, and A. van Blaaderen, *Ionic colloidal crystals of oppositely charged particles.* Nature, 2005. **437**(7056): p. 235-240.
3. Ngo, T.T., C.M. Liddell, M. Ghebrebrhan, and J.D. Joannopoulos, *Tetrastack: Colloidal diamond-inspired structure with omnidirectional photonic band gap for low refractive index contrast.* Applied Physics Letters, 2006. **88**(24): p. 241920.
4. Hosein, I.D. and C.M. Liddell, *Convectively assembled asymmetric dimer-based colloidal crystals.* Langmuir, 2007. **23**(21): p. 10479-10485.
5. Hosein, I.D. and C.M. Liddell, *Convectively assembled nonspherical mushroom cap-based colloidal crystals.* Langmuir, 2007. **23**(17): p. 8810-8814.
6. Hosein, I.D. and C.M. Liddell, *Homogeneous, core-shell, and hollow-shell ZnS colloid-based photonic crystals.* Langmuir, 2007. **23**(5): p. 2892-2897.
7. Pusey, P.N. and W. Vanmegen, *Observation of a Glass-Transition in Suspensions of Spherical Colloidal Particles.* Physical Review Letters, 1987. **59**(18): p. 2083-2086.
8. Sirota, E.B., H.D. Ouyang, S.K. Sinha, P.M. Chaikin, J.D. Axe, and Y. Fujii, *Complete Phase-Diagram of a Charged Colloidal System - a Synchrotron X-Ray-Scattering Study.* Physical Review Letters, 1989. **62**(13): p. 1524-1527.
9. Ilett, S.M., A. Orrock, W.C.K. Poon, and P.N. Pusey, *Phase-Behavior of a Model Colloid-Polymer Mixture.* Physical Review E, 1995. **51**(2): p. 1344-1352.
10. Habdas, P. and E.R. Weeks, *Video microscopy of colloidal suspensions and colloidal crystals.* Current Opinion in Colloid & Interface Science, 2002. **7**(3-4): p. 196-203.
11. Clark, S., J. Walz, W. Ducker, Langmuir, 2005. **21**.
12. Butt, H.J., B. Cappella, and M. Kappl, *Force measurements with the atomic force microscope: Technique, interpretation and applications.* Surface Science Reports, 2005. **59**(1-6): p. 1-152.
13. Israelachvili, J.N., *Intermolecular and surface forces*. 2nd ed. 1992, London: Academic. xxi, 450 p.
14. Schorr, P.A., T.C.B. Kwan, S.M. Kilbey, E.S.G. Shaqfeh, and M. Tirrell, *Shear forces between tethered polymer chains as a function of compression, sliding velocity, and solvent quality.* Macromolecules, 2003. **36**(2): p. 389-398.
15. Bevan, M.A. and D.C. Prieve, *Direct measurement of retarded van der Waals attraction.* Langmuir, 1999. **15**(23): p. 7925-7936.
16. Claesson, P.M., T. Ederth, V. Bergeron, and M.W. Rutland, *Techniques for measuring surface forces.* Advances in Colloid and Interface Science, 1996. **67**: p. 119-183.
17. Furst, E.M., *Interactions, structure, and microscopic response: Complex fluid rheology using laser tweezers.* Soft Materials, 2003. **1**(2): p. 167-185.
18. Sainis, S.K., V. Germain, C.O. Mejean, and E.R. Dufresne, *Electrostatic interactions of colloidal particles in nonpolar solvents: Role of surface chemistry and charge control agents.* Langmuir, 2008. **24**(4): p. 1160-1164.

19. Royall, C.P., A.A. Louis, and H. Tanaka, *Measuring colloidal interactions with confocal microscopy.* Journal of Chemical Physics, 2007. **127**(4): p. -.
20. Hsu, M.F., E.R. Dufresne, and D.A. Weitz, *Charge stabilization in nonpolar solvents.* Langmuir, 2005. **21**(11): p. 4881-4887.
21. Wu, H.J. and M.A. Bevan, *Direct measurement of single and ensemble average particle-surface potential energy profiles.* Langmuir, 2005. **21**(4): p. 1244-1254.
22. Lu, P.J., E. Zaccarelli, F. Ciulla, A.B. Schofield, F. Sciortino, and D.A. Weitz, *Gelation of particles with short-range attraction.* Nature, 2008. **453**(7194): p. 499-U4.
23. Vondermassen, K., J. Bongers, A. Mueller, and H. Versmold, *Brownian-Motion - a Tool to Determine the Pair Potential between Colloid Particles.* Langmuir, 1994. **10**(5): p. 1351-1353.
24. Royall, C.P., D.G.A.L. Aarts, and H. Tanaka, *Fluid structure in colloid-polymer mixtures: the competition between electrostatics and depletion.* Journal of Physics-Condensed Matter, 2005. **17**(45): p. S3401-S3408.
25. Royall, C.P., R. van Roij, and A. van Blaaderen, *Extended sedimentation profiles in charged colloids: the gravitational length, entropy, and electrostatics.* Journal of Physics-Condensed Matter, 2005. **17**(15): p. 2315-2326.
26. Pawley, J.B., *Handbook of biological confocal microscopy*. 2nd ed. 1995, New York: Plenum Press. xxiii, 632 p.
27. Kogan, M., C.J. Dibble, R.E. Rogers, and M.J. Solomon, *Viscous solvent colloidal system for direct visualization of suspension structure, dynamics and rheology.* Journal of Colloid and Interface Science, 2008. **318**(2): p. 252-263.
28. Martinez, C.J., J.W. Liu, S.K. Rhodes, E. Luijten, E.R. Weeks, and J.A. Lewis, *Interparticle interactions and direct imaging of colloidal phases assembled from microsphere-nanoparticle mixtures.* Langmuir, 2005. **21**(22): p. 9978-9989.
29. Solomon, T. and M.J. Solomon, *Stacking fault structure in shear-induced colloidal crystallization.* Journal of Chemical Physics, 2006. **124**(13): p. -.
30. Hansen-Goos, H., C. Lutz, C. Bechinger, and R. Roth, *From pair correlations to pair interactions: An exact relation in one-dimensional systems.* Europhysics Letters, 2006. **74**(1): p. 8-14.
31. Ramirez-Saito, A., C. Bechinger, and J.L. Arauz-Lara, *Optical microscopy measurement of pair correlation functions.* Physical Review E, 2006. **74**(3): p. -.
32. Ramirez-Saito, A., M. Chavez-Paez, J. Santana-Solano, and J.L. Arauz-Lara, *Effective pair potential between confined charged colloidal particles.* Physical Review E, 2003. **67**(5): p. -.
33. Guzman, O. and J.J. de Pablo, *An effective-colloid pair potential for Lennard-Jones colloid-polymer mixtures.* Journal of Chemical Physics, 2003. **118**(5): p. 2392-2397.
34. Antl, L., J.W. Goodwin, R.D. Hill, R.H. Ottewill, S.M. Owens, S. Papworth, and J.A. Waters, *The Preparation of Poly(Methyl Methacrylate) Lattices in Nonaqueous Media.* Colloids and Surfaces, 1986. **17**(1): p. 67-78.
35. Campbell, A.I. and P. Bartlett, *Fluorescent hard-sphere polymer colloids for confocal microscopy.* Journal of Colloid and Interface Science, 2002. **256**(2): p. 325-330.

36. Pathmamanoharan, C., K. Groot, and J.K.G. Dhont, *Preparation and characterization of crosslinked PMMA latex particles stabilized by grafted copolymer.* Colloid and Polymer Science, 1997. **275**(9): p. 897-901.
37. Royall, C.P., M.E. Leunissen, and A. van Blaaderen, *A new colloidal model system to study long-range interactions quantitatively in real space.* Journal of Physics-Condensed Matter, 2003. **15**(48): p. S3581-S3596.
38. Fuoss, R.M., *Dependence of the Walden Product on Dielectric Constant.* Proceedings of the National Academy of Sciences of the United States of America, 1959. **45**(6): p. 807-813.
39. Bautista, F., L. Rejon, and O. Manero, *The dielectric spectrum and the electrorheological effect in suspensions of varying conductivity - Part 2. Modeling of the electrorheological effect.* Colloids and Surfaces a-Physicochemical and Engineering Aspects, 2007. **303**(3): p. 191-200.
40. Obrien, R.W. and L.R. White, *Electrophoretic Mobility of a Spherical Colloidal Particle.* Journal of the Chemical Society-Faraday Transactions Ii, 1978. **74**: p. 1607-1626.
41. Russel, W.B., D.A. Saville, and W.R. Schowalter, *Colloidal dispersions*. 1989, Cambridge ; New York: Cambridge University Press. xvii, 525 p.
42. Crocker, J.C. and D.G. Grier, *Methods of digital video microscopy for colloidal studies.* Journal of Colloid and Interface Science, 1996. **179**(1): p. 298-310.
43. Dibble, C.J., M. Kogan, and M.J. Solomon, *Structure and dynamics of colloidal depletion gels: Coincidence of transitions and heterogeneity.* Physical Review E, 2006. **74**(4): p. -.
44. Iacovella, C.R.; Rogers, R. E.; Glotzer, S. C.; Solomon, M. J., *Pair Interaction Potentials by Extrapolation of Confocal Microscopy Measurements of Collective Structures.* In Preparation, 2010.

CHAPTER 3

ROLE OF SEDIMENTATION IN THE COLLOIDAL CRYSTALLIZATION OF OPPOSITELY-CHARGED PARTICLES

Chapter Summary

We investigate the role of sedimentation in the formation of ionic colloidal crystals. Using poly-12-hydroxystearic acid-stabilized poly(methyl methacrylate) (PHSA-PMMA) and poly(diphenyl dimethyl siloxane)-stabilized poly(methyl methacrylate) (DPDMS-PMMA) particles, we successfully assemble colloidal crystals of the cesium chloride (CsCl) type. A range of conditions leading to crystallization is seen for medium to high initial volume fractions ($0.12 < \phi_i < 0.24$) at various density differences between the particle and solvent. We find that the onset of crystallization is controlled by the Peclet number (Pe = ratio of convective forces to diffusive forces) and the initial volume fraction. Particle surface charge is examined via zeta potential measurements. We find that the PHSA-PMMA particles carry a negative surface charge while the DPDMS-PMMA particles carry a positive surface charge. This is observed at all conditions studied in this work. We find that the trend in ionic colloidal crystallization is opposite to that observed by Davis et al. [1] where $Pe^*\phi_i \leq 10^{-3}$ for hard-sphere crystallization. We believe this observed trend occurs because of a different mechanism for ionic colloidal crystallization versus hard-sphere crystallization.

3.1. Introduction

Colloidal particles are of continued interest because they are ubiquitous in nature and provide excellent models for studying equilibrium phase behavior [2]. Suspensions of colloidal particles have widely been used to study processes related to freezing, melting, and glass transition [3-7]. Colloidal systems may undergo crystallization because of the effects of packing and excluded volume [8], charge [9], or weak attractions [10]. Colloidal interactions come in a wide variety, including long-range repulsive [3, 6, 7], short-range attractive [5], hard-sphere like [4, 6, 7], and dipolar [7]. All of these interactions have been realized and equilibrium phases have been shown to occur as a consequence of them.

Sedimentation is a self-assembly technique that utilizes the field of gravity to control the rate at which colloidal particles move from a dilute suspension to a concentrated sediment [11]. This technique has been extensively studied and has been accepted as a means for forming high quality colloidal crystals. Sedimentation studies have addressed hard-sphere crystallization [1, 12-14], one-component crystallization of charged spheres [15, 16], two-component ionic crystallization [17, 18], stacking faults and defects [19, 20], and equilibrium sedimentation at interfaces [21, 22]. Russel pioneered the quantitative theory of colloidal sedimentation as a competition between sedimentation and crystallization rates. Providing critical analyses on this phenomenon [1], Russel has shown that sedimentation is simple to initiate and easy to control on the macroscopic scale. One is able to qualitatively and quantitatively utilize these advantages to generate colloidal crystals that are long range and defect-free. Given the advantages of

sedimentation, the drawback to this technique is time. Compared to other crystallization techniques (e.g. spin coating [15] and shear [20]), sedimentation requires on the order of days to weeks to form crystals of the same type, quality, and magnitude. While this drawback makes sedimentation unfavorable for practical applications, it is still valuable for fundamental studies on ionic colloidal crystallization because it is one of the few techniques that yield high quality crystals.

Hard-sphere colloidal crystallization is an important base case to which the behavior of other systems me be compared [1, 6, 12-14, 23, 24]. For equilibrium conditions, crystallization in hard-sphere systems is observed at a volume fraction of $\phi = 0.494$. For $0.494 < \phi < 0.545$, coexistence is observed. For $\phi > 0.545$, full crystallinity is observed. Above a volume fraction of 0.58, the system will transition into a glass phase [6]. These volume fractions provide useful benchmarks when studying systems that are not hard sphere in nature. For hard sphere systems, the maximum packing fraction is found to be 0.74. This translates into the face-centered cubic (fcc) structure, which is the most stable thermodynamically [6]. Hexagonal close pack (hcp) is also favored in this type of system. In practice, crystals with close packed layers with different abundances of fcc and hcp are typically found.

The behavior of charged colloidal particles depends heavily on the charge interactions. For one-component systems, the interactions will be repulsive. Studies have shown that in order to successfully crystallize these particles, screening of the charge must take place [15, 16, 25]. Accomplished by addition of electrolyte, screening helps to reduce the

Debye length on the particle. The Debye length is the electric double layer around the bare particle that contributes to the repulsive potential between two particles. In effect, this layer extends the effective radius of the particle, thereby affecting the volume fraction of thermodynamic transitions such as the crystallization boundary. Studies have shown that successful screening of the charge in such colloidal systems yield high quality, long-range crystalline structures. In repulsive colloidal systems, hexagonal close pack, face-centered cubic, and body-centered cubic (bcc) [9] are typically observed.

For two-component systems, the interactions between the particles are typically ionic. Interesting possibilities occur when some percentage of the particles are of opposite charge because attractions result. If the attractions are too significant heterocoagulation occurs. However, for $U_{att}/k_BT \sim -1$, interesting phases may result. It has long been observed that long-range attractive interactions lead to irreversible aggregation in colloidal systems [26]. Until recently, the long-range attractive interaction has yet to be fully realized in colloidal suspensions [17, 18]. Ionic colloidal crystallization is a technique that takes advantage of attractive interactions to cause particles of opposite charge to crystallize. By carefully tuning these attractive interactions (not neutralizing them), one can produced unique long-range ordered structures. Depending on the size ratio between the opposing particles, various structures can be realized. For size ratios close to 1, cubic (fcc and bcc) structures typically form. More intriguing structures form at ratios well below 1, including LS_6 and LS_8 structures. Ionic colloidal crystallization has been shown to provide promise in the field of photonics and the associated applications [17, 27-36]. A method for achieving self-assembled binary colloidal crystals

of opposite charge was presented by Leunissen et al [17]. Using sedimentation techniques, long-range ordered crystals were achieved. Crystals were observed at size ratios of 0.31 and 1. One of the requirements for these ionic crystals was the need for a modest attraction ($U(r) \sim -2k_BT$) between the two particles. In particular, the attractions were needed such that irreversible aggregation was restricted. Achieving such a modest attraction on a consistent basis was difficult due to batch-to-batch variations in the surface charge of particles.

Although a thermodynamic analysis of colloidal crystallization via sedimentation has been done for hard-sphere, repulsive, and ionic systems, a thorough kinetics analysis has been limited to hard sphere systems. In a study done by Davis et al. [1, 12], an examination of the limits to crystallization of such systems was quantified. Davis showed that sedimentation of hard spheres was controlled by the Peclet number (Pe) and the initial volume fraction. For the particular case studied, they found that crystallization is observed when $Pe * \phi_i < \sim 10^{-3}$. The Peclet number is a dimensionless quantity that is a ratio of the convective forces to the diffusive forces:

$$Pe = \frac{(\Delta\rho)ga^4}{k_BT} \qquad (3\text{-}1)$$

where $\Delta\rho$ is the density difference between the particle and solvent, g is the acceleration due to gravity, a is the particle radius, k_B is the Boltzmann constant, and T is the absolute temperature [37]. When the Peclet number is less than one, diffusive forces dominate. Convective forces, in this case due to gravity, dominate when the Peclet number is greater than one. Davis concluded that hard sphere crystallization would take place for low Peclet number and low initial volume fraction. In other words, limiting the density

mismatch between the particles and solvent increases the probability of achieving crystallization. In sedimentation studies, the convective forces are controlled by the magnitude of the density mismatch and gravity. Therefore, it is of interest to understand what limitations, if any, exists in varying the Peclet number and achieving crystallization for ionic colloidal systems.

Visualization of colloidal crystal structures is also of continued interest. Light microscopy techniques provide a simple means to visualize a specimen. It is limited, however, because it does not provide a means for viewing the three-dimensional structure. Light microscopy does not block out of focus light, which inhibits the ability to view a particular plane within the sample because of the large background contribution from out of focus light. Confocal laser scanning microscopy (CLSM), on the other hand, provides the means for acquiring the three-dimensional structure of crystals [38]. The major feature of the CLSM is the pinhole, which acts to block light that did not originate in the object plane. By prohibiting this light from passing through, the CLSM is able to focus on a point within the sample and not just on the surface. A collection of many image slices over a set distance leads to a three-dimensional volume. This method allows the study of not only structure but also dynamics and other valuable parameters.

One of the challenges with ionic colloidal crystallization is ensuring the charge on the particles of interest are opposite in nature. If one could synthesize a particle that consistently maintained a positive or negative charge, then crystallization could be readily done without relying on the tenuous nature of batch-to-batch variability in the

particle surface charge. We will show through the use of CLSM that binary crystallization of oppositely-charged particles is possible by mixing two model colloids- one negatively charged and one positively charged. One of the particles has the unique property of retaining its original sign upon addition of salt while the other particle can undergo a reversal of its sign by the introduction of the same salt. By synthesizing a colloidal particle with a stabilizing layer that resists the effects of a sign-reversing agent, we are able to rapidly produced binary crystals. Thus, batch-to-batch variability does not restrict our ability at maintaining the same sign on our particle. Each batch of particles synthesized provides a different pairing with particles of opposite charge such that the restriction on modest attraction is maintained. With our model system, the ability to mix and match particles enhances the possibility of achieving ionic colloidal crystals.

Previous work done on ionic colloidal crystallization via sedimentation provides valuable insight for isolating the various crystal structures useful in applications of great interest [17]. While this work has been thorough in providing a thermodynamic analysis of this type of crystallization, questions remain related to the kinetics of ionic colloidal crystallization. Specifically, the questions of how ionic crystallization proceeds and the range of crystallization achievable have not been fully answered. Therefore, the objectives of this study are to:

- Determine the conditions needed to successfully reproduce the ionic colloidal crystals following the method as outlined by Leunissen et al. [17]

- Quantify the range (i.e. initial volume fraction, ϕ_i, and the Peclet number, Pe) of ionic colloidal crystallization possible using the technique of sedimentation. Our approach will be to vary the density difference between the particles and solvent.
- Understand the nucleation and growth of these ionic colloidal crystals in order to provide a qualitative assessment of how this type of crystallization takes place.
- Compare ionic crystallization results to literature studies of hard-sphere crystallization.

3.2. Experimental

3.2.1. Particle Synthesis

Fluorescently-labeled poly(methyl methacrylate) particles stabilized by poly-12-hydroxystearic acid (PHSA-PMMA) were synthesized as outlined in Chapter 2. Fluorescently-labeled poly(methyl methacrylate) particles stabilized by poly(diphenyl-dimethyl siloxane) (DPDMS-PMMA) particles were synthesized using the method of Kogan et al [39]. In a two-step dispersion polymerization process, the DPDMS stabilizer was synthesized first. The stabilizer step entailed dissolving DPDMS in hexane solvent and initiating a polymerization reaction with benzoyl peroxide (BPO) to form the stabilizer liquid. Next, the stabilizer is combined with methyl methacrylate (MMA) and used to form a stabilizing layer around the PMMA particles as a second polymerization reaction is initiated with BPO. Each reaction step took 12 hours to complete. Particles were dyed with Coumarin-30 Yellow (Sigma-Aldrich, USA). To ensure a monodisperse system, particle synthesis proceeded such that the polydispersity was no more than 5%. Particles were sized using scanning electron microscopy (SEM). Figure 3.1 shows

representative images of both PHSA-PMMA and DPDMS-PMMA particles. Average particle sizes were 660 nm (polydispersity = 4%) for PHSA-PMMA and from 609 nm (polydispersity = 3%) for DPDMS-PMMA.

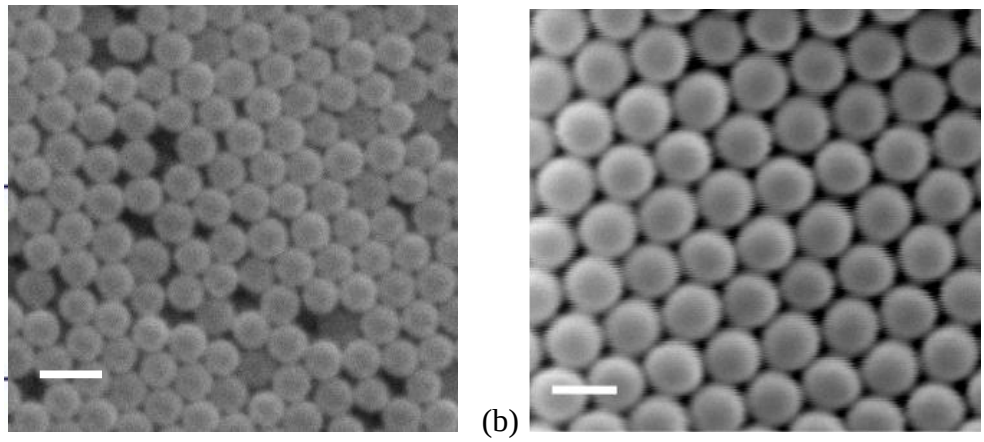

Figure 3.1 – Scanning electron microscopy images of poly(methyl methacrylate) particles stabilized by (a) poly-12-hydroxystearic acid and (b) poly(diphenyl dimethyl siloxane). Scale bars represent 2μm.

3.2.2. Sample Preparation and Imaging

Ionic colloidal crystallization of the PHSA-PMMA and DPDMS-PMMA particles was performed following the procedure discussed by Leunissen et al [17]. Particles were prepared in separate salt solutions of cyclohexyl bromide (CHB) (Sigma-Aldrich, United States) and decalin (Fluka, United States) with a mass ratio ranging from 30% CHB/70% decalin to 80% CHB/20% decalin. Variation of the mass ratio was done to assess the range of crystallization that could be achieved by varying the magnitude of the gravitational driving force for sedimentation because of the density difference between solvent and particle. See section 3.3.5 for further discussion. Tetrabutyl ammonium chloride (TBAC) was chosen to serve as the electrolyte for this work. Concentrations ranged from 100μM to 6mM. Although quantification of the Debye length

corresponding to these salt concentrations is challenging for reasons discussed in the previous chapter, we roughly estimate that 100μM concentrations of salt yield Debye lengths of approximately 110 nm and 6mM salt concentrations yield Debye lengths of approximately 79 nm. In this chapter, most measurements were performed with particles in 6mM salt concentration. The particles were allowed to equilibrate in the salt solution for at least three hours. It was found that the particle surface charge varied before three hours. After three hours, the surface charge reached a plateau. Particle solutions were then mixed using a vortex mixer until completely dispersed and transferred to a capillary cell (2mm I.D., 6mm O.D., 20mm height). The combined solution was allowed to sediment over the course of 96 hours with initial observations being taken within 24 hours of sedimentation.

Confocal laser scanning microscopy was used to image the samples. A Leica SP2 TCS confocal laser scanning microscope (Leica, Germany) was used. Figure 3.2 provides a pictorial view of the confocal microscope setup. To view the particles with different colors, excitation wavelengths were set to 458nm (Coumarin-30) and 543nm (Nile Red). Emission bands were set to be 470nm-530nm (Coumarin-30) and 560nm-660nm (Nile Red).

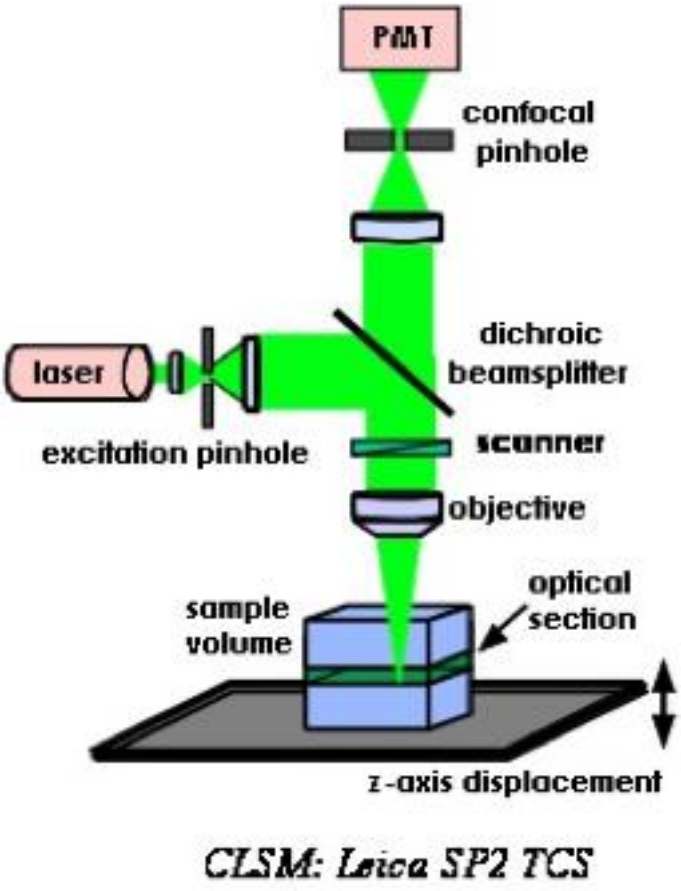

Figure 3.2 – Leica SP2 TCS confocal laser scanning microscope [40]

3.2.3. Charge Characterization

To determine the charge on the synthesized particles, zeta potential measurements were done. Mobility of the particles was obtained using a Zetasizer Nano Series ZS device (Malvern, United Kingdom). PHSA-PMMA and DPDMS-PMMA particles were each dispersed in the previous determined range of CHB/decalin solvents containing TBAC at 6mM concentration. For each condition, five measurements of 50 sub-runs were performed. Inputs to the device included the particle type, solvent viscosity, and applied voltage (default setting was 40mV). The average mobility was computed and used for subsequent calculations. The zeta potential was calculated using a computer program

based on the method of O'Brien and White [41]. Inputs to this program included the dimensionless Debye length, equivalent conductance (in units of $m^2 \cdot S/mol$) for TBAC (19.4 for TBA^+ and 73.6 for Cl^-) [42], solvent dielectric constant (5.59 for CHB/decalin [25]), and solvent viscosity (2 Pa·s). The zeta potential was outputted from the program based on the solution to the Poisson equation. Conductivity measurements were done for the CHB/decalin solvent containing 6mM. From the conductivity measurements, the Debye length was computed (~79 nm for [TBAC] = 6mM) and used in the computer program. The charge on the particle was calculated using the relation

$$Q = 4\pi\varepsilon_0\varepsilon_r a\zeta(1+\kappa a) \qquad (3\text{-}2)$$

where Q is the particle charge, ε_r is the relative dielectric constant of the CHB/decalin solvent (5.59), ε_0 is the permittivity of free space, ζ is the zeta potential, κ is the inverse Debye screening length, and a is the particle radius [25]. The charge number, Z, was then determined by dividing the calculated charge by the charge of an electron.

Several experimental and systematic errors introduced throughout the computation process raised questions about the accuracy of the device used to measure the charge mobility. To this end, zeta potential test standards, obtained directly from the maker of the Zetasizer (Malver, United Kingdom), were used to calibrate the device. Four independent runs of the test standard were performed. The testing standard had a known value of -68 mV with a standard deviation of 2.1 mV. Measured zeta potential values of the test standard were, on average, -63.4 mV with a standard deviation of 6.4 mV. Based

on the test standard results, it was determined that the device was working within specification as outlined by Malvern.

The accuracy of the surface charge measurements also depended on the particle surface charge reaching an equilibrium steady state. In earlier experiments, a variation in the charge mobility was seen across samples containing lower concentrations of TBAC. This variation led to an inaccurate profiling of the zeta potential and surface charge. To understand the sensitivity of the surface charge to TBAC, a time analysis was performed to determine when the equilibrium point was reached. PHSA-PMMA particles with a particle diameter of 929nm (polydispersity = 4.3%) were prepared in CHB/decalin solutions containing 1.5μM TBAC. We observed the greatest variation in the mobility at this concentration. Samples were monitored for 48 hours with measurements taken at 0, 3, 24, and 48 hours. Figure 3.3 shows how the zeta potential varied over the course of this study.

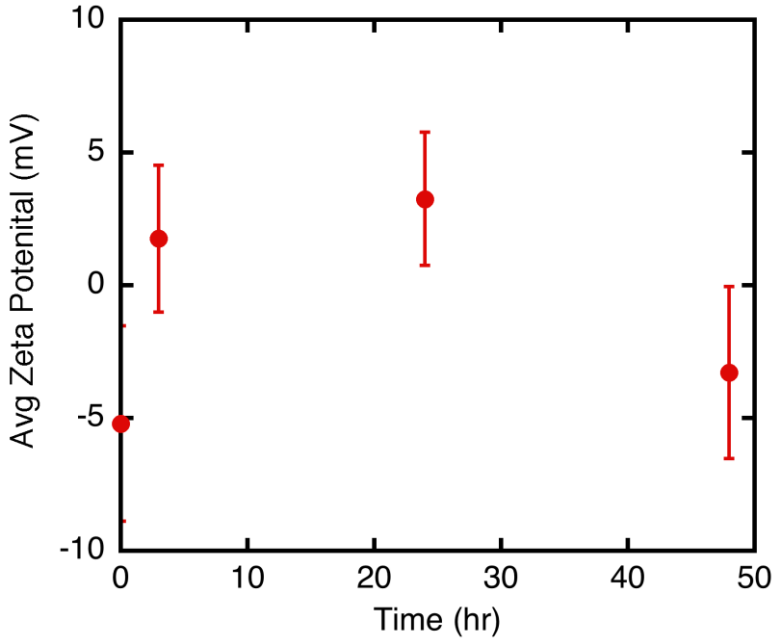

Figure 3.3 – Zeta potential of 929nm PHSA-PMMA particles in CHB/decalin (73%/27% by mass) containing 1.5μM TBAC. Data points taken at 0 hrs, 3 hrs, 24 hrs, and 48 hrs. Error bars represent the standard error of the mean for each data point.

Between 0 and 3 hours, a large change in the charge mobility, and zeta potential, was observed. Between 3 and 24 hours, the change in the zeta potential was significantly less. While a decrease in the zeta potential was seen at 48 hours, it was not statistically different from the zeta potential initially or at 3 hours. Therefore, it was concluded that the particles should be dispersed into the solvent and allowed to equilibrate for at least 3 hours before proceeding with crystallization experiments. We expected the variation at higher TBAC concentration to be less than that seen at the lower concentration so the 3-hour time limit would be sufficient for the surface charge of our samples to reach equilibrium.

Appendix A presents a detailed analysis on the measurement of the zeta potential and analysis of the results. Details on determining the accuracy of the output from the zetasizer is presented.

3.2.4. Calculation of Peclet Number

The Peclet number, corresponding to the different sedimentation scenarios was computed from direct measurements of the sedimentation front. Samples containing the combined PHSA-PMMA and DPDMS-PMMA particles were prepared in CHB/decalin solvent at ratios ranging from 30/70 to 80/20 CHB/decalin (mass %). This range was chosen to give us the broadest spectrum, in terms of density differences, to allow us to make accurate assessments of the behavior of any crystallization seen. Initial volume fraction for all samples was 0.12. This volume fraction was chosen for prior studies in the literature. A constant total height of the solution was set to 15mm (± 1mm). Samples were set on top of a bench top counter and allowed to sediment for one hour. After one hour elapsed, the sedimentation velocity was computed by measuring the distance between the meniscus and top of the sediment. The Peclet number was then computed using equations 3-3 and 3-1.

$$U_0 = \frac{2a^2(\Delta\rho)g}{9\mu} \tag{3-3}$$

$$Pe = \frac{(\Delta\rho)ga^4}{k_B T} \tag{3-1}$$

U_0 is the sedimentation velocity, a is the particle radius, $\Delta\rho$ is the density difference between the particle and solvent, g is the acceleration due to gravity, μ is the solvent viscosity, Pe is the Peclet number, k_B is the Boltzmann constant, and T is the absolute temperature [37]. Figure 3.4 shows a time lapse series of a sample in a CHB/decalin ratio of 50/50 by mass.

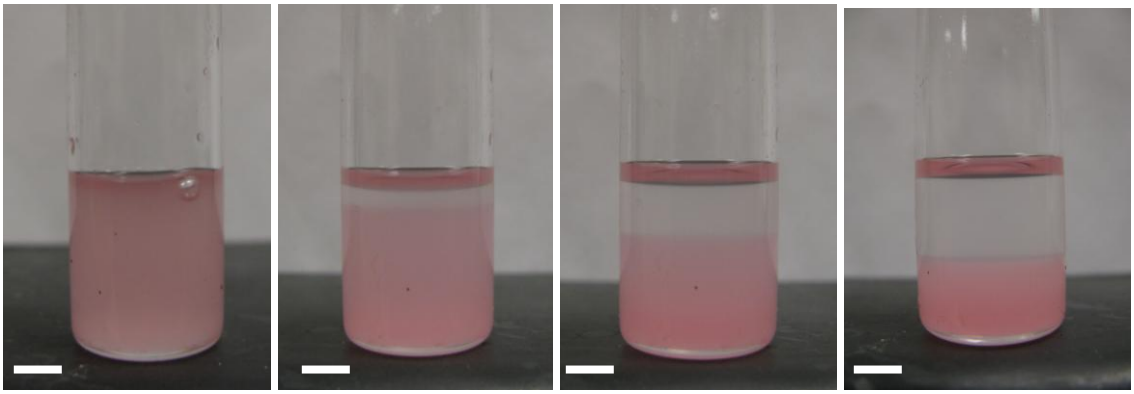

(a) (b) (c) (d)

Figure 3.4 – Sedimentation of PHSA-PMMA and DPDMS-PMMA particles in 50/50 (mass %) CHB/decalin containing 6mM TBAC. Total height of solution is 15mm. Images taken at (a) t = 0 mins, (b) t = 20 mins, (c) t = 40 mins, and (d) t = 60 mins. Scale bars on all images = 4mm.

3.3. Results

3.3.1. Colloid Charge Characterization

Figure 3.5 shows the charge number as a function of CHB mass fraction. The concentration of TBAC in all cases was 6mM. Charge measurements at CHB/decalin ratios of 40/60, 50/50, 60/40, and 70/30 were done to determine if variation of the CHB/decalin, and the density difference between the particles and solvent, produced a significant difference in the surface charge. Five independent measurements, for both

PHSA-PMMA and DPDMS-PMMA particles at each CHB/decalin ratio, were performed for charge mobility using the zetasizer. The zeta potential and charge number were computed for each mobility value and averaged. The solid lines in the figure indicate the average charge number across all CHB/decalin ratios. For PHSA-PMMA particles, the average charge number was determined to be -88 ± 17. For DPDMS-PMMA particles, the average charge number was determined to be +59 ± 14. Error in the average charge number calculation is the standard deviation of the mean. Shown in Figure 3.5 are the upper and lower limits based on the standard deviation. Since the majority of the charge numbers statistically reside within the standard deviation, we conclude that variation of the CHB/decalin will not have a major impact on our ability to characterize the crystallization that is observed.

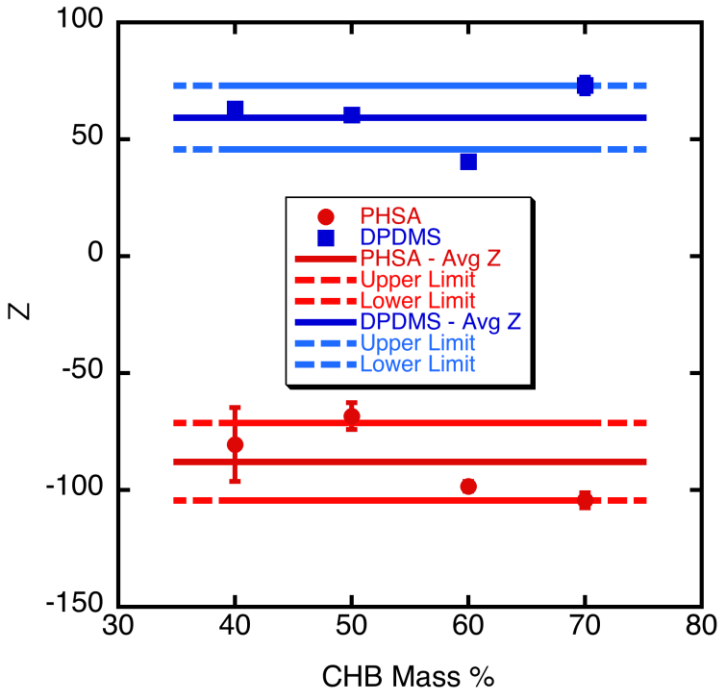

Figure 3.5 – Charge number as a function of CHB/decalin for both PHSA-PMMA and DPDMS-PMMA particles. TBAC concentration for all samples was 6mM. Solid lines represent mean charge number. Error represented by upper and lower limits (dashed lines) based on standard deviation of the mean charge number. (κ^{-1} = 79nm)

Previous to this work, a study of the zeta potential as a function of the TBAC salt concentration was done to understand behavior of each particle system when exposed to increasing salt concentration. Figure 3.6 presents the zeta potential as a function of the salt concentration. Salt concentrations ranged from 0μM to 120μM. When dispersed in pure CHB/decalin (no TBAC), it was found that both PHSA-PMMA and DPDMS-PMMA carried a positive surface charge. As the salt concentration increased, the PHSA-PMMA particle surface charge went from positive to negative. This observation has been reported elsewhere in the literature [25]. Eventually, the zeta potential reached a constant and no further changes were observed. For the DPDMS-PMMA particles, the surface

charge remained positive regardless of the amount of salt that was introduced in the CHB/decalin solvent. It is believed that the underlying chemistry of each system leads to these interesting findings.

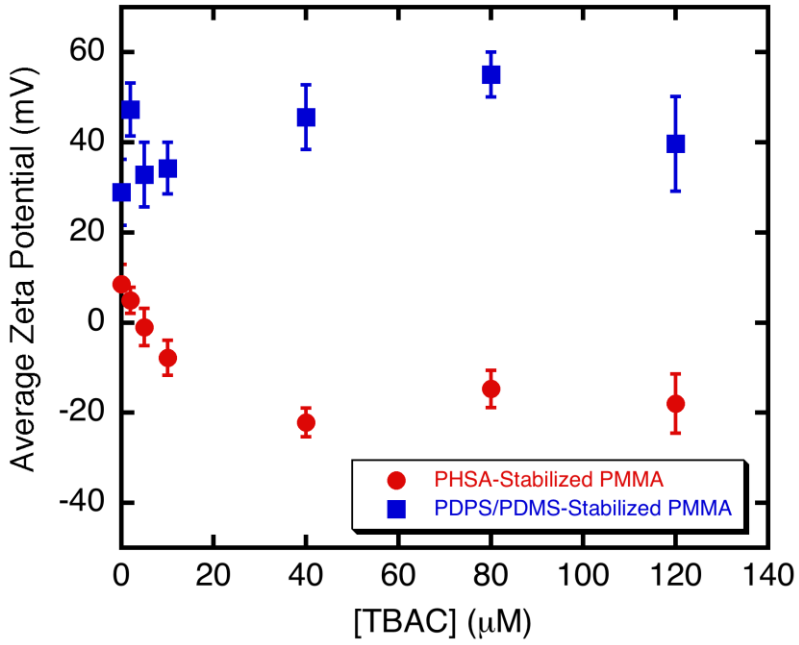

Figure 3.6 – Zeta potential as a function of TBAC concentration ranging from 0μM to 120μM. PHSA-PMMA particles (diameter = 660 nm) and DPDMS-PMMA particles (represented as PDPS/PDMS-stabilized PMMA, diameter = 634 nm) were observed to carry positive surface charge initially. Sign of PHSA-PMMA surface charge changed to negative as TBAC concentration increased. Error bars represent standard error of the mean.

3.3.2. Reproducibility of Ionic Colloidal Crystals

The formation of ionic colloidal crystals proceeded by the method of Leunissen et al. [17]. Leunissen demonstrated that ionic colloidal crystals could be formed by combining oppositely-charged PMMA particles in a solvent mixture of 73%/27% (vol.) CHB/decalin. Salt concentration was kept at 60μM tetrabutylammonium bromide

(TBAB). The size ratio (a_1/a_2) of their particles was 0.92. Initial volume fraction of the samples was set to 0.12. Samples were placed in a cell and allowed to sediment with the first signs of crystallites being observed within 24 hours.

Proceeding in a similar manner, PHSA-PMMA and DPDMS-PMMA particles were prepared and solutions allowed to sediment. To determine the conditions needed to reproduce a similar binary crystal, a screening test was implemented looking at various salt concentrations at an initial volume fraction of 0.12. The CHB/decalin ratio was initially set to 73%/27% (mass) but allowed to vary between 69%/31% and 77%/23%. In this case, a slightly larger DPDMS-PMMA particle (σ = 634 nm) was combined with the PHSA-PMMA particles (σ = 660 nm). The size ratio for this particle pairing was 0.96. TBAC concentrations ranged from 1μM to 10mM. At micromolar concentrations of salt no crystallization was observed. Between 1mM and 4mM TBAC, the particles began showing slight ordering. Between 5mM and 6mM, more ordering was observed. At 6mM, full ordering was noted. Figure 3.7 shows a CLSM image of one of the first ionic colloidal crystals to be reproduced. Above 6mM, the degree of ordering decreased significantly indicating a peak in crystallization was found at the 6mM concentration mark. Confirmation of reproducibility was satisfied with the formation of four additional crystals under these same conditions. Ionic colloidal crystals were also able to be reproduced using the 609 nm DPDMS-PMMA particles.

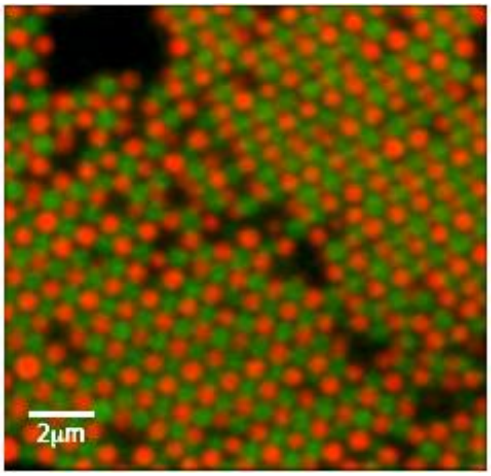

Figure 3.7 – 660 nm PHSA-PMMA and 634 nm DPDMS-PMMA ionic colloidal crystals. Initial volume fraction = 0.12. Final volume fraction = 0.56. Particles dispersed in 71% CHB/29 % decalin (by mass) with 6mM TBAC.

3.3.3. Quality of Ionic Colloidal Crystallization

It was observed that the quality of ionic colloidal crystallization depended strongly on how the particles settled within the solvent. Figure 3.8 provides insight into how the particles order and form ionic crystals. At a far enough distance, image dimension = 37.5 μm x 37.5 μm, distinct regions of ordering were observed within the samples. Scanning in all three dimensions, crystalline ordering was found to extend laterally (x-y directions) up to approximately 100 μm and vertically (z-direction) up to 50 μm. We define a sample to be crystalline if binary ordering was observed at least 20μm in the x-y direction and at least 10μm in the z-direction. Of the samples that we labeled "crystalline", approximately 90% of them satisfied this definition. In all samples, pockets of aggregation were observed. These aggregates were either one-component (phase separated) or two-component. When comparing these results to previous studies [17, 18], it was found that crystallization was incomplete and prone to defects. These defects included holes and grain boundaries. Though the samples in this work produced

polycrystalline results, the overall objective of this study was not compromised. Therefore, it was concluded that the incomplete crystallization should be studied in further detail but the analysis of the formation of these ionic crystals should not be dependent on forming pure crystals.

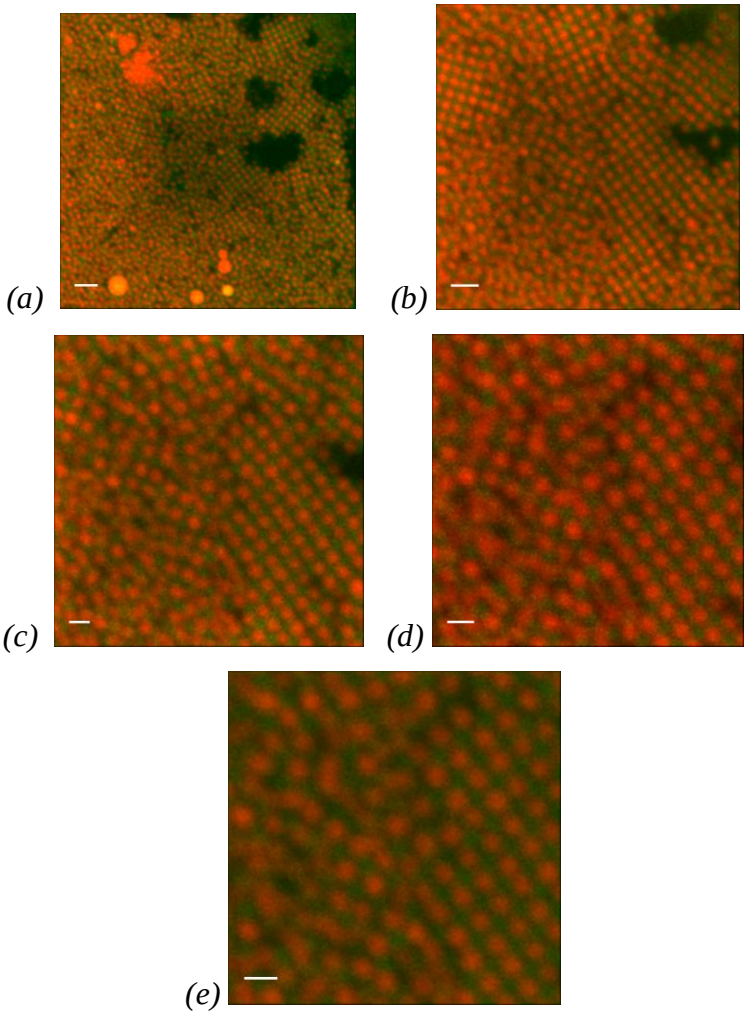

Figure 3.8 – Quality of ionic crystallization for PHSA-PMMA and DPDMS-PMMA particles. Particles are dispersed in 50/50 mixture of CHB/decalin containing 6mM TBAC. Initial volume fraction was 0.18. Images were taken 10μm above the cover glass. Image dimensions: (a) 37.5μm x 37.5μm; (b) 21.4μm x 21.4μm; (c) 15μm x 15μm; (d) 11.5μm x 11.5μm; (e) 10μm x 10μm. Scale bars on images: (a) and (b) = 10μm; (c) = 5μm; (d) and (e) = 2μm

3.3.4. Identification of Crystal Structure

To identify the particular structure of our crystals, image processing techniques were utilized to produce 3-D renderings of our structures. We used image processing code, based on the algorithms of Crocker and Grier [43], to perform image processing on our image volumes. As previously discussed in Chapter 2, image stacks were filtered using a Gaussian filter to remove noise from the images. Next, particle centroids were indentified using a brightness maximum routine. This routine was performed in all three spatial directions. Finally, particle locations are generated and stored. The accuracy of the image processing code was confirmed using overlay images which assess how well the code located and identified particle centers. Volume fractions of the sediment were computed using the total number of particles identified by the code. As this was a binary system, image processing was performed on each individual color (red vs. green) and combined at the end.

Figure 3.9 shows a rendering of the ionic colloidal crystals. In order to properly identify the structure of our crystals, reference crystals were generated using a Visual Molecular Dynamics (VMD) software package (http://www.ks.uiuc.edu/Research/vmd/). Leunissen et al. [17] showed that oppositely-charged particles with a size ratio close to unity typically produced cubic structures. With this knowledge, face-centered cubic (fcc) and body-centered cubic (bcc) structures were generated. Figure 3.9(a) is a rendering of a pure cesium chloride (bcc) structure while Figure 3.9(b) is a rendering of a pure sodium chloride (fcc) structure. Key features in each of these renderings helped to isolate the difference in the structure. For the cesium chloride structure, each alternating layer is

offset from the previous layer. Also, there is larger spacing between the particles. For the sodium chloride structure, particles alternate in each layer and each layer is not offset from the previous layer. Figure 3.9(c) shows RASMOL renderings of the experimental crystal. Initial assessment showed that our crystals were of the cesium chloride type. Rotating the RASMOL rendering by 30 degrees confirmed this initial assessment when compared to the pure cesium chloride structure.

In addition to the qualitative assessment of our crystal structures, comparison work with published phase diagrams for ionic colloidal systems was done. By calculating the charge ratio (Q) and dimensionless Debye length (κa), the phase diagram shown in Figure 3.10 was used to pinpoint the crystal structure. The phase diagram, based on the work of Leunissen et al. [17], shows the three primary phases that are observed for a size ratio of 1. In an ideal system ($T^* = 0$, where T^* is the dimensionless temperature), where there is no entropy, the phase boundaries are given by the black lines. These represent Madelung energy (zero-temperature) calculations. As entropy is introduced, the phase boundaries shift depending on the amount of entropy in the system when the particles are in contact. Using Monte Carlo simulations, Leunissen et al. computed the various contact energies to assess the importance of entropy at ambient temperatures. Their results are represented by the various colored lines, representative of the different contact energies, on their phase diagram. We computed an average charge ratio of 1.48 and a dimensionless Debye length of 4.17. The experimental pair potential (at contact) of our system was computed to be approximately $-2\ k_BT$ using the screened Yukawa equation:

$$\frac{U(r)}{k_B T} = Z_i Z_j \lambda_B \frac{e^{\kappa(a_i + a_j)}}{(1+\kappa a_i)(1+\kappa a_j)} \frac{e^{-\kappa r}}{r}, \qquad (3\text{-}5)$$

where *U(r)* is the pair potential at contact, k_B is the Boltzmann constant, *T* is the absolute temperature, *Z* is the charge number, λ_B is the Bjerrum length (10nm), κ is the inverse of the Debye length, *a* is the particle radius, *r* is the center-to-center separation (equals 1 at contact). Based on these values, we found we were within the cesium chloride region of the phase diagram. The single blue circle pinpoints the exact location of our system on the Leunissen phase diagram.

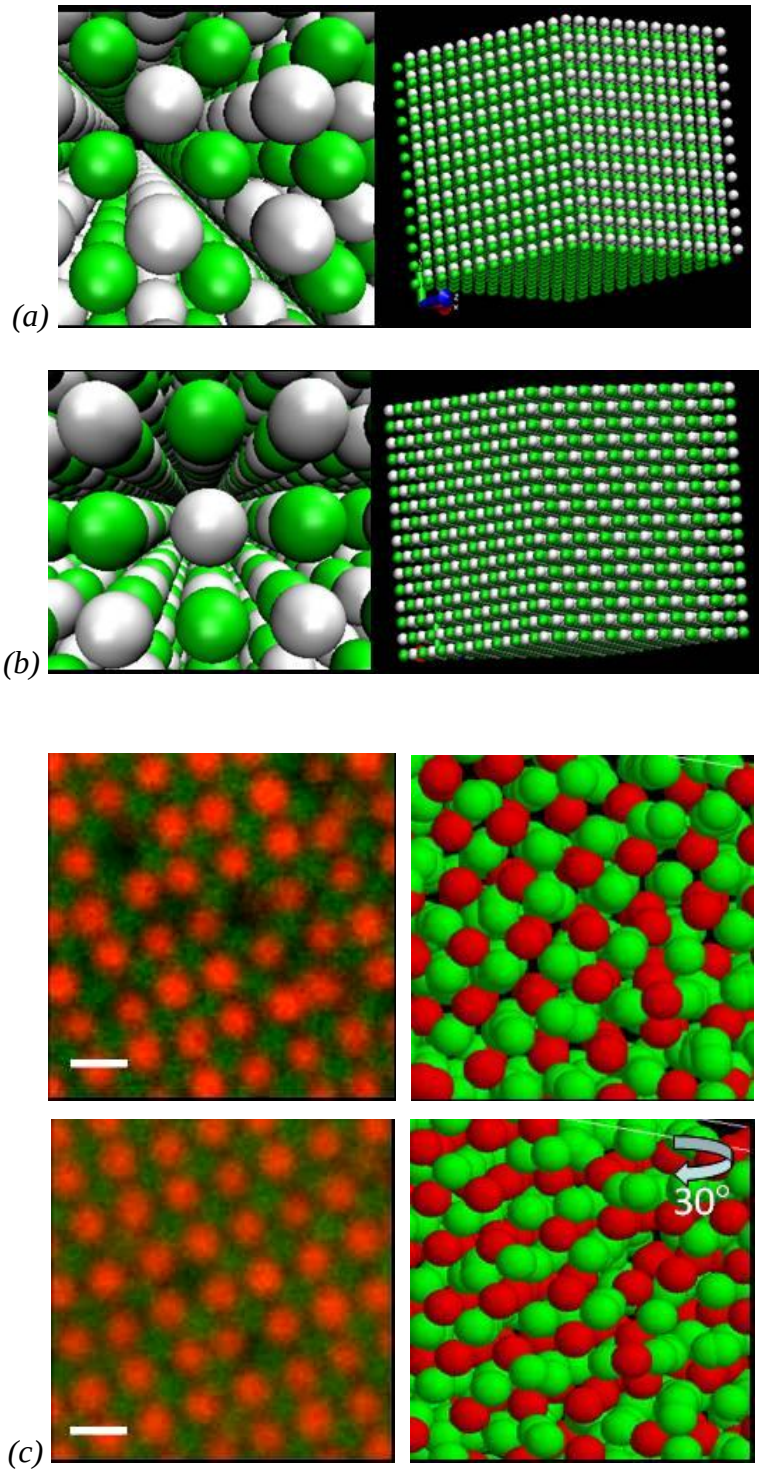

Figure 3.9 – Three-dimensional renderings of (a) perfect cesium chloride crystal, (b) perfect sodium chloride crystal, and (c) CLSM images and associated RASMOL renderings of PHSA-PMMA and DPDMS-PMMA ionic colloidal crystal. Scale bars in CLSM images (c) are 1μm.

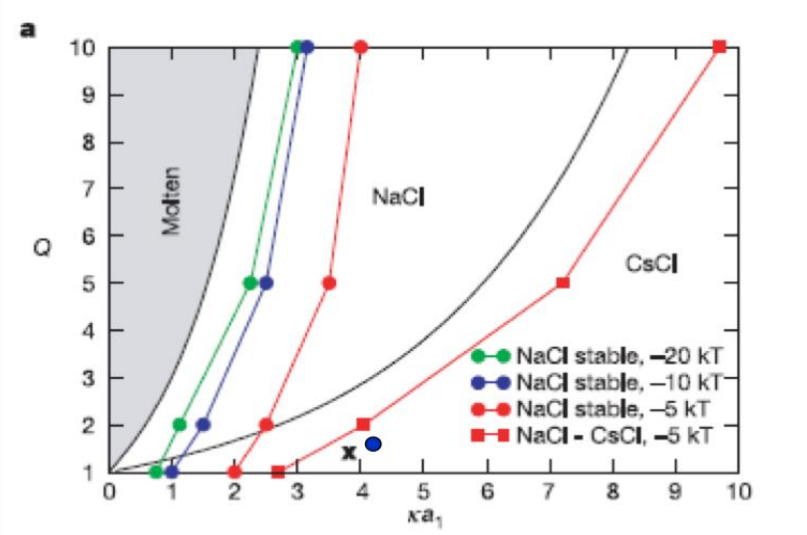

Figure 3.10 – Phase diagram for ionic colloidal crystallization as presented by Leunissen et al. [17]. Phase boundaries determined from simulation based on energy calculations at zero temperature (no entropy, black line), -5 kT (red line), -10 kT (blue line), and -20 kT (green line).

3.3.5. Variation of CHB/decalin Ratio and Initial Volume Fraction

An examination of the range of ionic colloidal crystallization was done by variation of the CHB/decalin ratio and initial volume fraction. Figure 3.11 shows the range of ionic colloidal crystallization observed as a function of initial volume fraction and CHB/decalin ratio. At the lower initial volume fractions (ϕ_i = 0.01 and 0.03), no crystallization was seen regardless of the CHB/decalin ratio. For an initial volume fraction of 0.12, crystallization took place at CHB/decalin ratios of 60/40 and 70/30 (Leunissen et al. [17] condition). At an initial volume fraction of 0.18, crystallization was observed between CHB/decalin ratio of 50/50 and 70/30. At ϕ_i = 0.24, crystallization was observed at all CHB/decalin ratios.

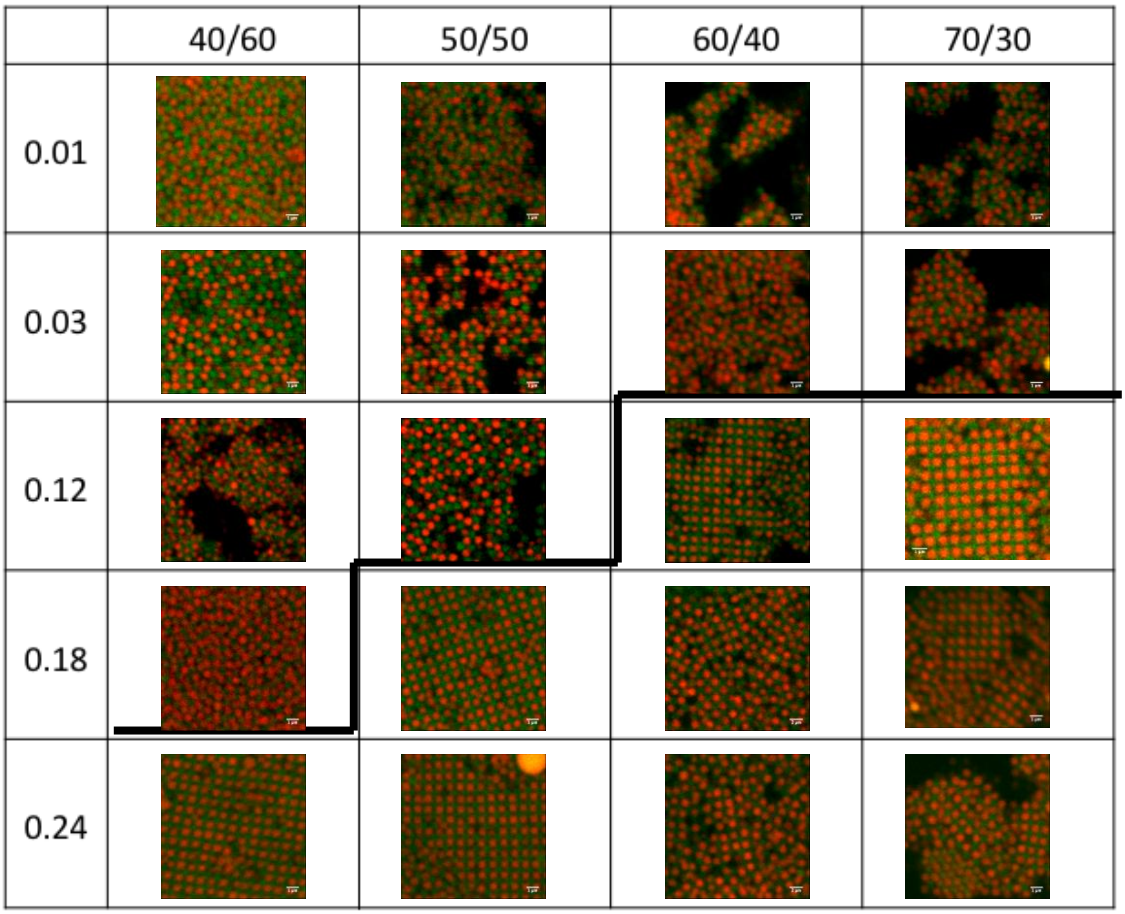

Figure 3.11 – Ionic colloidal crystallization as function of initial volume fraction (left-hand column) and CHB/decalin ratio (top row). Bold line indicates boundary between crystalline and non-crystalline regions.

3.3.6. Relation between CHB/decalin Ratio and Peclet Number

Table 3.1 presents the dimensionless Peclet number as it relates to CHB/decalin ratio and sedimentation velocity. PHSA-PMMA and DPDMS-PMMA particles were dispersed in CHB/decalin containing 6mM TBAC. An initial volume fraction of 0.12 was used. For CHB/decalin ratios around the reference point (CHB/decalin = 70/30), the Peclet number was calculated to be on the order of 10^{-2}. This translated into a relatively slow sedimentation rate (on average ~ 0.21 μm/s). When the CHB mass percent was increased

above 71%, the sedimentation velocity decreased further translating into a smaller Peclet number. Decreasing the CHB mass percent below 69% led to rapid increase in the sedimentation velocity. The Peclet number in turn increased. Error in the sedimentation velocity calculation originates from the accuracy of each height reading using a caliper. Accuracy in the reading is to within 0.1mm. For the Peclet number, error is associated with particle size variation and the calculated sedimentation velocity.

At a CHB/decalin ratio around 70/30, the PHSA-PMMA and DPDMS-PMMA particles were near density matched to the CHB/decalin solvent. As the Peclet number is the ratio of the convective forces to diffusive forces, the slow sedimentation at high CHB mass percents indicates the diffusive (thermal) forces dominate. At low CHB mass percents, where there is greater mismatch between the particles and solvent densities, the convective forces (i.e. gravitational forces) control the sedimentation and whether or not crystallization is seen in the samples.

Table 3.1 – Peclet number calculation based on measured sedimentation velocities for various CHB/decalin ratios at an initial volume fraction of 0.12

CHB Mass %	**Decalin Mass %**	**Sedimentation Velocity (μm/s)**	**Peclet Number**
30	70	2.64 (± 0.03)	0.66 (± 0.02)
40	60	1.39 (± 0.02)	0.36 (± 0.01)
50	50	1.25 (± 0.03)	0.34 (± 0.01)
55	45	1.13 (± 0.02)	0.30 (± 0.01)
58	42	0.90 (± 0.07)	0.24 (± 0.01)
60	40	0.79 (± 0.06)	0.21 (± 0.02)
65	35	0.65 (± 0.05)	0.16 (± 0.04)
69	31	0.45 (± 0.07)	0.10 (± 0.04)
71	29	0.21 (± 0.09)	0.09 (± 0.03)
75	25	0.14 (± 0.08)	0.04 (± 0.03)
77	23	0.07 (± 0.04)	0.02 (± 0.01)

Figure 3.12 plots the calculated Peclet number as function of CHB mass percent at an initial volume fraction of 0.12. For low values of the Peclet number, crystallization (blue squares) was observed in all samples. This corresponded to high values of the CHB mass percent. A transition from crystalline to non-crystalline was found around a Peclet number of 0.22. For Peclet numbers higher than 0.22, corresponding to lower CHB mass percent, crystallization was not observed in any of the samples. The Peclet number had a

linear relationship with the CHB/decalin ratio that could be expressed as $Pe = (0.95 - 0.012x_{CHB})$, where x_{CHB} is the mass fraction of CHB.

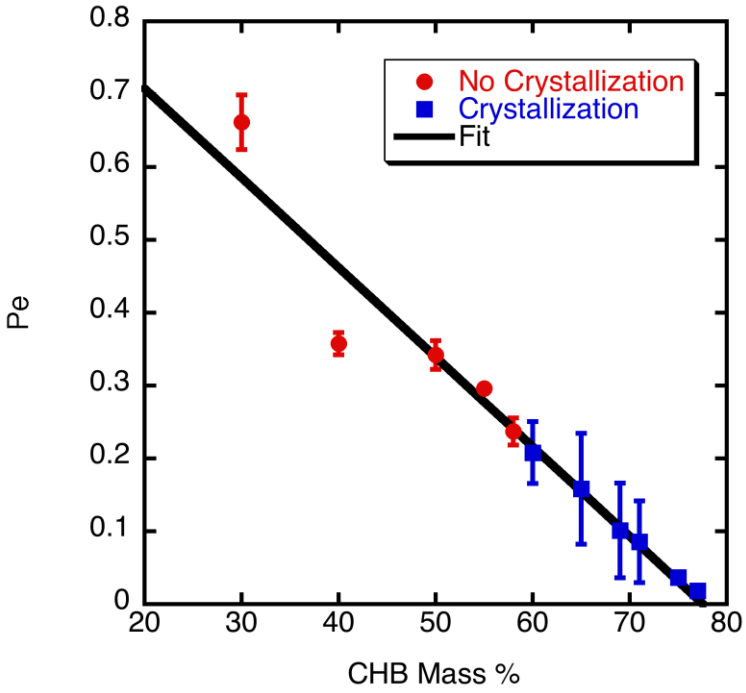

Figure 3.12 – Peclet number as a function of CHB/decalin ratio for solutions of 660 nm PHSA-PMMA and 609 nm DPDMS-PMMA particles. Concentration of TBAC was 6mM and initial volume fraction of solutions was 0.12. Line is best fit to the data points. Error bars represent the standard error of the mean for each condition.

3.3.7. Peclet Number Relation to Ionic Colloidal Crystallization

Figure 3.13 presents the range of ionic colloidal crystallization as a function of the Peclet number and initial volume fraction. For low initial volume fraction, no crystallization is observed at any Peclet number. An amorphous phase is found at all conditions. This indicates there is a minimum initial volume fraction needed to induce crystallization. At an initial volume fraction of 0.12, crystallization is seen for Peclet number values up to 0.21, as reported in the previous section. For an initial volume fraction of 0.18,

crystallization was seen up to a Peclet number of 0.34. At an initial volume fraction of 0.24, crystallization is seen at all Peclet numbers. It is known that the Peclet number is a function of the initial volume fraction [1, 11]. Therefore, it is believed the increase in the initial volume fraction caused a decrease in the Peclet number. As such, the potential for crystallization to take place at lower CHB mass fractions increased as the initial volume fraction increased.

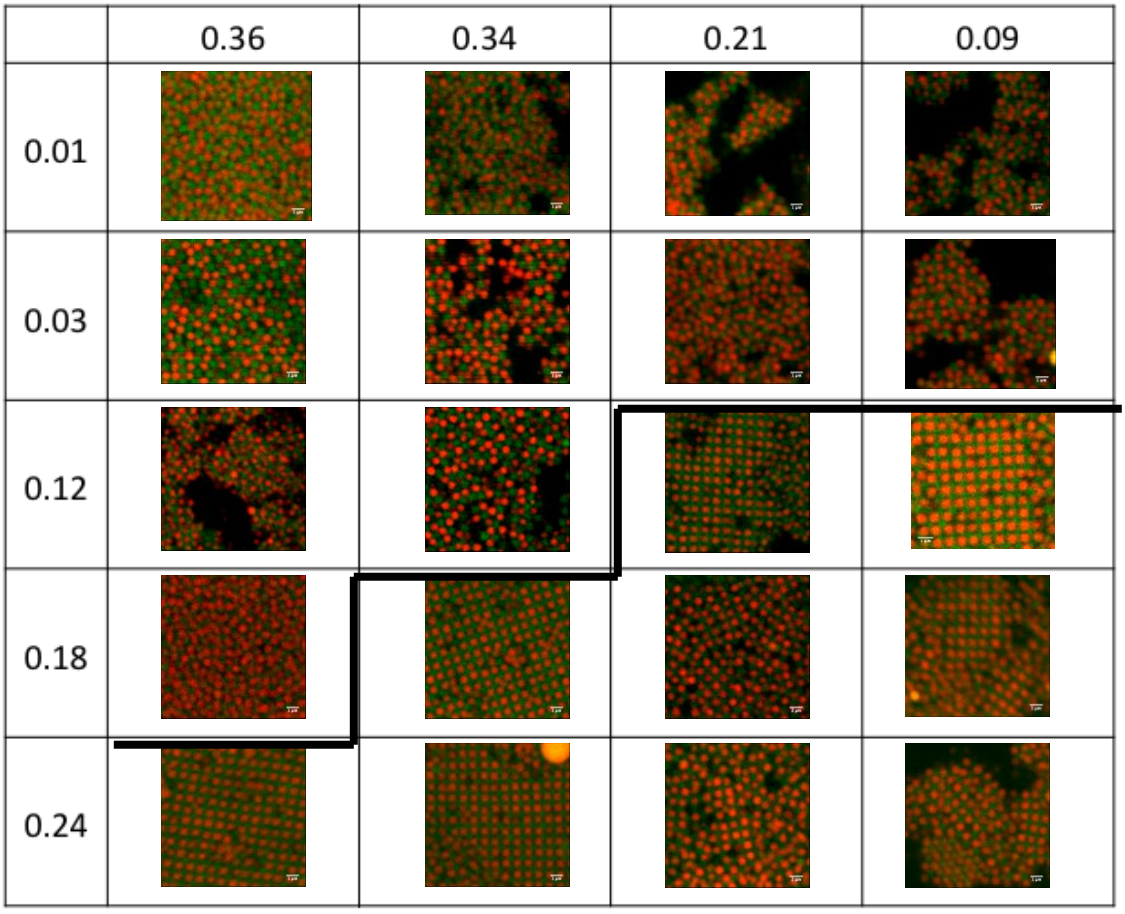

Figure 3.13 - Ionic colloidal crystallization as function of initial volume fraction (left-hand column) and Peclet number (top row). Bold line indicates boundary between crystalline and non-crystalline regions. Re-plot of Figure 3.11.

Figure 3.14 is a plot of crystallization results for the Peclet number and initial volume fractions studied. The orange symbols represent non-crystalline points. Black symbols represent crystalline points. As seen in Figure 3.8, there is no crystallization observed for the lowest initial volume fractions at any of the studied CHB/decalin ratios. The region for crystallization increases as the initial volume fraction increases. Eventually, the point is reached where crystallization is found for all conditions. A comparison to previous work shows that the result of this work is opposite to that found by others. The blue line in the plot represents the upper limit where Davis et al. indicates crystallization should take place. Specifically, for hard spheres, crystallization is expected for low initial volume fractions and low Peclet number [1]. No crystallization is seen for high initial volume fraction. Further discussion is presented in section 3.4.2.

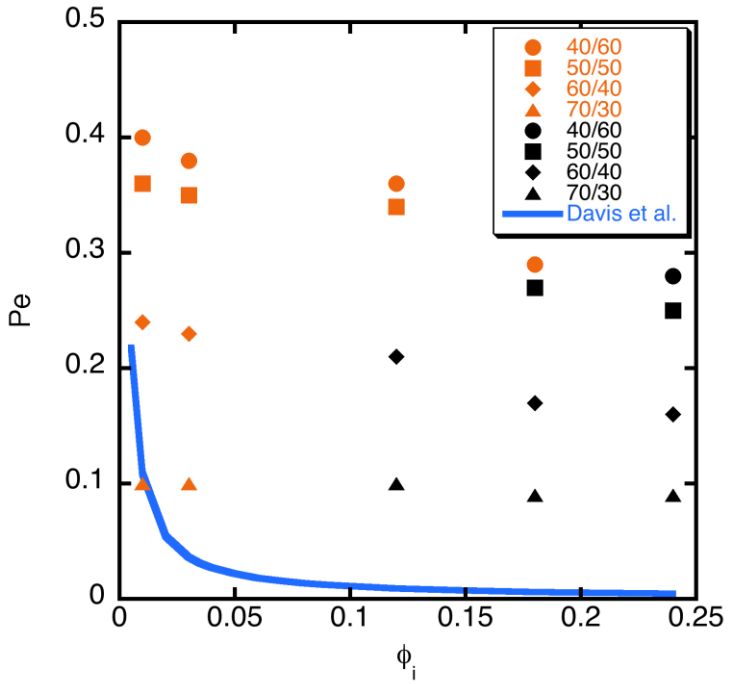

Figure 3.14 – Peclet number as a function of initial volume fraction for PHSA-PMMA and DPDMS-PMMA particles in CHB/decalin. Orange symbols indicate non-crystalline result. Black symbols indicate crystalline result.

3.4. Discussion

3.4.1. Peclet Number Calculation Methodology

In developing the method for computing the Peclet number, a question arose with regards to performing the sedimentation velocity measurements in vials as opposed to capillary cells. All crystallization experiments are done using capillary cells (I.D. = 2mm, O.D. = 6mm). The reason is that it was much easier to visualize the sample using the confocal microscope as opposed to using a vial. In addition, the smaller quantities (10-15μL) extended the life of the samples that were prepared for reproducibility purposes. Performing the sedimentation velocity measurements in vials was convenient because visualization with the eye was far easier than trying to measure the sedimentation rate in a capillary cell that had an inner diameter that was six times smaller than the diameter of the vial. The dimensions of the vials used were 12mm O.D x 35mm length and had a volumetric capacity of 2mL. To confirm uniformity in sedimentation, samples were placed in both vials and capillary cells, and the sedimentation was monitored over three hours. Visual inspection was done every hour. It was determined that there were no significant differences in the rate at which the particles settled in either the capillary cell or the vial.

Additionally, a caliper was used to measure the distance between the solvent meniscus and the top of the sediment. The caliper was accurate to within 0.1mm. Error associated with using the caliper originated with visually identifying the bottom of the meniscus and top of the sediment in each of the samples. Care had to be used not to disturb the sediment when measuring the separation distance. To minimize the error with using the caliper, five measurements of the distance between the top of the sediment and bottom of

the meniscus were made. In each case, a visual measurement was done using the caliper and the distance recorded. The distances were then averaged and the sedimentation velocity computed.

Accuracy in measurements with the caliper was confirmed by computing the sedimentation velocity of polystyrene in water. Polystyrene beads (σ = 1.148μm, ρ = 1.05 g/mL) were dispersed in water at a volume fraction of 0.048. A vortex mixer was used to thoroughly disperse the beads. The beads were allowed to sediment for 26 hours. Using the caliper, the distance between the meniscus and top of the sediment was measured to be 3.1 ± 0.3 mm. This translated into a sedimentation velocity of 0.119μm/hr. Using equation 3-3, the sedimentation velocity, based on the known physical properties of polystyrene in water, was calculated to be 0.129μm/hr. The relative error associated with using the caliper was determined to be approximately 8%. We acknowledge this error is slightly high and other possible methods for refining the accuracy in measuring the sedimentation velocity (e.g. using a fast motion camera to track the changes in height) should be considered.

At higher CHB/decalin ratios, those greater than 71/29, the measurement of the sedimentation velocity was more difficult due to the very slow rate at which the particles settled in the solvent. The height between the sediment and meniscus were approximately 0.5mm after one hour. With the caliper accuracy being ±0.1mm, the actual error in the measurement at these CHB/decalin ratios was approximately 20%. To improve the accuracy, measurements were taken at 2 and 3 hours instead of the 1-hour

time point set for the other samples. The measured distances were divided by the appropriate time to compute the sedimentation velocity. Again, the same approach used to compute the sedimentation velocity for the other samples was used for the higher CHB/decalin ratio samples.

3.4.2. Comparison of Ionic Colloidal Crystallization to Hard-Sphere Crystallization

In section 3.3.7, we presented results relating the Peclet number to ionic colloidal crystallization. We are interested in understanding how our findings compare to other crystallization studies. Of particular interest are studies that focused on sedimentation of hard-sphere systems [1, 6, 12, 14] and how those findings parallel ionic colloidal crystallization. Leunissen et al. [17] presented a thorough analysis of the thermodynamics behind ionic colloidal crystallization. They showed the various structures one could obtain and the different factors that controlled the formation of those structures. These factors included finding the right balance in the charge ratio, size ratio, and Debye length. Striking this balance, one could observe thermodynamically-stable structures that included not only atomic analogs (e.g. CsCl and NaCl) but also unusual structures combining different sized particles (e.g. LS_6 and LS_8). Thermodynamics is one key to readily creating ionic colloidal crystals. The other half of the equation is the kinetics to such crystallization.

In trying to understand the kinetics behind ionic colloidal crystallization, we compared our findings with those of hard-sphere systems. Davis et al. [1] showed that crystallization of hard spheres generally takes place at low Peclet numbers and low initial

volume fractions. The Peclet number times the initial volume fraction was determined to be typically on the order of 10^{-3}. In other words, crystallization at higher Peclet number values is not possible because the sedimentation rate of the particles exceeds the rate of crystal growth. When comparing our results to the findings of Davis et al., we found the reverse to be true. At lower Peclet number and lower initial volume fraction, crystallization did not take place for any condition studied. Yet, at the highest initial volume fraction ($\phi_i = 0.24$), crystallization was observed at all Peclet number conditions (see Figure 3.13). One possible explanation for this observation focuses on the fundamental differences of the two systems. Our system has ionic interactions that play a role in how this type of crystal forms. Whereas hard-sphere systems do not have interactions due to charge, our system does and we must account for these interactions.

Another possible mechanism considered revolved around the nature of screening our systems. Unlike their atomic counterparts, the charge on colloidal particles is normally screened through the use of an electrolyte. We used TBAC as the electrolyte in our systems. We hypothesized that the degree of screening changed how the particles packed and therefore controlled what structure formed, if any. Combined with the rate at which the particles settled, the level of screening could be key at how these systems form the crystal structures that are observed. At a lower initial volume fraction, the slower sedimentation with high screening (i.e. larger κa) could prevent crystallization from taking place. Instead, amorphous and/or aggregated systems would be observed.

To further explore how ionic colloidal crystals form, a time lapse analysis of our system was done. It provided some insights into how these ionic colloidal crystals formed. Using the CLSM, a time series of 61 images was taken over a 1-hour period. A nucleation point was found within the sample and the growth of the crystal tracked. Initially, the particles were fully dispersed and freely moving in the solution. After 10 minutes, the first signs of crystallization were noted. It was clear that the ionic interactions between the PHSA-PMMA and DPDMS-PMMA particles were dominating as sedimentation occurred. It is suspected that the increase in the initial volume further promoted the ionic interactions. This, in turn, led to an increase in the potential for crystallization to take place in these systems. We could only make qualitative assessments of how the crystal grew over the course of the hour and beyond. A quantitative analysis is needed to fully understand the scope of the kinetics to ionic colloidal crystallization.

3.4.3. Polydispersity Effects on Crystallization

Polydispersity is an important topic to be considered in any colloidal crystal study. It is preferred that particles are monodispersed (polydispersity less than 2% of the mean particle diameter) in order to achieve high quality crystals with long-range ordering. Yet, colloidal particle are not monodispersed. Polydispersed systems may yield crystallization, however, the quality of the crystals are poor and subject to fractionation and defects. A study of hard-sphere systems that have a polydispersity ranging from 2-10% tended to produce two-phase systems, of which one was crystalline [44]. The PMMA particles used in this study had a measured polydispersity of 4% (PHSA-PMMA)

and 3% (DPDMS-PMMA). The behavior of PMMA particles with polydispersity values below this threshold does not vary significantly and mimic those of purely monodispersed systems.

Of particular interest in this study was the discovery of the interaction of significantly larger PHSA-PMMA particles with the overall ionic system. The first image in Figure 3.10 shows some of these larger PHSA-PMMA particles. It was anticipated that these larger particles would disrupt the growth of the ionic crystal. Since the particles pack in specific configurations in order to maximize their entropy, any perturbations should cause the break down of the crystal. To our surprise, the larger PHSA-PMMA particles promoted the growth of these ionic crystals. As the crystal began to propagate laterally, the larger particles did not stop the growth of the crystal. Instead, the DPDMS-PMMA particles tended to form rings around the larger PHSA-PMMA particles allowing the ionic chain to maintain itself and crystal growth to continue. One hypothesis for this observed behavior is that the charge on the larger PHSA-PMMA particles was the same as that of its smaller counterpart. As such, instead of aggregation taking place, the particles moved into an ordered phase. Additional experiments would need to be done to confirm this hypothesis.

3.5. Conclusion

We have presented a study on the sedimentation of ionic colloidal particles. The goal of this work was to understand the kinetics behind ionic colloidal crystallization. Using PHSA-PMMA (negatively-charged) and DPDMS-PMMA (positively-charged) particles,

an investigation was performed to quantify the growth of ionic colloidal crystals using the technique of sedimentation. We found that the depth of forming such crystals depended on the density difference between the particles and solvent. Quantification of this parameter was done by calculating the Peclet number (Pe). At higher initial volume fraction, the probability for forming ionic colloidal crystals increased across all CHB/decalin ratios. Ionic colloidal crystals were observed at the highest initial volume (ϕ_i = 0.24) fraction and fastest sedimentation rate (CHB/decalin = 40/60; Pe = 0.36). Crystallization was not obtainable at low initial volume fraction and low Peclet number. This finding is opposite to what has been reported for hard-sphere crystallization. Based on the work of Davis et al. [1], we believe that an alternate mechanism for forming ionic colloidal crystals exists but has not been fully understood.

Future work should focus on further quantification of the crystal growth over time. One suggestion would be to track the growth of these crystals by measuring the crystalline volume fraction of a control volume over a specific time period (e.g. 3 hours). Such a study would allow for a more accurate read on how the oppositely-charged particles behave and order themselves. Another suggestion would be to extend the range of sedimentation rates. While this study was able to gain a good read on the degree of crystallization possible by varying the density difference, additional questions remain. For example, what happens when the initial volume fraction is increased to 0.30 or 0.35? Does crystallization take place or does another phase form (e.g. glass)? Finally, simulations should be utilized to understand what is believed to be a nucleation and growth scenario. Simulations would be invaluable at helping to explain the differences

between our finding and what has been published on colloidal crystallization under sedimentation.

References

1. Davis, K.E., W.B. Russel, and W.J. Glantschnig, *Settling Suspensions of Colloidal Silica - Observations and X-Ray Measurements.* Journal of the Chemical Society-Faraday Transactions, 1991. **87**(3): p. 411-424.
2. Anderson, V.J. and H.N.W. Lekkerkerker, *Insights into phase transition kinetics from colloid science.* Nature, 2002. **416**(6883): p. 811-815.
3. Hachisu, S., Kobayash.Y, and A. Kose, *Phase Separation in Monodisperse Latexes.* Journal of Colloid and Interface Science, 1973. **42**(2): p. 342-348.
4. Kegel, W.K. and A. van Blaaderen, *Direct observation of dynamical heterogeneities in colloidal hard-sphere suspensions.* Science, 2000. **287**(5451): p. 290-293.
5. Pham, K.N., A.M. Puertas, J. Bergenholtz, S.U. Egelhaaf, A. Moussaid, P.N. Pusey, A.B. Schofield, M.E. Cates, M. Fuchs, and W.C.K. Poon, *Multiple glassy states in a simple model system.* Science, 2002. **296**(5565): p. 104-106.
6. Pusey, P.N. and W. Vanmegen, *Phase-Behavior of Concentrated Suspensions of Nearly Hard Colloidal Spheres.* Nature, 1986. **320**(6060): p. 340-342.
7. Yethiraj, A. and A. van Blaaderen, *A colloidal model system with an interaction tunable from hard sphere to soft and dipolar.* Nature, 2003. **421**(6922): p. 513-517.
8. Pusey, P.N., W.C.K. Poon, S.M. Ilett, and P. Bartlett, *Phase-Behavior and Structure of Colloidal Suspensions.* Journal of Physics-Condensed Matter, 1994. **6**: p. A29-A36.
9. Sirota, E.B., H.D. Ouyang, S.K. Sinha, P.M. Chaikin, J.D. Axe, and Y. Fujii, *Complete Phase-Diagram of a Charged Colloidal System - a Synchrotron X-Ray-Scattering Study.* Physical Review Letters, 1989. **62**(13): p. 1524-1527.
10. Ilett, S.M., A. Orrock, W.C.K. Poon, and P.N. Pusey, *Phase-Behavior of a Model Colloid-Polymer Mixture.* Physical Review E, 1995. **51**(2): p. 1344-1352.
11. Russel, W.B., Saville, D. A., Schowalter, W. R., *Colloidal Dispersions*. 1 ed. Cambridge Monographs on Mechanics and Applied Mathematics, ed. G.K. Batchelor. 1989, Cambridge: Cambridge University Press. 525.
12. Davis, K.E., W.B. Russel, and W.J. Glantschnig, *Disorder-to-Order Transition in Settling Suspensions of Colloidal Silica - X-Ray Measurements.* Science, 1989. **245**(4917): p. 507-510.
13. Leunissen, M.E., M.T. Sullivan, P.M. Chaikin, and A. van Blaaderen, *Concentrating colloids with electric field gradients. I. Particle transport and growth mechanism of hard-sphere-like crystals in an electric bottle.* Journal of Chemical Physics, 2008. **128**(16): p. -.
14. Ackerson, B.J., S.E. Paulin, B. Johnson, W. van Megen, and S. Underwood, *Crystallization by settling in suspensions of hard spheres.* Physical Review E, 1999. **59**(6): p. 6903-6913.
15. Shereda, L.T., R.G. Larson, and M.J. Solomon, *Local stress control of spatiotemporal ordering of colloidal crystals in complex flows.* Physical Review Letters, 2008. **101**(3): p. -.

16. Royall, C.P., R. van Roij, and A. van Blaaderen, *Extended sedimentation profiles in charged colloids: the gravitational length, entropy, and electrostatics.* Journal of Physics-Condensed Matter, 2005. **17**(15): p. 2315-2326.
17. Leunissen, M.E., C.G. Christova, A.P. Hynninen, C.P. Royall, A.I. Campbell, A. Imhof, M. Dijkstra, R. van Roij, and A. van Blaaderen, *Ionic colloidal crystals of oppositely charged particles.* Nature, 2005. **437**(7056): p. 235-240.
18. Vermolen, E.C.M., A. Kuijk, L.C. Filion, M. Hermes, J.H.J. Thijssen, M. Dijkstra, and A. van Blaaderen, *Fabrication of large binary colloidal crystals with a NaCl structure.* Proceedings of the National Academy of Sciences of the United States of America, 2009. **106**(38): p. 16063-16067.
19. Hilhorst, J., V.V. Abramova, A. Sinitskii, N.A. Sapoletova, K.S. Napolskii, A.A. Eliseev, D.V. Byelov, N.A. Grigoryeva, A.V. Vasilieva, W.G. Bouwman, K. Kvashnina, A. Snigirev, S.V. Grigoriev, and A.V. Petukhov, *Double Stacking Faults in Convectively Assembled Crystals of Colloidal Spheres.* Langmuir, 2009. **25**(17): p. 10408-10412.
20. Solomon, T. and M.J. Solomon, *Stacking fault structure in shear-induced colloidal crystallization.* Journal of Chemical Physics, 2006. **124**(13): p. -.
21. Beckham, R.E. and M.A. Bevan, *Interfacial colloidal sedimentation equilibrium. I. Intensity based confocal microscopy.* Journal of Chemical Physics, 2007. **127**(16): p. -.
22. Lu, M., M.A. Bevan, and D.M. Ford, *Interfacial colloidal sedimentation equilibrium. II. Closure-based density functional theory.* Journal of Chemical Physics, 2007. **127**(16): p. -.
23. Bartlett, P., R.H. Ottewill, and P.N. Pusey, *Superlattice Formation in Binary-Mixtures of Hard-Sphere Colloids.* Physical Review Letters, 1992. **68**(25): p. 3801-3804.
24. Filion, L. and M. Dijkstra, *Prediction of binary hard-sphere crystal structures.* Physical Review E, 2009. **79**(4): p. -.
25. Royall, C.P., M.E. Leunissen, and A. van Blaaderen, *A new colloidal model system to study long-range interactions quantitatively in real space.* Journal of Physics-Condensed Matter, 2003. **15**(48): p. S3581-S3596.
26. Islam, A.M., B.Z. Chowdhry, and M.J. Snowden, *Temperature-Induced Heteroflocculation in Particulate Colloidal Dispersions.* Journal of Physical Chemistry, 1995. **99**(39): p. 14205-14206.
27. Graham-Rowe, D., *A new light in dentistry.* Nature Photonics, 2008. **2**(12): p. 705-707.
28. Graham-Rowe, D., *Tunable structural colour.* Nature Photonics, 2009. **3**(10): p. 551-553.
29. Graham-Rowe, D., *From dots to devices.* Nature Photonics, 2009. **3**(6): p. 307-309.
30. Graham-Rowe, D., *A new twist to tuning lasers.* Nature Photonics, 2009. **3**(4): p. 182-183.
31. Graham-Rowe, D., *Sounding out photons.* Nature Photonics, 2009. **3**(3): p. 123-125.
32. Graham-Rowe, D. and R. Won, *Photonic tasting.* Nature Photonics, 2009. **3**(2): p. 69-71.

33. Li, T., R.B. Xing, W.H. Huang, and Y.C. Han, *A self-assembly approach to fabricate the patterned colloidal crystals with a tunable structure.* Colloids and Surfaces a-Physicochemical and Engineering Aspects, 2005. **269**(1-3): p. 22-27.
34. Liddell, C.M. and C.J. Summers, *Nonspherical ZnS colloidal building blocks for three-dimensional photonic crystals.* Journal of Colloid and Interface Science, 2004. **274**(1): p. 103-106.
35. Liu, K., T.A. Schmedake, and R. Tsu, *Experimental determination of the band structure of photonic crystals of colloidal silica spheres.* Physics Letters A, 2009. **373**(21): p. 1885-1890.
36. Norris, D.J., *A view of the future.* Nature Materials, 2007. **6**(3): p. 177-178.
37. Hoogenboom, J.P., D. Derks, P. Vergeer, and A. van Blaaderen, *Stacking faults in colloidal crystals grown by sedimentation.* Journal of Chemical Physics, 2002. **117**(24): p. 11320-11328.
38. Pawley, J.B., *Handbook of biological confocal microscopy*. 2nd ed. 1995, New York: Plenum Press. xxiii, 632 p.
39. Kogan, M., C.J. Dibble, R.E. Rogers, and M.J. Solomon, *Viscous solvent colloidal system for direct visualization of suspension structure, dynamics and rheology.* Journal of Colloid and Interface Science, 2008. **318**(2): p. 252-263.
40. Solomon, M.J., Kogan, M., *Confocal Optical Microscopy.* Encyclopedia of Condensed Matter Physics, 2005: p. 229-235.
41. Obrien, R.W. and L.R. White, *Electrophoretic Mobility of a Spherical Colloidal Particle.* Journal of the Chemical Society-Faraday Transactions Ii, 1978. **74**: p. 1607-1626.
42. *CRC Handbook of Chemistry and Physics*. 90 ed, ed. D.R. Lide. 2009: Taylor & Francis, Inc. 2804.
43. Crocker, J.C. and D.G. Grier, *Methods of digital video microscopy for colloidal studies.* Journal of Colloid and Interface Science, 1996. **179**(1): p. 298-310.
44. Wette, P., H.J. Schope, and T. Palberg, *Enhanced crystal stability in a binary mixture of charged colloidal spheres.* Physical Review E, 2009. **80**(2): p. -.

CHAPTER 4

CONCLUSION AND FUTURE WORK

Conclusion

In this dissertation, we have investigated the assembly of colloidal particles by characterization of their interactions using confocal laser scanning microscopy (CLSM). Using confocal microscopy permitted us to study the behavior of three dimensional, collective structures of one-component and two-component systems. This, in turn, enabled us to characterize these systems at the single particle level allowing for quantification of specific properties and development of a methodology for capturing colloidal pair interaction potentials.

In Chapter 2, an experimental methodology for computing the pair interaction potential was presented. Charged colloidal particles made of poly(methyl methacrylate) (PMMA) stabilized by poly-12-hydroxystearic acid (PHSA) were dispersed in dioctyl phthalate (DOP). The viscosity of DOP retarded the velocity of the particles allowing for 3-D imaging to be done using CLSM. In conjunction with simulations the following methodology was validated. Dilute suspensions of PHSA-stabilized PMMA particles ($\phi < 0.05$) were prepared and imaged on the CLSM. The number of image volumes collected at each volume fraction increased as the volume fraction decreased. This was to improve statistics in the data and minimize the noise produced from Brownian motion

and the CLSM. Using image processing techniques, the average radial distribution function, *g(r)*, was computed for each volume fraction. The potential of mean force, *w(r)*, was calculated from each radial distribution function. Based on the findings from simulations, a criteria for diluteness was set such that *w(r)* was required to scale linearly with the volume fraction in order to be considered dilute. Using only those volume fractions that met this criteria, linear extrapolation back to the limit of infinite dilution was performed. The pair potential, *U(r)*, is located within this limit based on the definition from statistical mechanics [1]. Upon completing the extrapolation at each radial separation, the *U(r)* curve was constructed.

To confirm our methodology, we considered the cases where screening of the repulsive interactions was implemented. Working with low (10μM) and high (2mM) concentrations of tetrabutylammonium chloride (TBAC) salt, the same procedure as done for the no salt case was performed. Simulations determined that screening of the repulsive interactions increased the maximum volume fraction in which our methodology would work. Experiments confirmed the results from simulations and results were presented. In comparing all three cases, we found that high screening of the repulsive interactions caused the particles to exhibit hard sphere-like behavior. To further confirm our results, we applied the screened Yukawa (Coulomb) potential to all three cases. Characterization parameters needed for the theoretical potential were obtained from conductivity and zeta potential measurements. The experimental data showed very good agreement with the theoretical potential. Our proposed experimental methodology for obtaining the pair interaction potential is promising because it allows for direct access to

the pair potential without the need of simulations to match a known potential and radial distribution function to the experimental data.

In Chapter 3, we examined the assembly of oppositely-charged particles using the technique of sedimentation. PHSA-stabilized PMMA particles and PMMA particles stabilized by poly(diphenyl dimethyl siloxane) (DPDMS) were dispersed at dilute concentrations in a mixture of cyclohexyl bromide (CHB) and decalin containing 6mM TBAC. The mass ratio of CHB and decalin varied from 30/70 to 80/20 CHB/decalin. This spread of ratios was chosen to assess the range of possible crystallization that could be obtained under sedimentation. The charge on the particles at each CHB/decalin ratio was assessed by measuring the charge mobility and computing the zeta potential. We found that charge across the range of CHB/decalin ratios studied were within the standard deviation of the mean charge for both particles. Following the procedure of Leunissen et al. [2], reproduction of ionic colloidal crystals was achieved at a CHB/decalin mass ratio of 71/29. Varying the CHB/decalin ratio and initial volume fraction (ϕ_i = 0.01 to 0.24), we observed ionic colloidal crystallization take place when the initial volume fraction was 0.12 or greater. Depending on the initial volume fraction, crystallization was observed at all CHB/decalin ratios.

To further understand the crystallization trend we qualitatively observed, we examined the results of Davis et al. [3] to determine if our results agreed with those seen for hard-sphere crystallization. Davis reported that hard-sphere crystallization took place under conditions where both the initial volume fraction and sedimentation rate were low. The

sedimentation rate was quantified by the dimensionless Peclet number, which is the ratio of the convective forces to the diffusive forces. Lower Peclet numbers translated to slower sedimentation rates while the opposite was true of higher Peclet numbers. We computed the Peclet numbers of our samples by experimentally measuring the sedimentation rate at different CHB/decalin ratios. A linear relationship was found between the Peclet number and the CHB/decalin ratio. Plotting Peclet number versus initial fraction, we found that ionic colloidal crystallization took place at high Peclet numbers and high initial volume fractions. This is directly opposite the Davis results indicating a different mechanism exists for crystallization in our systems.

Future Work

Assembly of colloidal particles is of great importance in advancing fields such as photonics and sensing applications. This is especially important in areas where the desire is to move from the infrared or UV spectrum and into the visible spectrum [4, 5]. Direct access to the pair interaction potential from experiments is important since one can tune systems of colloidal particles to achieve a desired crystallization effect. The studies in this dissertation provide examples of how quantitative information on colloidal interactions can be directly obtained experimentally and lay a foundation for pursuing these desired applications.

Going forward, there are several items that could be potentially examined. With regards to the developed methodology for characterizing the pair interaction potential, an additional interest would be to understand the validity of the method to attractive

systems. Attractive interactions are important in systems involving gels in addition to crystals. Strong attractions typically result in arrested systems forming gels or aggregates. A next step would be to characterize moderate attractive interactions by adding non-adsorbing polymer to the system presented in Chapter 2. One of the challenges posed by the inclusion of non-adsorbing polymer is finding the point where the attractions can be captured but gelation is avoided. We are uncertain that our method would be valid for strongly attractive systems because of the need to perform linear extrapolation to satisfy the limit where the pair potential is observed. Moderate attraction would allow the particles to touch one another, but the Brownian motion would not be arrested. We have done some initial analysis on this front but additional work is required to fully determine if such systems can be modeled with our methodology.

In Chapter 3, we showed that ionic colloidal crystallization occurred in conditions that were opposite to those for hard sphere crystallization. Our findings are intriguing and a more rigorous quantitative analysis is needed to understand the kinetics we observed. One approach that is suggested is utilizing simulations to model our experimental results. Molecular dynamics (MD) simulations is potentially a useful approach to modeling the motion of these oppositely-charged systems to understand the kinetics of crystallization growth. Using the experimental characterization parameters (i.e. charge number and Debye lengths), it is believed a sufficient model could be obtained that potentially describes what has been seen experimentally. This information will become important as the application of ionic colloidal crystallization develops with time.

Analysis of particle interactions using confocal microscopy techniques can play a major role in understanding nature of colloidal self-assembly. We have investigated the direct assessment of the pair interaction potential with the aim of applying our methodology to tuning colloidal crystallization. Extensions of this research will broaden the current understanding for showing how one can control the range of crystallization that is currently seen as well as what is possible.

References

1. Chandler, D., *Introduction to Modern Statistical Mechanics*. 1987, New York: Oxford University Press. 274.
2. Leunissen, M.E., C.G. Christova, A.P. Hynninen, C.P. Royall, A.I. Campbell, A. Imhof, M. Dijkstra, R. van Roij, and A. van Blaaderen, *Ionic colloidal crystals of oppositely charged particles.* Nature, 2005. **437**(7056): p. 235-240.
3. Davis, K.E., W.B. Russel, and W.J. Glantschnig, *Settling Suspensions of Colloidal Silica - Observations and X-Ray Measurements.* Journal of the Chemical Society-Faraday Transactions, 1991. **87**(3): p. 411-424.
4. Fleischhaker, F. and R. Zentel, *Photonic crystals from core-shell colloids with incorporated highly fluorescent quantum dots.* Chemistry of Materials, 2005. **17**(6): p. 1346-1351.
5. Miguez, H., C. Lopez, F. Meseguer, A. Blanco, L. Vazquez, R. Mayoral, M. Ocana, V. Fornes, and A. Mifsud, *Photonic crystal properties of packed submicrometric SiO2 spheres.* Applied Physics Letters, 1997. **71**(9): p. 1148-1150.

APPENDICES

APPENDIX A

DETERMINING ZETA POTENTIAL USING ZETASIZER NANO SERIES DEVICE

In section 3.3, a charge number analysis of the PHSA-PMMA and DPDMS-PMMA particles used in the ionic colloidal crystallization study was presented. These charge numbers results were calculated from the zeta potential. In this appendix, an in-depth analysis on the zeta potential will be presented. First, the theory behind the zeta potential will be discussed. Next, the experimental approach to measuring the particle mobility and will be outlined. Finally, a discussion on the quality of the results using the zetasizer device to measure the charge mobility will be presented.

A.1. Theory

The zeta potential of a particle is the potential that is found at the boundary called the surface of hydrodynamic shear or slipping plane. The origin of this slipping plane stems from the development of a net charge at the particle surface, which influences the distribution of ions in the surrounding interfacial region. This, in turn, causes an increase in ions of opposite charge. The result is the formation of an electric double layer. The liquid layer surrounding the particle is composed of two parts: the Stern layer, where ions are strongly bound, and a diffuse layer, where particles are loosely attached. Figure A.1 diagrams this effect and shows where the zeta potential is found.

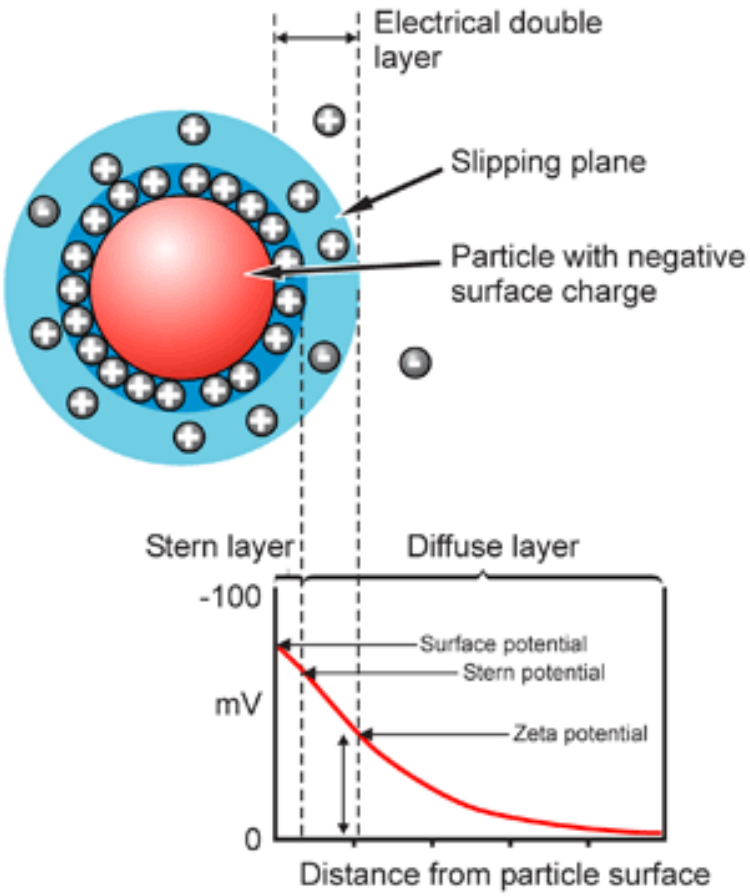

Figure A.1 – Diagram of particle surface charge showing the electric double layer and slipping plane. The zeta potential is found at the slipping plane [1].

The stability of a colloidal system can be determined from the zeta potential. For large values of the zeta potential (positive or negative), particles suspended in a solution will not have a tendency to flocculate and will repel one another. Thus, the particles are considered to be stable. An opposite effect is found for small values of the zeta potential.

The zeta potential is determined from a process called electrophoresis. Electrophoresis is the movement of a particle suspended in a liquid relative to that liquid under an applied electric field [2]. When an electric field is applied, charged particles are attracted to the

opposite electrode. Viscous forces acting on the particles oppose this movement. A constant velocity is achieved once equilibrium is reached between the opposing forces. The velocity of a particle within an electric field is defined as the electrophoretic mobility. A relation between the zeta potential and electrophoretic mobility can be made using the Henry equation:

$$U_E = \frac{2\varepsilon\zeta f(\kappa a)}{3\eta},$$

where U_E is the electrophoretic mobility, ε is the dielectric constant, ζ is the zeta potential, η is the solvent viscosity, and f(κa) is Henry's function. Henry's function can take on one of two values depending on the approximation. For relatively large particles (> 0.2μm) dispersed in electrolytes containing more than 10^{-3} molar salt, f(κa) = 1.5 and is known at the Smoluchowski approximation. For small particles dispersed in non-aqueous media or less than 10^{-3} molar salt, f(κa) = 1 and is known as the Huckel approximation [2].

A.2. Measuring Mobility Using Zetasizer Nano Series ZS

To determine the zeta potential of our experimental systems, the mobility of the particles was determined. A Zetasizer Nano Series ZS (Malvern, United Kingdom) device was used to measure the mobility. This particular zetasizer has the capability to measure size, molecular weight, and the zeta potential. The functionality of the device was limited to particles with sizes ranging from 5nm to 10μm. Dilute suspensions (ϕ = 0.01) were prepared and set aside for measuring. Depending on the solvent, there are two cells that could be used. For aqueous solutions, a folded capillary cell (Figure A.2a) was available.

The advantage of the folded capillary cell was the small quantities of solution that needed to be used per run. We used the folded capillary cell primarily to ensure the device was working properly. This check was done by using zeta potential test standards (model number: DTS0230) obtained directly from Malvern. Upon verification that the device was working properly, we switched to the universal 'dip' cell (Figure A.2b). This cell is constructed to handle non-aqueous solutions. Unlike the folded capillary cell, however, the dip cell required more solution in order to accurately obtain a reading. Therefore, the amount of test solution created (~1.5mL) was enough to allow several independent measurements to be performed.

(a)  *(b)* 

Figure A.2 – Zetasizer Nano Series ZS cells used for measuring the charge mobility and zeta potential. (a) Disposable folded capillary cell used to test standard for calibration of device. Also designed for aqueous system. (b) Universal 'dip' cell used to measure the mobility of organic systems. [3]

Samples were placed into the zetasizer device and the computer program for the zetasizer was loaded. The program allowed users to create their own standard operating procedure (SOP) for their particular sample. Within the SOP subsection, physical properties of many of the common chemicals (e.g. water) were pre-loaded for quick selection. Users

were also allowed to define the properties of special chemicals. Properties required for operating the device included viscosity of the solvent and particle refractive index. Additional inputs into the SOP included number of measurements, number of runs per measurement, type of cell being used, and voltage to be applied across sample. After creating the SOP, the user could run the SOP in one step using the user-friendly computer interface. Upon completing the SOP, the program generated a report which the user could download to either a flash drive directly or into an Excel spreadsheet before transferring to a flash drive. The report included mobility, zeta potential, and conductivity measurements.

The Zetasizer Nano ZS device performs electrophoretic mobility measurements using a patented M3-PALS technique [1, 4]. M3-PALS combines laser Doppler velocimetry and phase analysis light scattering (PALS). The advantage to working with PALS is that it increases the performance to greater than 100 times that associated with standard mobility measurement techniques. PALS allows for the measurement of high conductivity samples in addition to samples in non-aqueous solvents, which typically carry low particle mobilities. The key feature to the M3 technique is that it takes two measurements for each mobility determination.

A.3. Assessing Quality of Results from the Zetasizer Nano ZS

Results from the zetasizer are straightforward to obtain. The program is designed to eliminate extra steps that user may encounter by calculating all of the necessary information internally. Assessing the quality of the results is required to ensure the value

generated for the particle mobility is realistic. We approached the validation of the zetasizer results by examining the phase plots generated by the program. The phase plot provides information regarding the mobility as a function of time. Phase, by definition, is frequency multiplied by time. The Zetasizer Nano Series device uses the M3-PALS technique to measure particle velocities. This is done by applying frequency shifts at slow and fast intervals. Several reversals of the applied electric field are done to ensure the net field in each direction is the same and reduce any effects associated with polarization. The slow field reversal portion gives distribution information while fast field reversal gives the mean velocity [4]. Figure A.3 shows the phase plots for two different cases. As a baseline, we examined the transfer standard (Figure A.3a) to understand what constituted an accurate result. The transfer standard has a known zeta potential of -68mV. Therefore, the negative phase is expected for such case. Key features, which we noted, included the saw tooth (signal) in the short time area (fast field reversal) and the minimization of the noise across the entire phase plot. Noise, associated with thermal drifts, is reduced by increasing the number of runs in each measurement.

In Figure A.3b, the phase plot for 609nm poly(diphenyl dimethyl siloxane) particles dispersed in a mixture of cyclohexyl bromide and decalin with 6mM tetrabutylammonium chloride is shown. As these particles are known to carry a positive charge, we expected to see a positive phase as shown in the plot. Immediately, we observed slightly more noise in this data when compared to the transfer standard. We also noted the saw tooth behavior in the fast field reversal, but the increase in thermal drift was also apparent by the moderate slope in the fast field reversal region. The

increased noise in our samples, when compared to the transfer standard, raised concerns regarding the accuracy of our measurements. The transfer standard was composed of a solution with water as a base. As such, it made diagnosing differences between results challenging since we are working primarily with organic solvents. We minimized the noise by following the protocols outlined by Malvern. By continuously increasing the number of runs per measurement, we were able to reduce the noise and obtain a good result as seen in Figure A.3b. We recommend that a minimum of 150 runs per measurement be done as a baseline when performing these mobility measurements. We also recommend that multiple samples of the same solution be tested to ensure the same results are seen with the device.

(a)

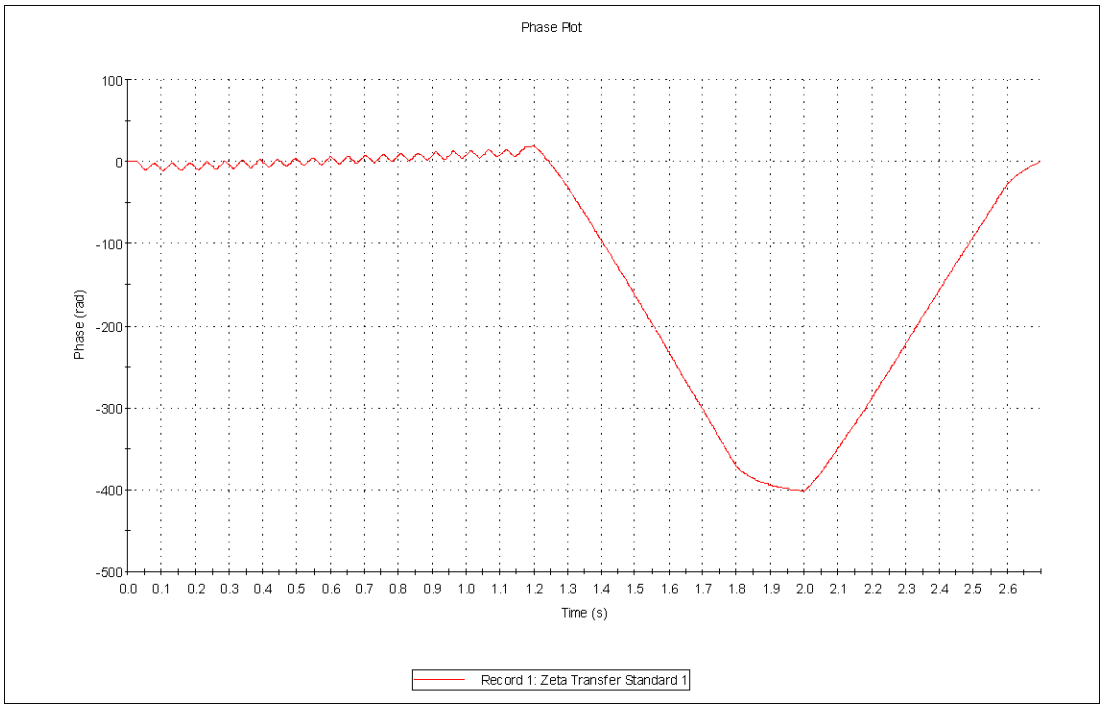

(b)

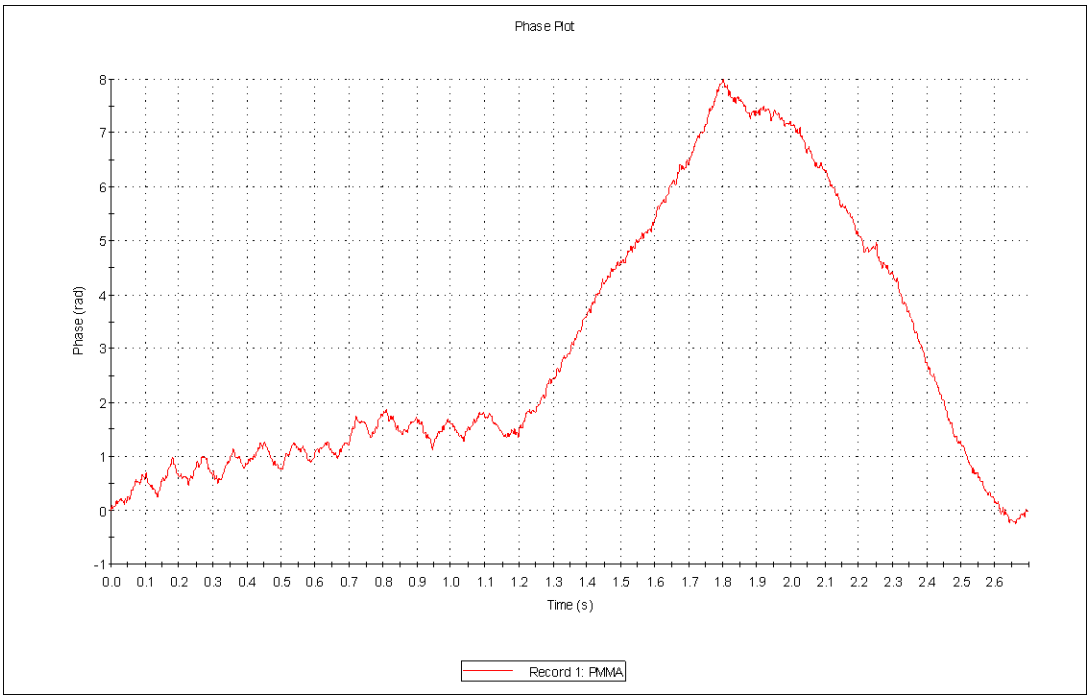

Figure A.3 – Zetasizer Nano ZS phase plots for (a) transfer standard DTS0320 and (b) 609nm DPDMS-PMMA particles dispersed in CHB/decalin containing 6mM TBAC. Plots are taken directly from Zetasizer Nano ZS program by Malvern Instruments.

References

1. *Zeta Potential: An Introduction in 30 Minutes*, in *Malvern Instruments Technical Notes*, Malvern Instruments Ltd.
2. Probstein, R.F., *Physicochemical Hydrodynamics: An Introduction*. Second ed. 2003, Hoboken, N.J.: John Wiley & Sons, Inc. 400.
3. *Malvern Instruments - Products*. [cited 2009 December 17]; Available from: http://www.malvern.co.uk.
4. *Simplifying the measurements of zeta potential using M3-PALS*. Malvern Instruments Zetasizer Nano Application Notes

APPENDIX B

SIMULATION RESULTS FOR PAIR INTERACTION POTENTIAL METHODOLOGY STUDY

In Chapter 2, we presented a methodology for ascertaining the pair interaction potential directly from confocal laser scanning microscopy images. Working in conjunction with computer simulations, we were able to validate our experimental results. In section 2.4.3, key results from simulation work were presented to compare and validate experimental findings. In this appendix, additional results from simulations are presented. These results provided additional information that was used to develop the methodology presented. All results are based on Monte Carlo simulations performed by Chris Iacovella in the Glotzer group [1].

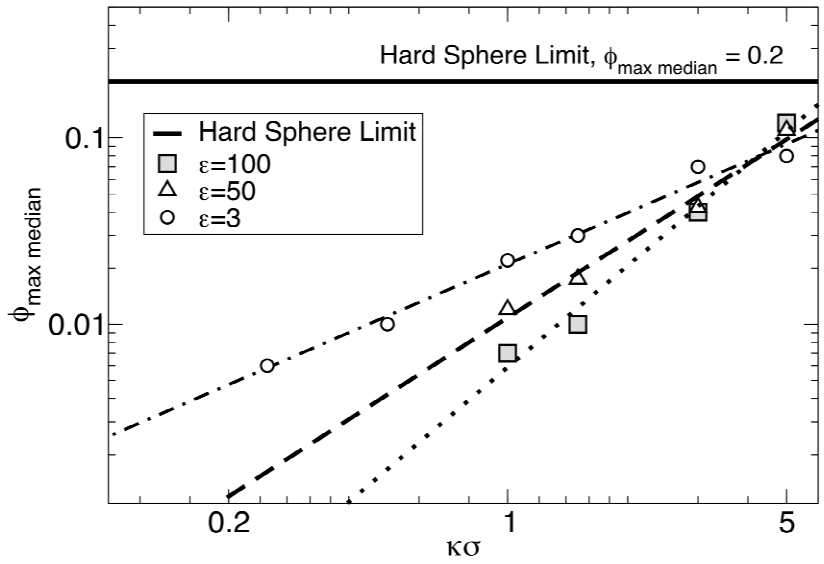

Figure B.1 – The median value of ϕ_{max} as a function of the dimensionless Debye length showing the approximate crossover between concentrated and dilute regimes. Figure by Chris Iacovella.

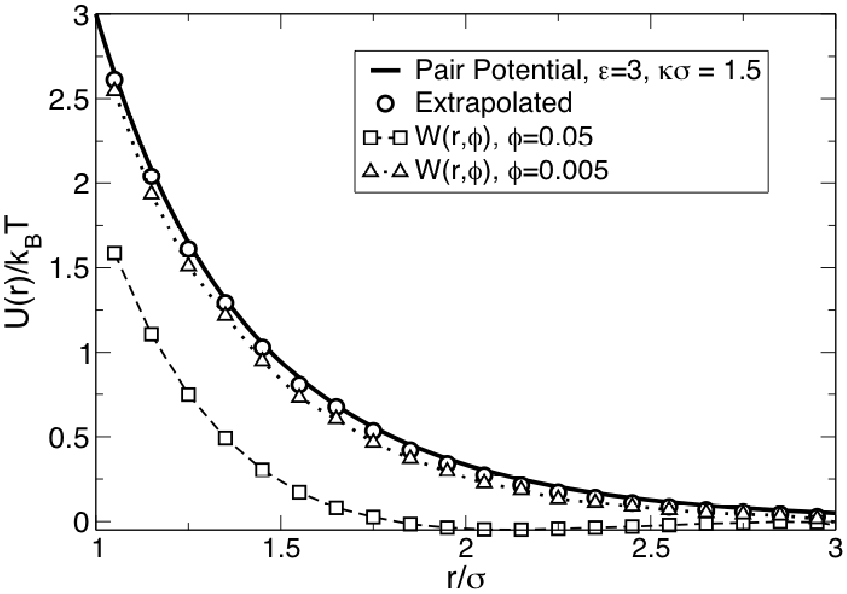

Figure B.2 - For a Yukawa system with ε=3 and $\kappa\sigma$ = 1.5, the pair potential and extrapolated potentials are plotted showing excellent agreement. The extrapolated potential was calculated from 11 values of ϕ ranging from 0.002-0.03. $W(r,\phi)$ is also plotted for ϕ = 0.05 and 0.005. Figure by Chris Iacovella.

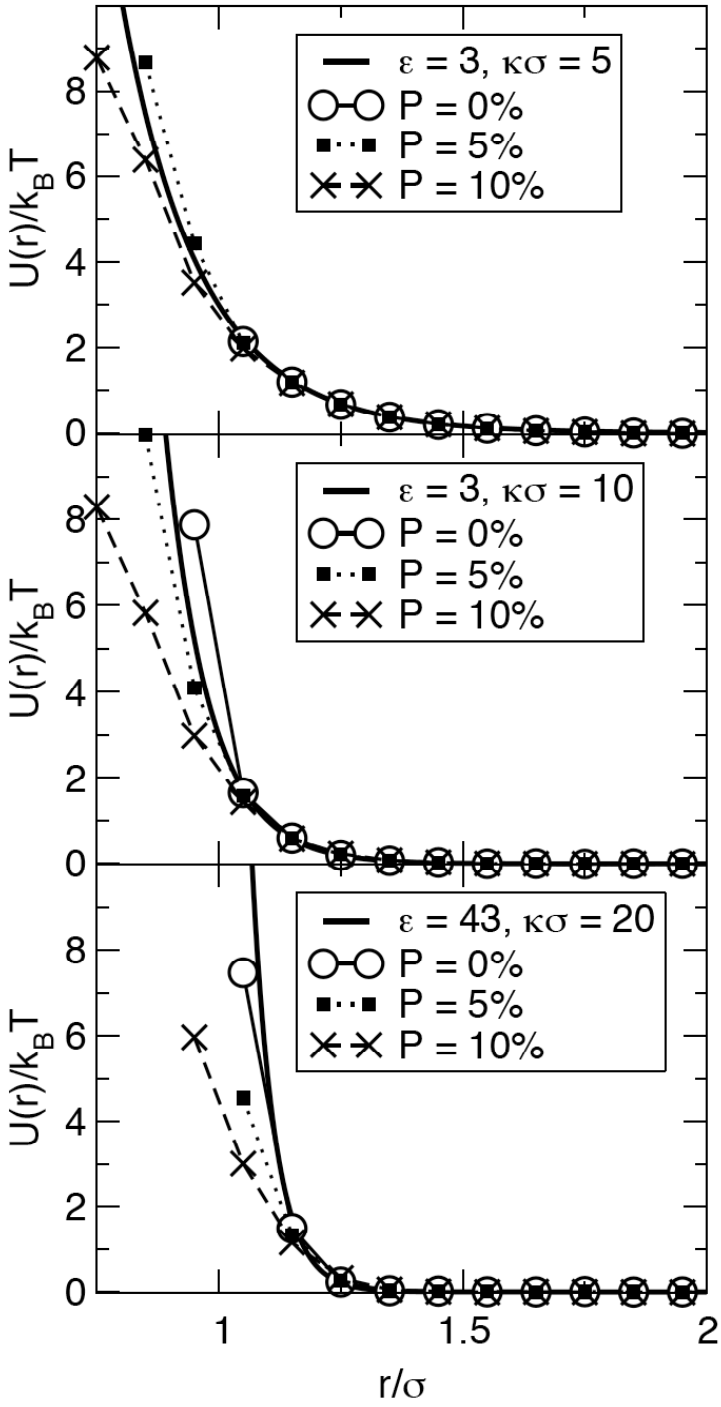

Figure B.3 – Simulation of polydispersity effects on extrapolated potential. At low values of ε and κσ, we found very little to no deviation between the extrapolated potential and the true potential. However, at high values of ε and κσ, polydispersity effects are significant. The polydispersity of our particles was 4% so our extrapolated potential was not affected by potential polydispersity issues. Figure by Chris Iacovella.

References

1. Iacovella, C.R.; Rogers, R. E.; Glotzer, S. C.; Solomon, M. J., *Pair Interaction Potentials by Extrapolation of Confocal Microscopy Measurements of Collective Structures.* In Preparation, 2010.

APPENDIX C

IONIC COLLOIDAL CRYSTALLIZATION USING CENTRIFUGATION FOR RAPID ASSEMBLY

The technique of centrifugation is an assembly approach to crystallization that has been shown to produce colloidal crystals on time scales much faster than that seen for sedimentation. Several studies have looked at centrifugation and colloidal crystallization [1-3]. In this study, we attempt to produce ionic colloidal crystals using centrifugation. The Peclet number is once again utilized to investigate how centrifugation speed correlates to ionic crystal formation. An examination of the range of crystallization is compared against crystallization under normal gravity. The objective of this work is to determine if centrifugation will produce high quality crystalline structures and compare the time it takes to produce such structures with those that generated under normal gravity (i.e. sedimentation).

C.1. Experimental

Poly-12-hydroxystearic acid-stabilized poly(methyl methacrylate) (PHSA-PMMA) and poly(diphenyl-dimethyl siloxane)-stabilized poly(methyl methacrylate) (DPDMS-PMMA) particles were synthesized using the methods of Antl et al. [4] and

Kogan et al. [5]. Sizes of the particles were 660 nm (PHSA-PMMA) and 609 nm (DPDMS-PMMA) as determined from scanning electron microscopy (SEM) measurements. Particles were dispersed in a solution of cyclohexyl bromide (CHB) and decalin containing 6 mM tetrabutyl ammonium chloride (TBAC) salt. The mass ratio of CHB to decalin was set to 71% CHB/29% decalin. This ratio was chosen based on prior success at reproducing ionic colloidal crystals with this system under sedimentation. Particles were allowed to sit idle for at least 3 hours in order for the charge on the particles to reach equilibrium. Figure C.1 shows the specially designed capillary cell used for this study. A capillary (I.D. 2mm, O.D. 6mm) was placed at the center of a Pyrex glass ring (O.D. 16mm, I.D. 13mm). Cover glass (Corning, New York, United States), approximately 0.16-0.19 mm thickness, was attached to the bottom of the glass ring using epoxy glue. The capillary was glued to the cover glass using the same epoxy. To maintain the stability of the apparatus, poly(dimethyl siloxane) (PDMS) was used to fill the glass ring and surround the capillary. The PDMS baked at 80^{o}C for one hour and allowed to harden. A microsyringe was used to place ~20μL of solution into the capillary cell.

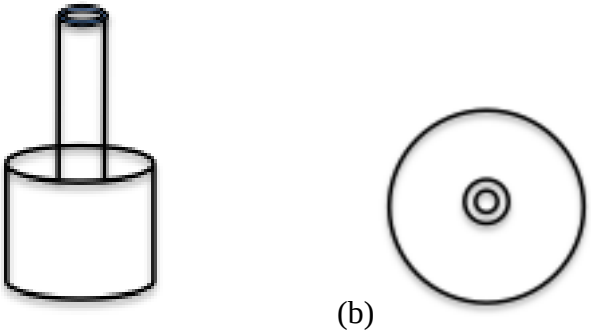

Figure C.1. - Capillary cell design for centrifugation experiments. (a) Side view showing smaller capillary cell housed inside of larger glass ring. Roughly one-half of the capillary cell is recessed inside of the ring. (b) Bottom view showing position of capillary cell in relation to the ring. Not shown is the cover glass used to close the bottom of the device.

Candidate samples were placed in 50mL Oak Ridge centrifuge tubes (Nalgene, United States). Due to the high speeds the samples would experience from the centrifuge, additional care was required. For protection purposes, the centrifuge tubes were stuffed with Kimwipes (Kimberly-Clark Corporation, United States) approximately 2/3 the length of the tube. The sample cell was gently loaded into the centrifuge tube and additional Kimwipes were used to cushion the sample as well as avoid damaging the cell. Once prepared, the centrifuge tubes were loaded into an Allegra 21R benchtop centrifuge (Beckham Coulter, Inc., United States). To fully understand the scope of ionic crystallization possible, proposed centrifuge speeds ranged from 150 rpm to 10,000 rpm. Spin times varied based on the centrifuge speed. Typical times ranged from 1 hour to 24 hours. Table C.1 lists the centrifuge speeds and the associated time each experiment was allowed to run.

Table C.1 – Centrifuge speeds and run times for ionic colloidal crystallization samples

Centrifuge Speed (rpm)	**Experiment Run Time(s) (hrs)**
150	24
500	1, 5, 12, 24
1,000	1, 5, 12, 24
1,500	1, 5, 12, 24
2,000	1
3,000	1
4,000	1
5,000	1
7,500	1
10,000	1

Confocal laser scanning microscopy (CLSM) was used to image the samples. Excitation and emission wavelengths were set to 458nm (excitation)/470-530nm (emission) for the DPDMS-PMMA particles and 543nm (excitation)/550-650nm (emission) for the PHSA-PMMA particles. As the particles were forced against the walls of the capillary cell, scanning commenced from the outer edge of the cell towards the center. Once the particles were located, image stacks were collected. A zoom factor of 7 (21.42μm x 21.42μm) was chosen to take images on the far field scale. Double refinement of the image quality was done using the advanced features of the CLSM as well as ImageJ (NIH) image processing software.

C.2. Results & Discussion

The Peclet number, which is the ratio of the convective forces to the diffusive forces, was calculated in order to quantify and compare the relative centrifugal force (RCF) to the degree of crystallization that would be seen at each condition. According to Hoogenboom et al., the Peclet number can be computed according to the following equation

$$Pe = \frac{(\Delta\rho)gR^4}{k_B T} \qquad \text{(C-1)}$$

where Pe is the Peclet number, $\Delta\rho$ is the density difference between the particle and solvent, g is gravity as a function of the RCF, R is the particle radius, k_B is the Boltzmann constant, and T is the absolute temperature. In this equation, g is the RCF times the acceleration due to gravity. Table C.2 presents the Peclet number at each of the centrifugal speeds. We noted the sharp increase in the Peclet number as the speed of the centrifuge increased.

Table C.2 – Centrifuge speeds and Peclet numbers for ionic colloidal crystallization samples

Centrifuge Speed (rpm)	RCF	Peclet Number
150	1	8.00×10^{-3}
500	11	9.60×10^{-2}
1,000	45	0.386
1,500	100	0.868
2,000	179	1.54
3,000	402	3.47
4,000	715	6.17
5,000	1,118	9.65
7,500	2,516	21.7
10,000	4,472	38.6

Since the Peclet number is the ratio of convective forces (due to gravity) to diffusive forces (thermal interactions), it was preferred that the Peclet number be kept under a value of 1. Initially, experiments were done at 3,000, 4,000, and 5,000rpm; however, our analysis of the Peclet number showed that these speeds could be too large to achieve the desired crystallization. Figure C.2 confirms this understanding. The image shows the result of a sample centrifuged at 5,000 rpm for 1 hour. We did not observe any crystalline ordering in the sample. It should be noted that the majority of the particles were located along the edge of the capillary. Therefore, it could be the case that some of the particles were located on the wall (z-axis) where it was difficult to image.

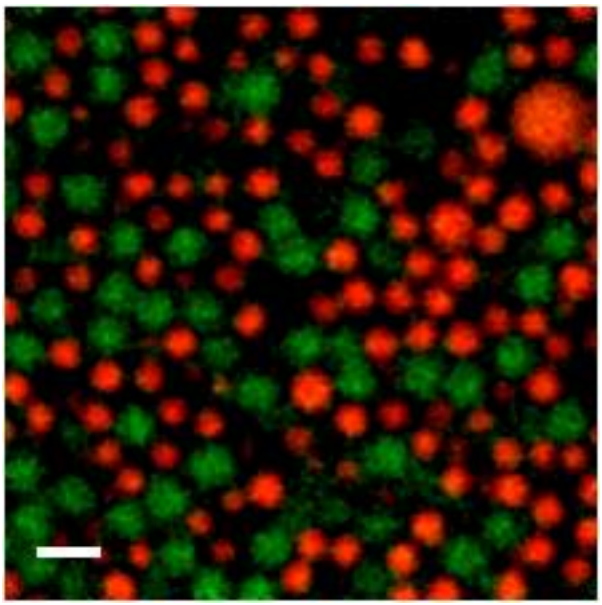

Figure C.2 – CLSM image of PHSA-PMMA (660nm, red) and DPDMS-PMMA (609nm, green) in CHB/decalin (71%/29% by mass). Particles were centrifuged at 5,000 rpm for 1 hour then immediately imaged. Scale bar = 2μm.

We decided to limit our experiments to centrifuge speeds of 1,500 rpm or less to keep the Peclet number below 1. This would allow the diffusive (thermal) forces to remain dominant. We noted that a centrifuge speed of 150 rpm mimicked the condition seen for a sample placed on the bench top counter and exposed to the influence of normal gravity. Given this fact and the lower limit of the centrifuge (200 rpm), experiments at 150 rpm were not done.

For the experiments that were attempted at centrifuge speeds of 500, 1,000, and 1,500 rpm, it was found that crystallization was not achieved. Figure C.3 shows the results for 1,000 rpm. No crystallization was found at all time periods studied. We were surprised by this outcome given the Peclet number was under 1.

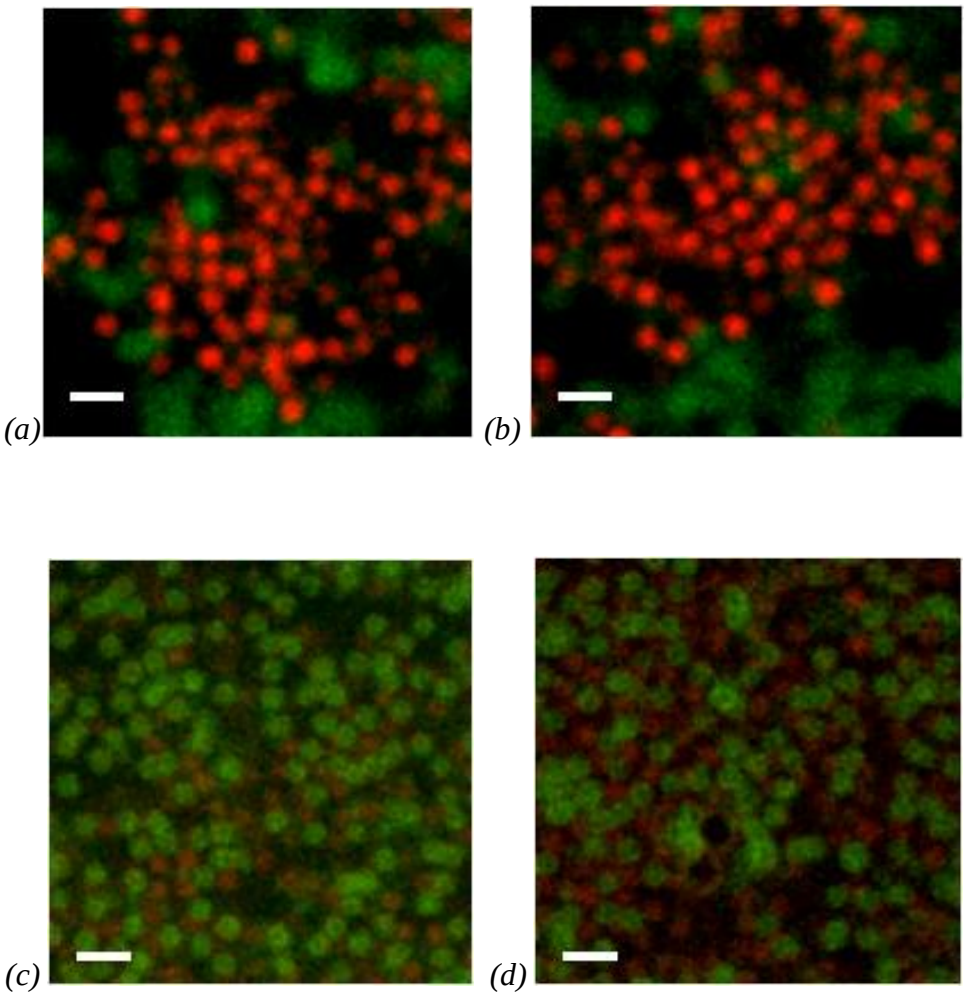

Figure C.3 - CLSM image of PHSA-PMMA (660nm, red) and DPDMS-PMMA (609nm, green) in CHB/decalin (71%/29% by mass). Particles were centrifuged at 1,000 rpm for 5 hours (a and b) and 24 hours (c and d) then immediately imaged. Scale bar in each image = 2μm.

To confirm that the crystal was reproducible with the particles and solvent condition, a sample was prepared and placed on the bench top counter and allowed to sediment for 24 hours. Upon scanning the sample, we confirmed that crystallization was taking place with the particles and solvent. We proceeded to attempt the crystallization at centrifuge speeds of 200 rpm and 300 rpm. This correlated to Peclet numbers of 1.54×10^{-2} and 3.47×10^{-2}, respectively. Spin times were set at 3 hours and 24 hours. Again, no

crystallization was achieved at any of the conditions. Figure C.4 shows the result for centrifuging at 200 rpm.

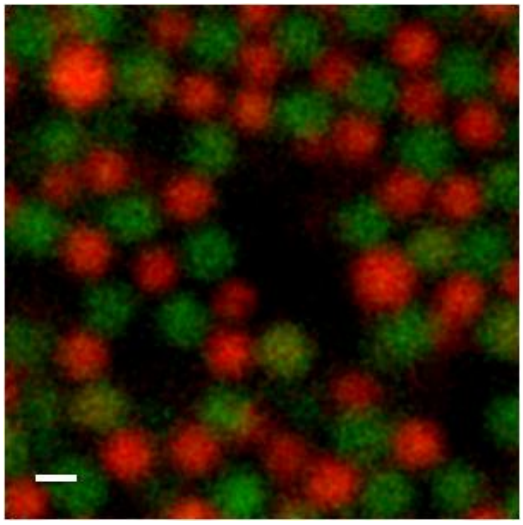

Figure C.4 - CLSM image of PHSA-PMMA (660nm, red) and DPDMS-PMMA (609nm, green) in CHB/decalin (71%/29% by mass). Particles were centrifuged at 200 rpm for 24 hours then immediately imaged. Scale bar = 1μm.

There are two possible explanations for these results. First, the sample cell may not have been in the proper position while in the centrifuge tube. The cell was placed in an upright position (aligned along the vertical axis) in the tube. This could have been the incorrect position as the tube was place at an angle in the centrifuge. With gravity pulling straight down, the actual forces applied to the cell was both gravity and centrifugal. As such, the extra applied force could have been too much for the crystal to remain stable for the time periods studied. Second, damage to the cell could have disrupted any crystallization that may have taken place. As previously mentioned, the sample cell had to be carefully cushioned in the centrifuge tube to prevent any damage from occurring. Even so, due to the fragile nature of the glass cell, we did observe some damage on the cover glass.

These two possibilities may explain the why we were not able to crystallize our particles using centrifugation. However, additional analyses would be required.

C.3. Recommendations for Future Work

The potential benefits and learning that can be gained from doing ionic colloidal crystallization by way of centrifugation warrant additional experiments to be performed. Based on our learning from these initial experiments, we make the following recommendations:

1. The sample cell should be modified to ensure its rigidity during the centrifugation portion of the experiment. We found that the thin cover slip was prone to cracking even when the sample cell was well cushioned. This led to leaking out of the solvent and therefore loss of the sediment. A thicker cover glass should be used; however, the chosen cover slip need not be too thick to prevent visualization on the CLSM.

2. A sample holder should be constructed to lock the sample cell in place. Currently, we are carefully placing the sample cell into specially packed centrifuge tube and relying on the packing to hold the sample cell in place. There is some risk associated with this approach. The sample cell can shift leading to damage of the cover slip or other abnormalities (e.g. particle forced out of the solvent and stuck on the wall). For this study to be successful, the sample cell needs to be in a fixed position from start to finish.

References

1. Dinsmore, A.D., J.C. Crocker, and A.G. Yodh, *Self-assembly of colloidal crystals.* Current Opinion in Colloid & Interface Science, 1998. **3**(1): p. 5-11.
2. Pusey, P.N. and W. Vanmegen, *Phase-Behavior of Concentrated Suspensions of Nearly Hard Colloidal Spheres.* Nature, 1986. **320**(6060): p. 340-342.
3. Velev, O.D. and A.M. Lenhoff, *Colloidal crystals as templates for porous materials.* Current Opinion in Colloid & Interface Science, 2000. **5**(1-2): p. 56-63.
4. Antl, L., J.W. Goodwin, R.D. Hill, R.H. Ottewill, S.M. Owens, S. Papworth, and J.A. Waters, *The Preparation of Poly(Methyl Methacrylate) Lattices in Nonaqueous Media.* Colloids and Surfaces, 1986. **17**(1): p. 67-78.
5. Kogan, M., C.J. Dibble, R.E. Rogers, and M.J. Solomon, *Viscous solvent colloidal system for direct visualization of suspension structure, dynamics and rheology.* Journal of Colloid and Interface Science, 2008. **318**(2): p. 252-263.